MECHANICALLY INDUCED RESIDUAL STRESSES:
MODELLING AND CHARACTERISATION

by

Jean-Claude E. Stranart, *M.A.Sc.*

A thesis submitted in conformity with the requirements
for the Degree of Doctor of Philosophy,
Department of Mechanical and Industrial Engineering
University of Toronto

National Library
of Canada

Acquisitions and
Bibliographic Services

395 Wellington Street
Ottawa ON K1A 0N4
Canada

Bibliothèque nationale
du Canada

Acquisitions et
services bibliographiques

395, rue Wellington
Ottawa ON K1A 0N4
Canada

Your file Votre référence

Our file Notre référence

0-612-49944-8

Canada

Thesis Title:	Mechanically Induced Residual Stresses: Modelling and Characterisation
Degree and Year:	Doctor of Philosophy, 2000
Name:	Jean-Claude E. Stranart
Department:	Graduate Department of Mechanical and Industrial Engineering
University:	University of Toronto

Abstract

Accurate characterisation of residual stress represents a major challenge to the engineering community. This is because it is difficult to validate the measurement and the accuracy is doubtful. It is with this in mind that the current research program concerning the characterisation of mechanically induced residual stresses was undertaken. Specifically, the cold expansion of fastener holes and the shot peening treatment of aerospace alloys, aluminium 7075 and titanium Ti-6Al-4V, are considered.

The objective of this study is to characterise residual stresses resulting from cold working using three powerful techniques. These are: (i) theoretical using three dimensional non-linear finite element modelling, (ii) semi-destructive using a modified incremental hole drilling technique and (iii) nondestructive using a newly developed guided wave method supplemented by traditional C-scan measurements.

The three dimensional finite element results of both simultaneous and sequential cold expansion of two fastener holes revealed the importance of the separation distance, the expansion level and the loading history upon the development and growth of the plastic zone and unloading residual stresses. It further showed that the commonly adopted two dimensional finite element models are inaccurate and incapable of predicting these residual stresses. Similarly, the dynamic elasto-plastic finite element studies of shot peening showed that the depth of the compressed layer, surface and sub-surface residual stresses are significantly influenced by the shot characteristics. Furthermore, the results reveal that the separation distance between two simultaneously impacting shots governs the plastic zone development and its growth.

In the semi-destructive incremental hole drilling technique, the accuracy of the newly developed calibration coefficients and measurement techniques were verified with a known stress field and the method was used to measure peening residual stresses.

Unlike traditional ultrasonic techniques, the newly proposed leaky Lamb wave method is sensitive to sub-surface and in-depth acousto-elastic changes, making it suitable for the measurement of depth dependent residual stresses. A newly designed, commissioned and automated leaky Lamb wave test facility was used to acquire the frequency response of multi-layered systems and successfully applied to characterise shot peened components.

Acknowledgements

I offer my sincere gratitude to Dr. S.A. Meguid for his technical and financial assistance, and his patience throughout the course of my research. I also wish to acknowledge the invaluable assistance of Dr. Genadis Shagals. To the members of the Engineering Mechanics and Design Laboratory I give my thanks for their friendship and help during the undertaking of the current study.

The financial support of the Manufacturing Research Corporation of Ontario, the Natural Sciences and Engineering Research Council of Canada and the Metal Improvement Company is gratefully acknowledged.

Finally, my wife Mary Kocur and my son Daniel can never be repaid for the patience and understanding they showed and the constant support they provided.

Notations

E - elastic modulus

$H^{\cdot}$ - strain-hardening coefficient

K_n , K_t - normal and tangential stiffnesses of contact element

$\mathbf{u}$ - displacement

ε - strain

ε_1, ε_2, ε_3 - relaxed strains

σ - stress

σ^r - residual stress

σ^r_θ - residual stress in the circumferential direction

$\bar{\sigma}$ - von Mises equivalent stress

σ_I, σ_{II} - principal stresses

σ_o - initial yield stress

μ - coefficient of friction

ν - Poisson's ratio

Hole Drilling

B, C - hole drilling calibration coefficients

h - hole depth

Cold Hole Expansion Model

c - half-distance between adjacent holes

h, w, t - dimensions of plate

R - radius of hole

Shot Peening Model

a/b - shot aspect ratio
C - shot separation
R - radius of shot
v - shot velocity
W, H, B - dimensions of peened target
ε^{p}_{eq} - equivalent plastic strain
σ^{r}_{xx} - transverse residual stress
α - incident angle for oblique shot impact

Leaky Lamb Wave

$\mathbf{A}, \mathbf{B}$ - incident and reflected/transmitted conditions at the upper and lower boundaries of the plate
C_{ij} - elastic constants
h - thickness of plate
k_p, k_s - wave numbers associated with P and S waves
MFS - Modal Frequency Spacing
Q_p, Q_s - quality factors to account for dissipation in material
S - frequency spacing between adjacent wave modes
V_p, V_s - velocity of P and S waves
z - depth measured from plate upper surface
λ, μ - Lame constants
ν, η - wave numbers in the z-direction for quasi P and SV waves
ρ - density
ψ, φ - potential functions
$\tau_{xx}, \tau_{yy}, \tau_{xy}$ - components of stress for plane-stress condition
θ - incident angle of ultrasonic beam with respect to surface normal
ω - circular frequency

Contents

List of Figures

List of Tables

Chapter 1 Introduction and Justification

Summary: In this chapter, we define the problem, justify the undertaking of the study and outline the method of approach adopted in achieving the set objectives. Furthermore, we provide a summary of the layout of the thesis.

1.1 Justification of the Study

Fatigue is undoubtedly the most prevalent mode of failure in engineering structures. The consequence of failure of a primary load carrying component, e.g. in an airframe or aeroengine, is usually catastrophic, often resulting in loss of life and hardware. The designers of such critical mechanical systems are constantly faced with the challenge of establishing the appropriate stress levels in these critical parts that will ensure their safe operation under cyclic loading conditions.

At this stage, it is important to identify the pertinent parameters which influence the fatigue behaviour of critical load bearing components/assemblies. These include: (i) the externally applied load and its history, (ii) the geometrical features of the component/assembly, (iii) the residual stress field present in the component, (iv) the environment and (v) the strength and toughness of the material(s) selected. The importance of these parameters is evident in providing guidelines for: (i) the selection of the different geometrical features in existing and new designs, (ii) the life assessment of engineering structures, (iii) the introduction of beneficial residual stresses in highly stressed components, and (iv) the selection of appropriate materials.

In view of their importance to the mechanical integrity of engineering structures, attention in this thesis is devoted to mechanically induced residual stresses. In particular, this work examines the effect of cold hole expansion and shot peening upon the plastic zone development and its growth as well as unloading residual stresses. The selection of these two cold working techniques was motivated by their importance to the aerospace industry, the lack of systematic studies and the interest of the sponsors in the work.

Residual stresses are introduced into components either intentionally by the use of surface treatments, such as shot peening, or unintentionally by most metal forming, metal cutting and fabrication processes, such as forging, rolling, milling and welding. These processes introduce residual stresses as a result of inhomogeneous plastic deformation or thermal treatment. Residual stresses have been found to profoundly affect the fatigue and fracture behaviour of metallic components. For example, in the case of properly performed shot peening treatment, the introduction of compressive residual stresses results in improving the lifetime of the components considerably [1]. Conversely, the introduction of thermal tensile residual stresses in the heat affected zone in weldments may drastically reduce the service life of such components. Several investigators have demonstrated that these residual stresses are not permanent, but tend to diminish as a function of time, temperature, load history and metal removal in the form of either wear or corrosion [2, 3].

Despite their importance, most design engineers do not account for the beneficial effects of residual stresses in their design calculations, and use them merely to increase the margin of safety of critical components. In cases where detrimental residual stresses exist, designers use higher safety factors. Furthermore, a fracture mechanics approach to design is becoming an essential analysis tool for damage tolerance calculations. In that approach, both the applied and residual stress intensity factors are needed to determine the fatigue fracture behaviour and the residual life in engineering structures. It is therefore crucial to be able to characterise the residual stress field in engineering structures consistently and accurately.

In addition, the performance of these structures is generally governed by the interaction between innovative designs, advanced materials and beneficial surface treatments. Considerable gains can be realised by the use of advanced materials together with the application of appropriate surface treatments [4, 5].

1.2 Research Objectives

This thesis is devoted to the accurate characterisation of mechanically induced residual stresses. Specifically, attention is devoted to the development and growth of the plastic zone as well as unloading residual stresses using:

(i) non-linear three dimensional quasi-static finite element analysis,

(ii) non-linear three dimensional dynamic finite element analysis accounting for contact between the shot and the target,

(iii) a modified incremental hole drilling technique to obtain the high in-depth stress gradients in the residual stress profile,

(iv) a newly developed leaky Lamb wave technique. This entailed the design and commissioning of an automated guided wave facility to acquire the frequency response of multi-layered systems and relating the output to peening treatment.

1.3 Method of Approach

Fig. 1-1 shows a schematic of the approach adopted to achieve the above stated objectives. This includes:

(i) finite element studies,

(ii) incremental hole drilling measurements, and

(iii) ultrasonic C-scan and a newly developed leaky Lamb wave inspection method.

Given below is a brief summary of the above mentioned items.

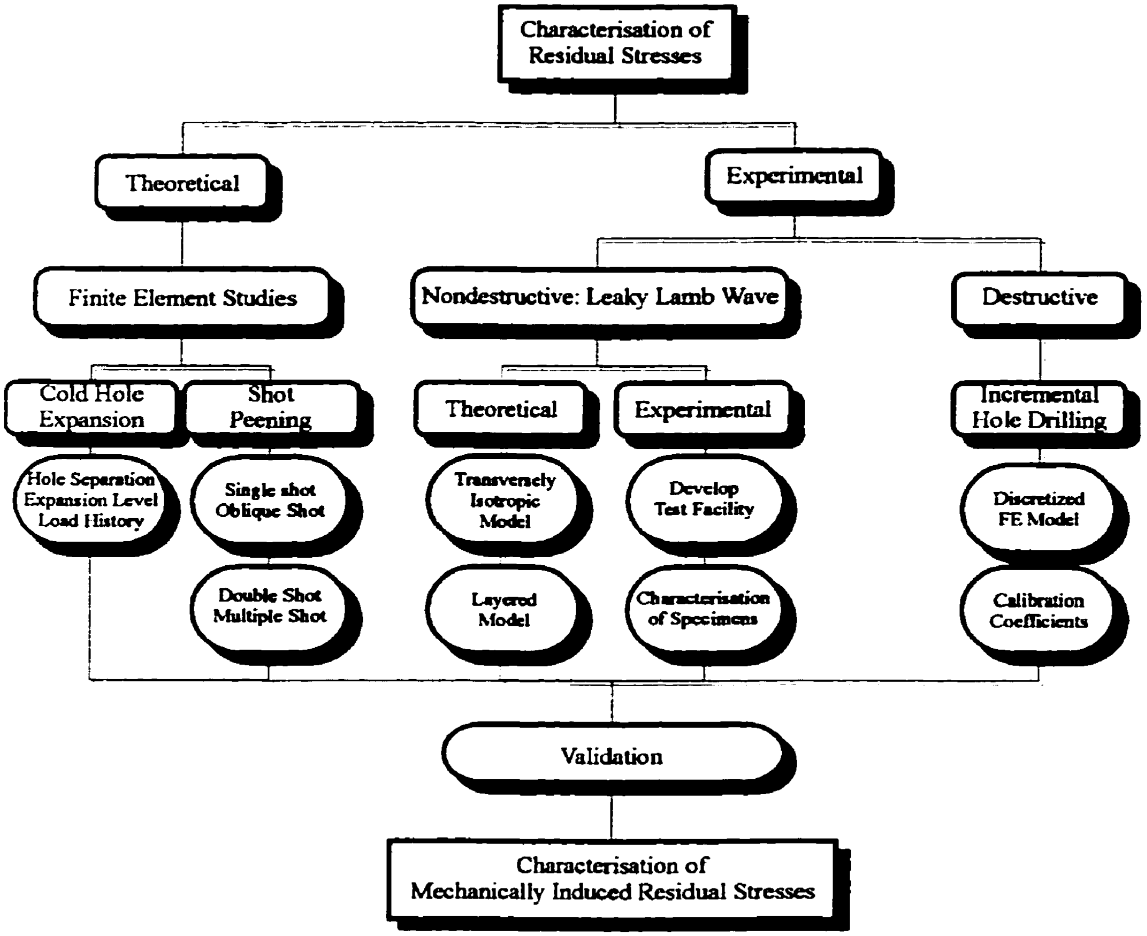

Fig. 1-1 Schematic of method of approach.

1.3.1 Finite Element Studies

This section is divided into two main parts. The first is concerned with the quasi-static simulation of the cold expansion of single and twin fastener holes using non-linear two and three dimensional elasto-plastic finite element models which account for contact between the mandrel and the target. The second is devoted to the dynamic three dimensional non-linear elasto-plastic finite element analyses of the shot peening process. The complexity of these systems is evident in the characterisation of the material behaviour, the selection of the appropriate contact elements and the associated tangential and normal stiffnesses needed by the code, and the selection of the appropriate process parameters and the necessary convergence tests.

1.3.2 Incremental Hole Drilling

The incremental hole drilling method was used for measuring peening residual stresses. The non-uniformity of peening residual stresses was accommodated for by the use of finite element analysis to evaluate the calibration constants. The calibration constants were evaluated for a geometry that complies with existing commercial strain gauge rosettes that were used in the study.

1.3.3 Ultrasonic Leaky Lamb Wave Method

The leaky Lamb wave method was used to characterise peening treatment nondestructively. In this case, the transmitted wave is refracted as well as mode converted to include guided waves which propagate parallel to the surface of the test component. As a result of the destructive interference of the specularly reflected part and the guided wave, minima are introduced to the amplitude spectrum of the received reflected signals. The locations of these minima can be accurately measured and used to evaluate the plastic zone and residual stress profile.

1.4 Layout of Thesis

This thesis is divided into six chapters in total. Following this brief introduction, **Chapter 2** provides a critical review of the relevant work in four main areas: modelling of mechanically induced residual stresses, destructive measurements of residual stresses, semi-destructive measurements, including the use of the incremental hole drilling and nondestructive ultrasonic stress measurement techniques. **Chapter 3** summarises the main issues concerning the quasi-static modelling of the cold hole expansion process and the dynamic simulation of the shot peening process using advanced finite element modelling techniques. In addition, it discusses the modelling of residual stresses to evaluate the effect on the leaky Lamb wave propagation modes. **Chapter 4** describes the experimental aspects of the work. It covers the modified hole-drilling technique, instrumented cold hole expansion as well as ultrasonic analysis and the LLW method for the characterisation of mechanically induced residual stresses. In **Chapter 5** we discuss and analyse the three methods used in characterising the mechanically induced residual stresses: finite element modelling, incremental hole drilling and the ultrasonic leaky Lamb wave method. Finally, in **Chapter 6** we summarise the findings of this work, identify the contribution of the thesis, and outline the need for related future research.

Chapter 2 Literature Review

Summary: This work is concerned with the evaluation of mechanically induced residual stresses, primarily through cold work processes such as shot peening and cold hole expansion. Accordingly, this literature review covers three main issues: The first deals with cold expanded hole induced residual stresses, the second with shot peening induced residual stresses, and the third with the characterisation of the residual stresses present in engineering components.

2.1 Mechanically Induced Residual Stresses

Residual stresses are introduced into metallic components as a result of inhomogeneous plastic deformation. These can arise either intentionally by the use of surface treatments such as shot-peening or unintentionally by most metal forming, metal cutting and fabrication processes such as forging, rolling, milling and welding. Residual stresses have been found to profoundly affect the fatigue and fracture behaviour of metallic components. For example, in the case of shot-peening, the introduction of compressive residual stresses results in improving the lifetime of the components considerably [1]. Conversely, the introduction of thermal tensile residual stresses in weldments may drastically reduce the service life of such components. Several investigators have demonstrated that these residual stresses are not permanent, but tend to diminish as a function of time, temperature, load history and metal removal in the form of either wear or corrosion [2, 3]. It is therefore crucial to be able to characterise the residual stress field in fabricated and treated machine components.

This literature review covers three main topics. The first deals with the analytical, numerical and experimental investigations of the stress field of interacting holes. The second examines the shot peening process, its parameters and the techniques for evaluating the quality of the treatment. The third deals with the state of the art in both destructive and non-destructive techniques for evaluating mechanically induced residual stresses.

2.2 Cold Hole Expansion

2.2.1 Stress Analysis of Interacting Holes

Since the pioneering work of Kirsch [6] of the single hole problem, much attention has been devoted to the development of solutions for problems involving adjacent holes. These solutions will enable the designer to assess the mechanical integrity of engineering components by minimising the stress concentration associated with interacting holes and by predicting the initiation site(s) of potential fatigue cracks. This section will focus on the relevant analytical, numerical and experimental research work concerning the behaviour of adjacent holes under load.

2.2.2 Analytical Investigations

The first attempt to solve the problem of two interacting holes in an infinite medium was carried out by Jeffery [7] in 1920. This problem was an application of his general solution of the two dimensional equations of elasticity in bipolar co-ordinates. Jeffery also solved the problem of a circular disc with an eccentric circular hole and the problem of a semi-infinite plate bounded by a straight edge and a circular hole. Later, Mindlin [8, 9] corrected the solution of the latter problem. Mindlin found that as the hole approaches the free edge, the tangential stress at the hole boundary close to the edge (point n, Fig. 2-1) tends to infinity while the tangential stress in the diametrically opposite point (p) becomes 4 for a uniaxial applied unit stress. On the other hand, the stress at the corresponding point on the free edge (point m) varies from a value equal to the applied stress when the hole is far away to zero when the hole approaches the boundary. These theoretical results were also verified by Mindlin using photoelasticity.

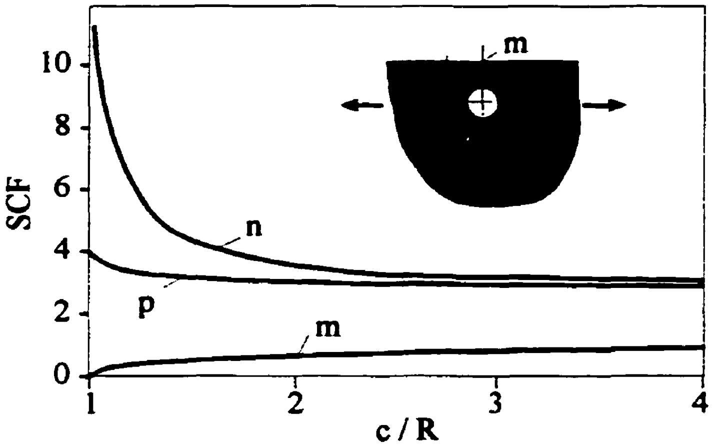

Fig. 2-1 Stress concentration factor at different locations for a hole close to a boundary (after [9]).

In 1974, Yu and Sendeckyj [10] provided a solution to the problem of multiple circular inclusions in an infinite matrix using the Schwartz alternating method. The solution of the single inclusion was obtained using the complex potential method. In 1985, Horii and Nemat-Nasser [11] introduced the method of pseudo-tractions to calculate the stress and strain fields in a linearly elastic homogeneous solid containing a number of defects of arbitrary shape. However, the method was applied to cases involving interacting circular holes and cracks. In the case of interacting holes, the solution was obtained by superimposing the homogeneous subproblem to two subproblems (Fig. 2-2), each consisting of an infinitely extended body with only one hole and zero stresses at infinity. The radial and shear stresses applied to the hole boundary in each subproblem are called pseudo-tractions and have to be determined from the boundary conditions of the problem.

Meguid and Shen [12] developed a general solution describing the interaction between a main hole and an arbitrarily located defense hole under uniaxial and biaxial loading conditions. Their solution was based upon the complex potentials of Muskhelishvili, an appropriate superposition procedure and the Laurent series expansion method. They provided approximate closed form expressions for the stress field. They concluded that both the location and the magnitude of the maximum tangential stress at the main hole change for a different inclination of defense hole. In addition, Meguid and Shen found that the largest stress concentration at the main hole occurs when the central line of the two holes is inclined at 30° with respect to the applied load.

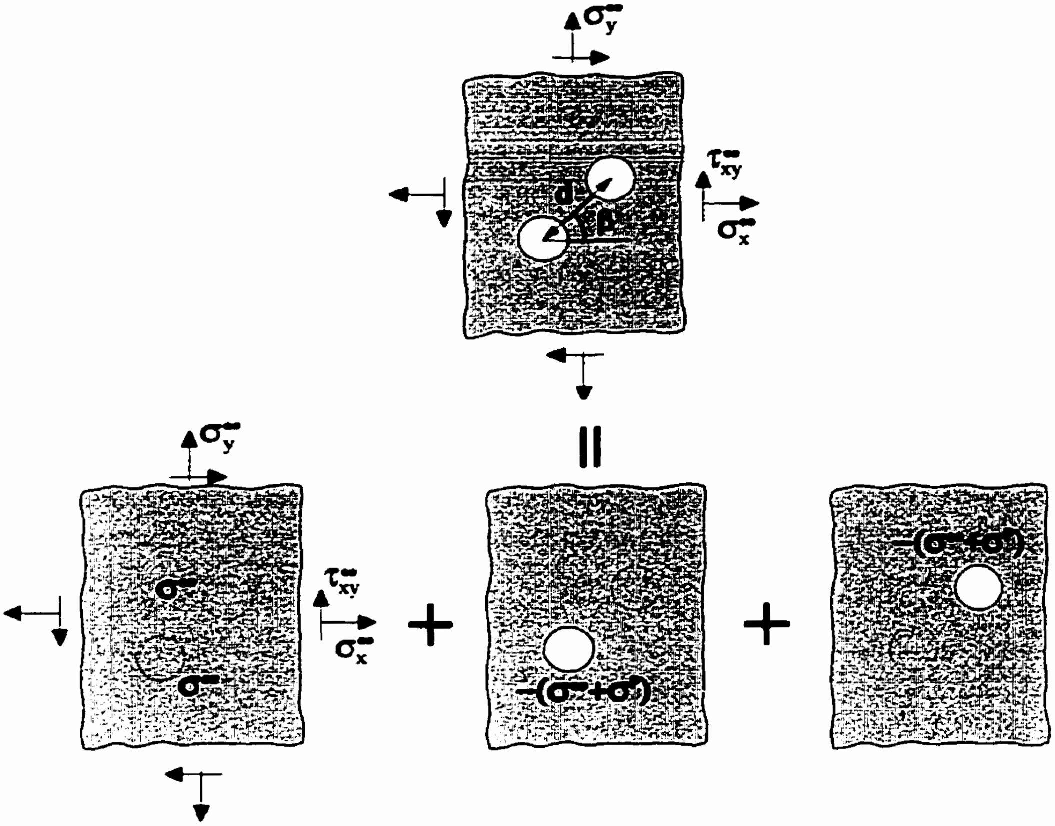

Fig. 2-2 Decomposition of an original problem into a homogeneous problem and two subproblems (after [11]).

The problem of multiple void-crack interaction was treated by Hu et al. [13]. They used a superposition technique to reduce the problem into a number of single-hole and single-crack subproblems. Each hole subproblem was modelled using the method of pseudo-tractions and each crack subproblem was modelled by a distribution of dislocations. They developed an integral equation approach based on two types of fundamental solutions, one due to point loads in a solid containing a hole and the other due to point dislocations in an infinite elastic body. The fundamental solution for a point force acting on the hole boundary was developed earlier by Dundurs and Hetenyi [14, 15].

Finally, Kienzler and Zhuping [16] and Greenwood [17] developed new techniques for treating a single circular hole under plane loading. However, they did not consider the interaction between multiple holes and/or inhomogeneities.

The above review indicates that existing models which are concerned with interacting holes, defects and inhomogeneities, require the use of fundamental solutions. This makes them inflexible and incapable of treating arbitrarily shaped holes and/or defects. It is, therefore, necessary to develop a model capable of treating generalised holes and cracks.

2.2.3 Finite Element and Photoelastic Investigations

Most of the analytical work in this field is related to the stress distribution in the vicinity of interacting holes in infinitely extended elastic bodies. Furthermore, in view of the complex nature of the developed equations, the finite element method and photoelasticity were adopted.

In 1978, Erickson and Riley [18] undertook a study using two dimensional photoelasticity to determine the optimum size and location of defense holes for a number of plates with different central hole diameter to plate width ratios. The defense hole method was introduced by Heywood [19] in 1952. According to this method, smaller holes are introduced on either side of the original hole to help smooth the flow of the tensile principal-stress trajectories past the original hole. This leads to a reduced stress concentration around the original hole. Erickson and Riley reported maximum stress reductions from 13 to 21% for plates with hole diameter to plate width ratios between 0.1 to 0.6. They concluded that with such reductions in the maximum stress level, the improvement in fatigue life of a part can be very significant.

Jindal [20] examined the effect of the hole geometry and the effect of defense holes on the stress concentration around the main hole using both the finite element method and two dimensional photoelasticity. It was found that by making the main hole oblong in the direction of loading, the stress concentration factor at the hole decreased by up to 22%. Jindal concluded that this approach was more effective than the defense holes approach, since the same reduction in stress concentration was achieved, whilst avoiding the introduction of two more regions of higher stress concentration. Meguid [21] considered the case of a rectangular plate with two main holes and three ways of introducing defense holes. He pointed out the significance of the position and inclination of the defense holes with respect to the main hole.

In 1993, Meguid and Gong [22] undertook comprehensive analytical, finite element and photoelastic studies of the interaction between existing main holes and arbitrarily located defense hole systems under uniaxial tension. Their analytical solution, which was based on the complex potentials of Muskhelishvili, an appropriate superposition procedure and the Laurent series expansion, was used to predict the variation of the stress concentration for different defense hole configurations. They concluded that the introduction of defense holes on either side of the original hole helps to smooth the flow of maximum stress trajectories past the original hole.

2.2.4 Residual Stresses Due to Hole Expansion

Cold expansion of fastener holes has been used for over forty years in the aerospace industry. It is a very efficient approach which results in extending the fatigue life of the treated part without any weight penalty. Until recently, particularly for civil aircraft, the technique was only applied to critical holes in highly loaded zones of the structure, such as landing gears and engine mounting regions. In modern aircraft, however, one may find over a thousand cold expanded holes in the wing alone. The requirement of increasing structural efficiency combined with a reduction in manufacturing costs has demanded a closer study of the cold expansion process.

Cold hole expansion is usually conducted using an oversized ball or a mandrel. The radial interference between the "rigid" ball or mandrel and the hole results in inhomogeneous plastic deformation (Fig. 2-3). Upon unloading, the elastically stressed regions away from the hole tend to fully recover, and as a result impose a compressive residual stress field on the plastically deformed regions (Fig. 2-4). This highly localised compressive field at or near the hole boundary is equilibrated by the development of a tensile residual stress field in the surrounding regions. These compressive residual stresses are highly effective in preventing premature fatigue failure under conditions of cyclic loading [23, 24].

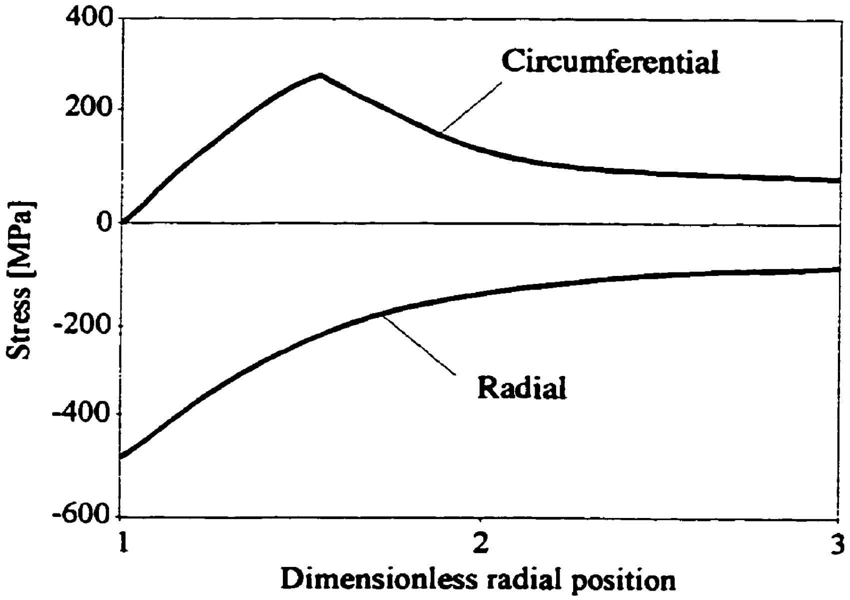

Fig. 2-3 Circumferential and radial stresses prior to unloading (after [24]).

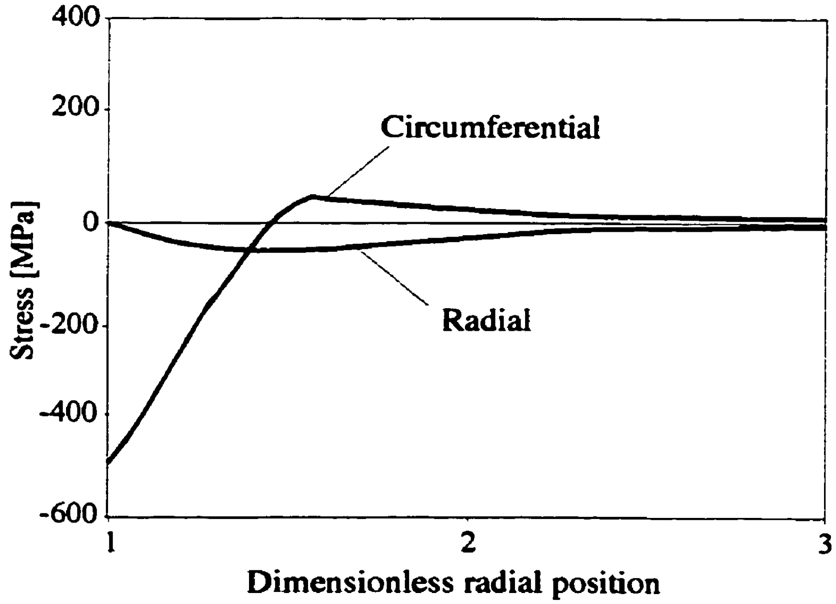

Fig. 2-4 Residual circumferential and radial stresses after unloading (after [24]).

A major impediment to the use of ball or mandrel in the cold hole expansion of fasteners is the surface damage introduced at the interface during the cold expansion process. To overcome this difficulty, the split sleeve expansion, split mandrel expansion and roller expansion methods have been developed. In the split sleeve method (Fig. 2-5) a thin, dry lubricated sleeve is placed over the stem of the mandrel and is pushed into the hole creating an interference fit. The mandrel is then drawn back through the split sleeve. Aircraft holes commonly treated by this method range from 5 mm to over 40 mm in diameter, with expansions between 2% and 6% depending on the material and application. In the split mandrel method, the mandrel is pushed easily through the hole as a result of the presence of a machined groove along its length. This method was developed to replicate all the functions of the split sleeve technique and avoid the use of the sleeve. Finally, the roller expansion technique consists of a set of specially shaped rollers mounted in a rotary tool and inserted into the hole.

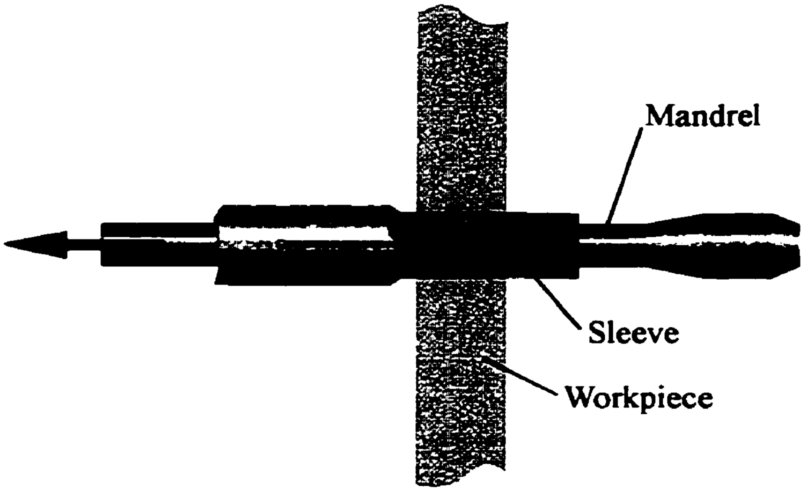

Fig. 2-5 Schematic of the split sleeve method.

Many analytical solutions have been developed to predict the residual stress distribution surrounding cold worked holes. The complexity of these models, however, depends upon the number of variables considered. The exact elasto-plastic solution of an infinite plate containing a circular hole subject to uniform pressure for an ideally plastic material was provided by Nadai [25] in 1950. Later, Hsu and Forman [26] obtained the residual stress field of an expanded hole, accounting for material hardening. Rich and Impellizzeri [27] improved the model presented in [26] by assuming isotropic hardening behaviour to account for compressive yielding on unloading. The solution under plane stress and plane strain conditions of linear hardening materials was also given by Jongebreur and Koning [28]. Recently, Wanlin [29] extended the solution of Hsu and Forman [26] to account for plates with finite width.

Existing experimental and axisymmetric finite element investigations reveal that highly non-uniform residual stresses are introduced by the cold expansion method [30-34]. Link and Sanford [30] obtained the residual strain field surrounding a single split-sleeve cold expanded hole in 6.35 mm thick 7075-T651 aluminium plates using moiré interferometry. They concluded that two dimensional analysis is incapable of predicting the residual strain field surrounding cold expanded holes. This may be due to the geometrical and material non-linearities associated with the elasto-plastic contact experienced by the fastener holes, as well as the complexity of the models needed to describe the problem. Cook and Holdway [31] reached the same conclusion as Link and Sanford [30] using the x-ray diffraction technique to measure the radial and hoop residual stresses around cold expanded fastener holes in 7050-T76 alloy. Poussard et al. [32] also used x-ray diffraction and two dimensional and axisymmetric finite element analyses to evaluate the residual stress field around a cold expanded hole in 2024-T351 alloy. Recently, an axisymmetric analysis of the cold expansion process, accounting for contact between the mandrel and the hole surface was conducted by Forgues et al. [33] and Bernard et al. [34].

Table 2-1 shows the reported life improvement due to cold hole expansion in airframe aluminium alloys. For commercial applications, the hole expansion is typically between 2% and 6%, depending on the material and the desired residual stress field. It can be seen in Table 2-1 that depending on the treated materials, hole expansion levels and loading conditions, the fatigue life improvement factor (LIF), defined as the ratio of the fatigue life of the treated hole to that of the untreated hole, ranges from 2 to 20. It has been shown in that larger amounts of coldwork reduce the initiation life of fatigue cracks

Material	Loading Conditions	Expansion	LIF*
7075-T7451	Constant Amplitude (σ_{max} = 207 MPa, R= 0.1)	5 %	5
7075-T651	Constant Amplitude (σ_{max} = 262 MPa, R= 0.05)	6 %	20
7075-T7531	Constant Amplitude (σ_{max} = 80 MPa, R= 0.1)	2.8 %	2
7075-T7351	Fighter aircraft spectrum (σ_{max} = 207 MPa)	4.7 %	4
7075-T6	Constant Amplitude (σ_{max} = 207 MPa, R= 0.1)	3.6 %	5
7075-T73	Commuter aircraft loading spectrum	3.5 %	10
7075-T6	Transport aircraft spectrum (σ_{max} = 127 MPa)	4 %	12
7075-T651	Constant Amplitude (σ_{max} = 262 MPa, R= 0.05)	5 %	14
7079T6	Commuter aircraft loading spectrum	3.5 %	10

* LIF = Fatigue life of treated hole / Fatigue life of untreated hole

Table 2-1 Life improvement due to cold hole expansion (after [24])

due to damage at the hole edge [35]. Therefore, an optimum level of hole expansion has to be found for each material, loading condition and hole geometry.

Extensive search of the literature indicates that no significant attempt has been made to model the cold expansion of adjacent holes. Papanikos [36] has devoted efforts to the two dimensional analysis of the adjacent cold hole expansion process, with an interest in the fatigue fracture behaviour in the presence of residual stresses. He also treated the three dimensional cold hole expansion of a single hole and outlined the variation of the stress field through the thickness of the expanded hole. In this work, however, we focus our attention to the three dimensional analysis of two expanded holes.

Of particular interest is the influence of sequential and simultaneous expansion upon the mechanically induced residual stress field. The importance of examining three dimensionally the effect of separation distance, size and orientation of adjacent fastener holes is apparent in the damage tolerant design of airframes.

2.2.5 Cold Hole Expansion Parameters

This section reviews the various parameters that influence the residual stress field due to the expansion of an open hole and, therefore, the effectiveness of the process. These include process, geometrical, material and loading parameters.

Process Parameters

One of the major process parameters is the hole expansion level. As mentioned earlier, the optimum expansion level should be established for each material, loading and geometry. Another important parameter is the surface upsetting or part thickening which is inherent in the hole expansion process. This out-of-plane displacement occurs at both the entrance and exit sides of the hole and is always greater at the exit side (lip formation). This results in a non-uniform residual stress field throughout the thickness of the component, with greater values of compressive residual stresses at the exit side. Fig. 2-6 shows the fatigue fracture surfaces of two identical specimens which contain (a) an untreated hole and (b) a cold expanded hole. The figure indicates that for the untreated hole, the fatigue crack growth is the same on both sides of the specimen, resulting in a uniform crack profile. On the other hand, hole expansion leads to the introduction of a non-uniform residual stress field which results in a non-uniform crack profile. Subsequent reaming of the cold worked hole will also influence the effectiveness of the expansion process.

Geometrical Parameters

Geometrical parameters include the sequence of cold working, hole depth, hole surface finish prior to expansion, hole straightness, bellmouthing, barrelling, ovality and expansion levels for multi-hole patterns. The influence of the hole geometry before and after expansion on the residual stress field are of particular interest to this thesis and are discussed in detail in Chapter 5. Details of the above mentioned parameters and their influence on the performance of the cold worked part can be found in references [23] and [24].

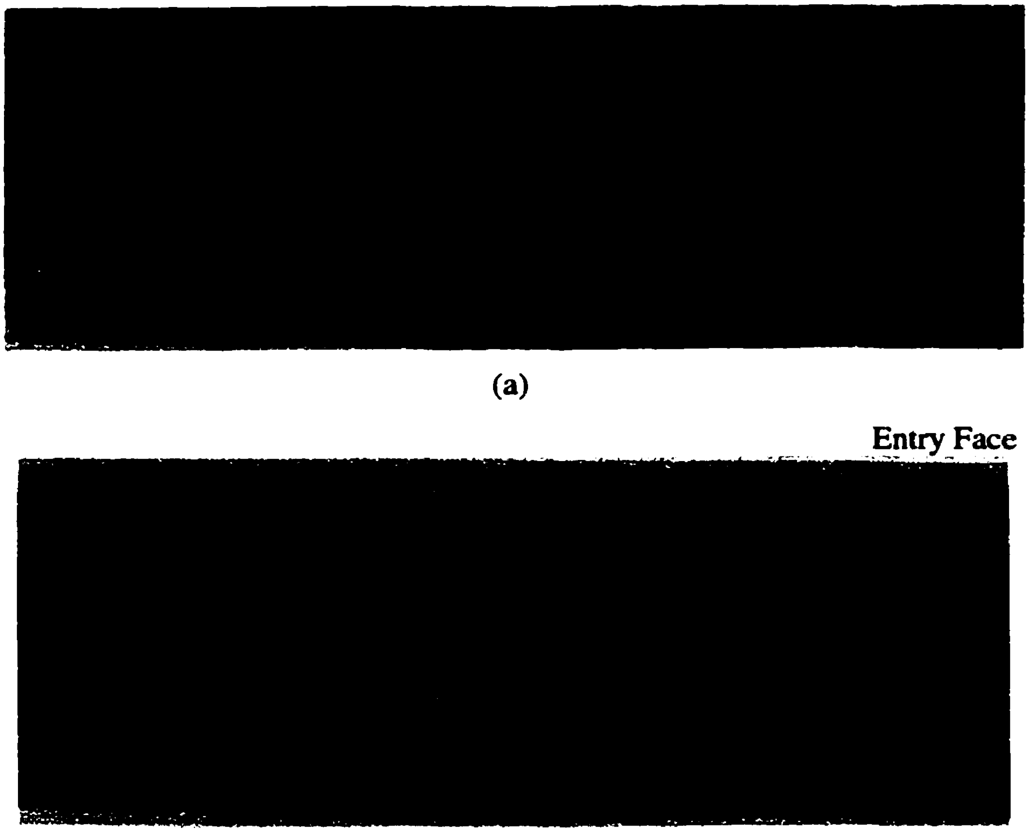

(a)

(b)

Fig. 2-6 Fatigue crack growth of (a) untreated hole and (b) cold expanded hole (after [24]).

Material and Loading Parameters

The applied stress level and the material of the component constitute two other important parameters influencing the residual stress field before and during fatigue crack growth. The results in Table 2-1 clearly demonstrate the importance of these parameters on the effectiveness of the hole expansion process. It was shown that a high level of applied stress can lead to the relaxation of the compressive residual stresses and, hence, reduce dramatically the life of the component [23, 24]. The effect of these parameters upon the residual stress field resulting from the cold expansion of adjacent holes is described in Chapter 5.

2.3 Shot Peening

2.3.1 Shot Peening for Improved Fatigue Resistance

Shot peening is a cold working process used to improve the fatigue life of metallic components. The result is accomplished by bombarding the critical surfaces of the component with small spherical shots made of cast high carbon steel, conditioned cut-wire or ceramic shot at relatively high impinging velocities (70-100 m/s). During impingement, a plastic indentation surrounded by a elasto-plastic zone is formed, as shown in Fig. 2-8. After contact between the shots and the target is ceased, the elastically stressed region tends to recover to the fully unloaded state, while the plastically deformed region sustains some permanent deformation. This inhomogeneous elasto-plastic deformation results in the development of a compressive residual stress field in the uppermost layers. To maintain equilibrium in the peened component, a tensile residual stress field is developed through the depth of the component. The mechanically induced surface compressive residual stresses have been found to be highly effective in enhancing the fatigue resistance of highly stressed engineering components.

The primary justification for shot peening treatment lies in the fact that its use improves the fatigue, fretting fatigue and stress corrosion cracking resistance and allows engineering components to be employed at relatively high stress levels under cyclic loading and/or aggressive environments. In the case of the aerospace industry, this means a reduction in structural weight for a specified reliability level. Typically, turbine and compressor discs and associated blades, propeller and harmonic drives, main rotor spindles and main and nose landing gear components such as bogie beams, wheels, struts and a large number of airframe components are currently being peened. In automotive applications, it means that relatively small low cost components can be upgraded for conservative use at stress levels that would represent poor practice without the treatment. Springs, gears of all types and shapes, connecting rods, cam shafts, crank shafts and torsion bars are examples of components that can be upgraded without the use of costly alloys or increased sections. The ability to upgrade the mechanical properties of a component by shot peening offers obvious opportunities in the correction of undersized components, when, e.g., fatigue failure occurs after a product is standardised or in field service.

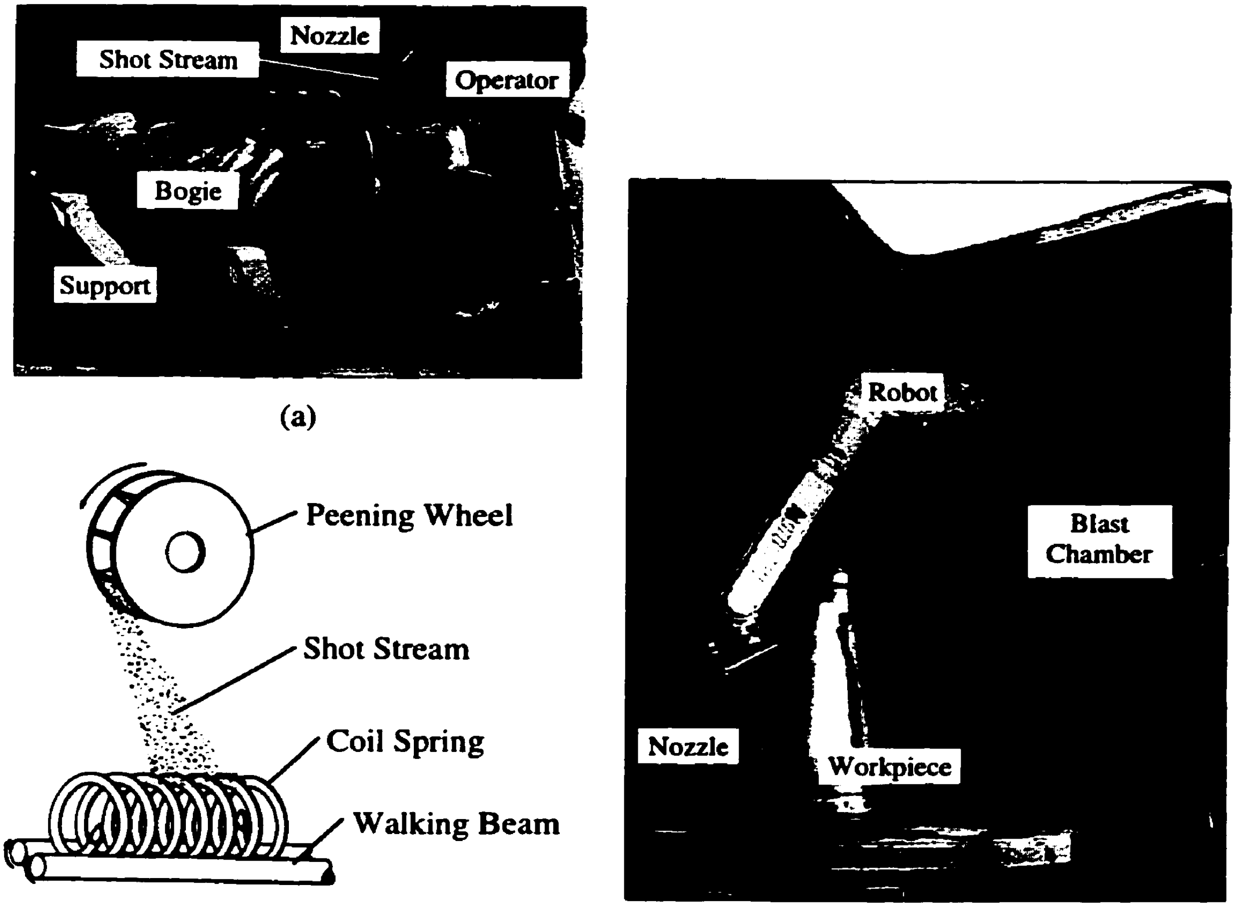

(a)

(b)

(c)

Fig. 2-7 Shot peening of components (a) peening of aircraft bogie using nozzle type machine, (b) wheel peening of coil springs using wheel type machine and (c) robotically controlled peening.

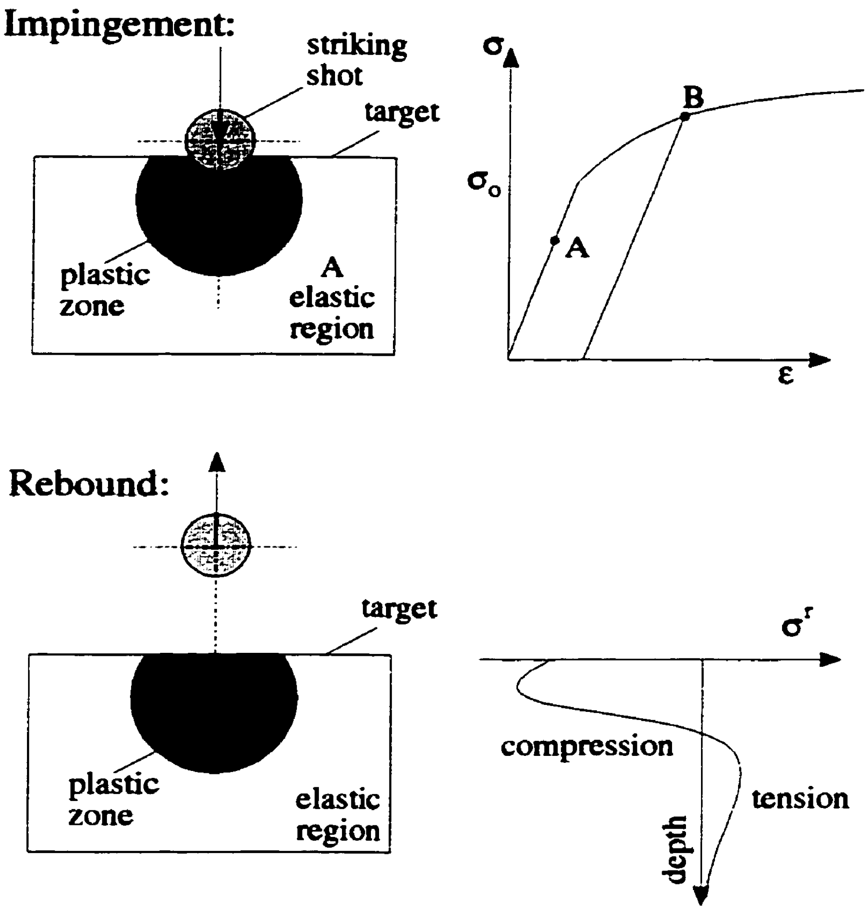

Fig. 2-8 Mechanics of shot peening.

2.3.2 Shot Peening Parameters

The effectiveness of shot peening depends to a large measure on the peening intensity and the peening coverage. Peening intensity is a measure of the consistency of the treatment and of the plastic dissipation of the impinging shots. Peening coverage, on the other hand, is measured in terms of the ratio of the area covered by peening indentations to the exposed area. These parameters depend on numerous variables, including: workpiece characteristics, shot characteristics, flow conditions, jet obliquity, stand-off distance and exposure time. Details concerning these variables and the technique can be found in [37-44].

Measurement of Peening Intensity

Peening intensity is measured by means of Almen test strips, as described in SAE J442 and J443. Three types of strips, designated N, A and C, are used to assess the peening intensity. All strips are nominally 0.75 inch wide and 3 inches long with the following thicknesses: 0.031, 0.051 and 0.094 inch corresponding to N, A and C, respectively. They are made of cold-rolled spring steel which is hardened and heat set between flat plates for 2 hours at 430°C to obtain a hardness of 44 to 50 R_C for A and C strips and 72 to 76 R_B for N strips. The Almen test strip is held flat in a holder during exposure to the jet stream. The difference in residual stresses between the peened surface and the bulk of the strip produces a curvature. An Almen gauge is used to measure the arc-height at the middle of the strip over a standardised length of 1.25 inches. It is worth mentioning that this curvature is an accumulative measure of the effect of the peening parameters. The A and C strips are commonly used when peening high strength alloys with metallic shot and the N strip is usually used when peening delicate components with glass beads or ceramic shot. The standard method for designating peening intensity is to give the arc-height in thousands of an inch followed by a letter indicating the strip type, for example, 12A.

The peening intensity is determined from a "saturation curve". To develop a proper saturation curve, the following standardised steps must be adhered to. A series of Almen strips are peened for various exposure times under specific peening conditions. Measuring the arc-heights and plotting these values versus exposure time yields a curve similar to that shown in Fig. 2-9. This figure suggests that during the early stages of the peening process, a rapid rate of arc-height generation develops with increasing time, and this is not maintained. The decline in the rate of arc-height generation is attributed to the target exposed surface being progressively subjected to highly localised deformations, and thus as the exposure time increases the target surface layers become harder. Point 'x', where the curve tends to flatten out, represents the characteristic peening intensity for the specific peening condition employed. Obviously, peening for periods longer than the time period represented by point 'x' will have only a limited effect. The time taken to reach point 'x' is known as the saturation time, provided that doubling this time does not increase the arc-height by more than 5 %.

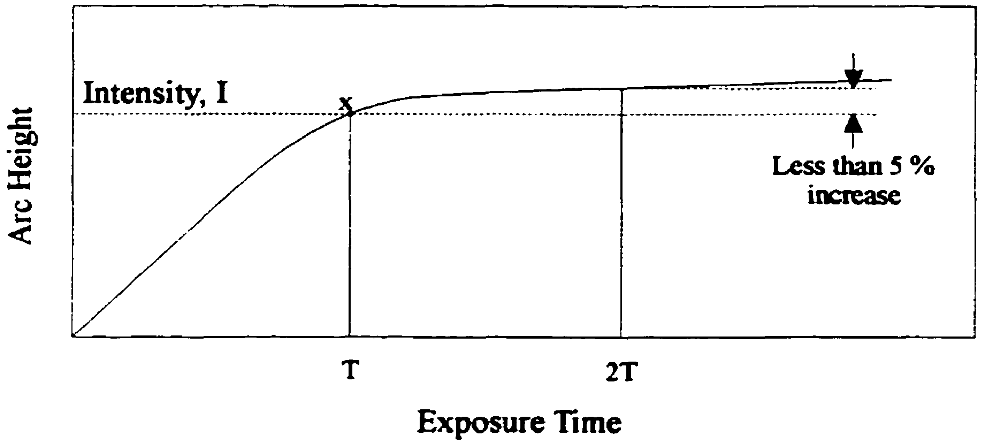

Fig. 2-9 Saturation curve showing relationship between arc height and exposure time.

Saturation curves can reveal a great deal about the suitability of given peening conditions for a particular application. Different peening conditions can be expected to produce different saturation curves. For example, if the peening intensity represented by point 'x' in Fig. 2-9 is lower than desired, it can be increased by increasing the shot velocity or shot size. If the characteristic intensity is too high, it may be decreased by decreasing the shot velocity or the shot size or both. After adjusting the peening conditions, a new series of Almen strips should again be exposed to the jet stream to determine the characteristic intensity under new conditions.

Peening Coverage

In order to understand what is meant by the term coverage, let us consider the following. Suppose in a peening process a target surface area A is exposed to the jet. Let the area produced by each particle striking the surface be S. Thus, even if the number of shots impinging on the target surface is A/S, the whole target area would not necessarily be covered by indentations. This is due to the nature of the process; some parts of the target surface will be struck by a shot more than once and others may escape. The ratio between the area of indentation produced by the shots S to the total exposed surface area to be covered by the shots A is the coverage.

In addition to establishing conditions for the characteristic peening intensity, one must determine the extent of coverage to be achieved in a given time under given peening conditions. This must be accomplished using the actual component.

In practice, the process users resort to the use of 5X and 10X magnifying glass and/or Dyescan tracers [45]. These techniques are subjective rather than objective, since they depend entirely upon the judgement and experience of the engineer performing the treatment. More recently, two reliable techniques to enable the accurate determination of peening coverage have been proposed by Meguid [46].

In the first technique, three dimensional surface roughness measurements were used to correlate peening coverage to surface conditions. In this case, the surface is mapped by making a number of closely spaced profile traces using a stylus-type instrument. Such a technique, however, requires large data handling capabilities, now readily available using computers, enabling the surface zone of interest to be scanned and a three dimensional surface description to be produced. Fig. 2-10 and Fig. 2-11 show typical isometric plots of peened surfaces and their contour representations for two different peening coverages, respectively.

In the second technique, coverage measurements are made using an image and area analyzer with television-type scanners. In this case, the image of the peened surface is formed on the t.v. scanner by an optical microscope, and a video signal is produced. After a number of image enhancing processes are performed on the signal, the peening coverage is obtained from the image contrast between peened and unpeened areas [46].

It is worth noting, however, that under certain circumstances, e.g. in the peening of complex geometries, it is difficult not only to achieve but also to monitor complete coverage. The presence of unpeened areas in a peened component may represent a problem to the designer, especially if the implications of incomplete coverage are not well understood. Research work related to the effect of partial coverage upon the fatigue performance of metallic components is very limited [46] and further investigations in this area are required [47, 48].

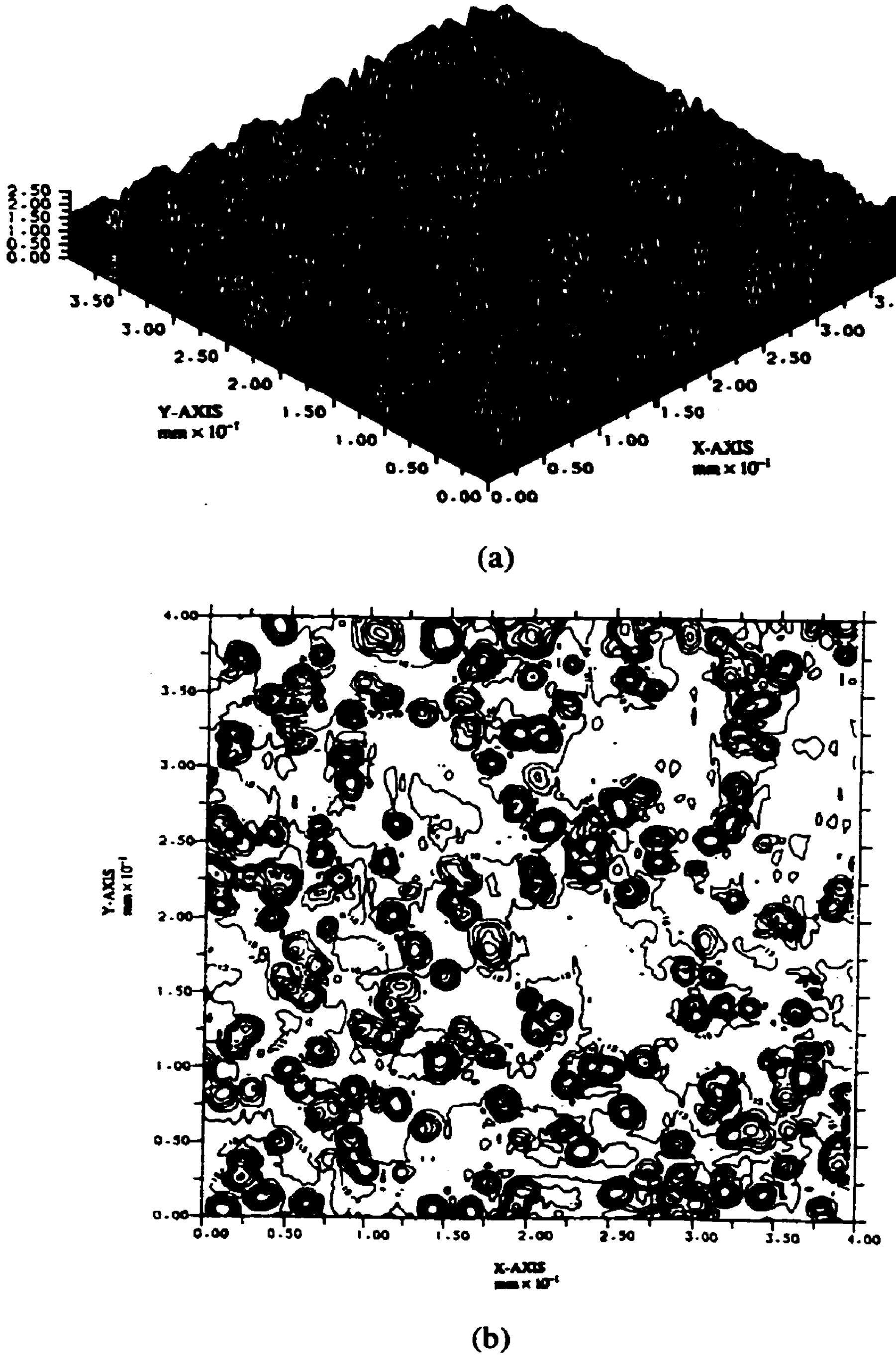

Fig. 2-10 (a) Isometric view and (b) contour representation of a peened area with 35% coverage, after Meguid [46].

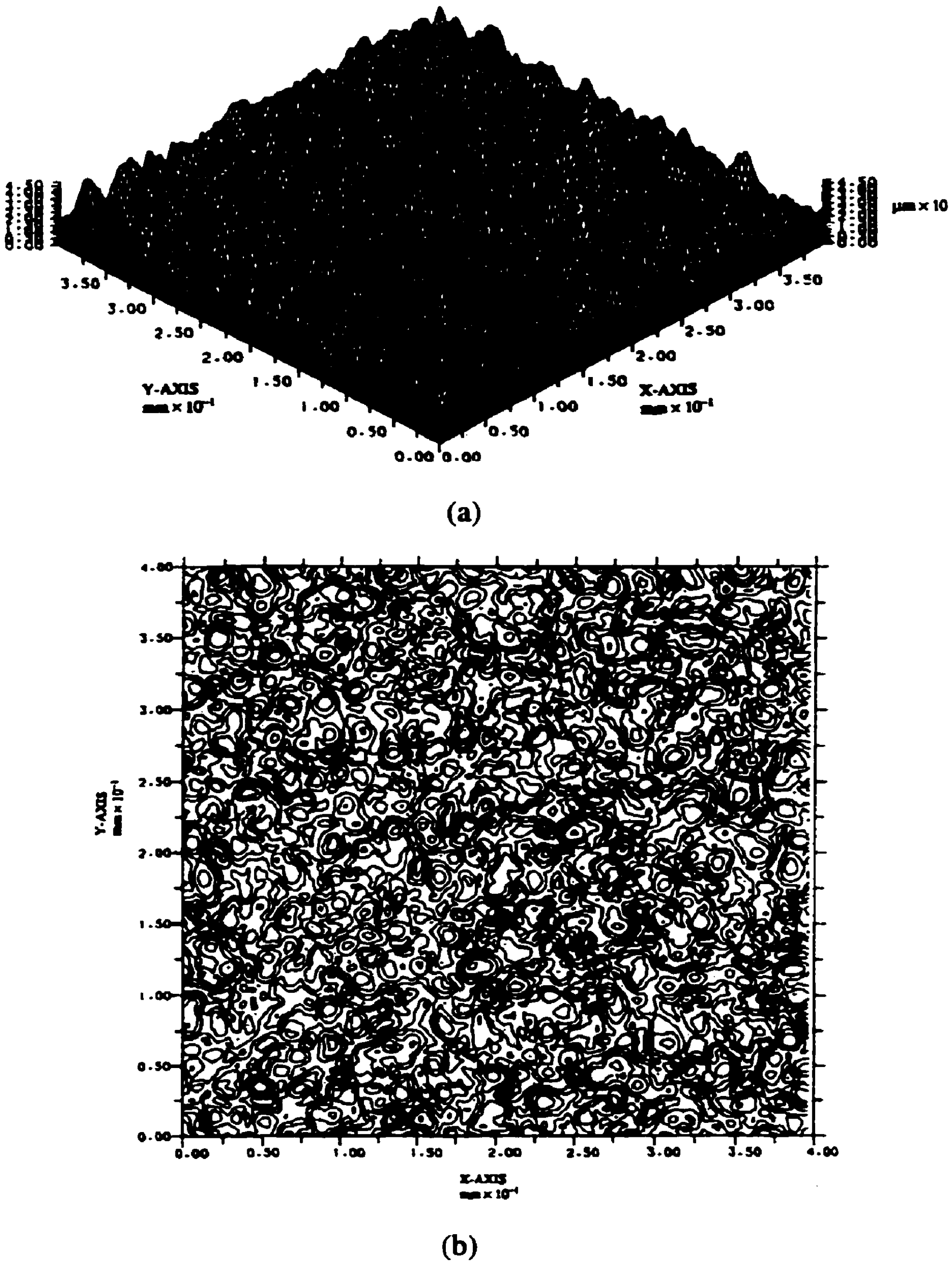

Fig. 2-11 (a) Isometric view and (b) contour representation of a fully peened area, after Meguid [46].

2.4 Characterisation of Mechanically Induced Residual Stress

Many models have been developed to predict or estimate the elastic and residual stress field resulting from features and operations which induce plastic deformation. In order to assess the validity of any technique or model, it must be evaluated against how well it reflects the stress field in the actual components it purports to model. The actual stresses in the component must be characterised, for which there exist a variety of techniques, both destructive and nondestructive, with varying levels of accuracy and capability. Existing applied and residual stress measurement techniques include: dissection method, hole-drilling, eddy current, Barkhausen, x-ray diffraction, neutron diffraction, ultrasonic technique and optical and thermal emission methods. The description, merits and limitations of these measurement techniques can be found in the review papers by Rund [49], Shackelford and Brown [50], and Meguid [51]. A brief synopsis is provided in the following section.

2.4.1 Destructive Techniques

Destructive or quasi-destructive techniques for measuring applied and residual stresses include: (i) the dissection method, (ii) x-ray diffraction and (iii) the hole drilling technique. In the dissection method, the change in shape of a component when a residually stressed layer of a material is removed is used to characterise the residual stress in that layer. As such, it is applicable only to thin components which exhibit measurable changes in curvature. In view of its limited accuracy and resolution, this technique is generally used to determine trends rather than actual field distribution. In the x-ray diffraction method, the angle of diffraction of the rays is related to the interlattice spacing of the different atomic planes. The residual stress field is then measured to a depth of 20 μm using the change in the spacing as a result of deformation. In order to determine stresses at greater depths, progressive layer removal, through careful machining or electro-polishing, is required. This introduces numerous difficulties with the technique. Of particular interest to this study is the hole-drilling technique.

The Hole Drilling Technique

The hole-drilling technique [52] is based on the fact that when a hole is introduced in a component containing residual stress field, the stresses at the location of the hole are relaxed. The elimination of these stresses at the hole surface changes the stress distribution in the the surrounding region, causing the local strains to change accordingly. By recording the relieved strains around the hole, the residual stresses in the material can be obtained using special calibration constants [53]. The relieved strains ε_1, ε_2 and ε_3 measured by a special strain gauge rosette typically (062RK or 031RE) are used to calculate the principal stresses, such that:

$$\sigma_I = \frac{\varepsilon_1 + \varepsilon_3}{4B} - \frac{\sqrt{2}}{4C}\sqrt{(\varepsilon_1 - \varepsilon_2)^2 + (\varepsilon_2 - \varepsilon_3)^2} \quad (2.1)$$

$$\sigma_{II} = \frac{\varepsilon_1 + \varepsilon_3}{4B} + \frac{\sqrt{2}}{4C}\sqrt{(\varepsilon_1 - \varepsilon_2)^2 + (\varepsilon_2 - \varepsilon_3)^2} \quad (2.2)$$

where σ_I and σ_{II} are the principal residual stresses, ε_1, ε_2 and ε_2 are the relaxed strains recorded and B and C are calibration coefficients. For residual stresses which are uniform with depth, the surface strains around the hole are fully relieved when the depth of the hole is equal to its diameter [52]. It is for this reason that residual stresses are often determined at a hole depth equal to hole diameter using calibration constants determined at full-hole depth in a uniform stress field [54, 55]. Although the calibration constants are available for a range of hole depths [53], *these cannot be used to compute non-uniform stress distributions, such as those encountered in shot peening.*

A number of methods have been proposed for measuring non-uniform residual stresses using the hole-drilling technique. These are the incremental strain [56, 57], the average stress [58], the power series [55] and the integral methods [59, 60, 61]. An extensive assessment of these techniques revealed that the integral method is the most fundamental and most suitable for accurately determining highly varying stress fields [62]. The approach adopts the finite element method to evaluate the calibration constants and thus relate non-uniform stress distributions to the relaxed strains associated with the incremental drilling of the hole.

Although a few studies reported the use of the integral method [59, 60], the results associated with the finite element calibration were not given. The only non-uniform calibration coefficients found in the literature are those given by Schajer [61]. Application of the available technique is unsuitable, as the smallest increments developed are several times larger than the depths of interest. In order to extend the technique for the large gradients and shallow depths addressed in this study, work was needed in five areas: refinement of the inversion increments, accurate determination of the initial contact with the workpiece, filtering of noise in the recorded signal, data collection and management, and the verification of the enhanced technique.

2.4.2 Nondestructive Techniques

Nondestructive methods for residual stress measurement include electromagnetic, nuclear and acoustic based techniques. Electromagnetically-based nondestructive techniques include eddy current and Barkhausen noise measurement. The eddy current technique employs a wire coil in close proximity to the component being tested. The induced eddy current changes due to material variations (plasticity, stress and chemical composition), which in turn affects the measured coil impedance. These changes can then be used to characterise the residual stress state of the component. The technique is sensitive to microstructural variations and is limited to ferromagnetic materials [63].

The Barkhausen noise technique, on the other hand, hinges on the discontinuous magnetization of a component subjected to a varying magnetic field. Due to the polycrystaline nature of metals, the induced magnetic field changes in a step-like manner. These steps are generally proportional to the composition, microstructure, temperature, and the induced stress in the material. A correlation can then be determined between the stresses in the material and the Barkhausen noise level. The disadvantages of this technique are: (i) sensitivity to microstructural variations, (ii) limited stress range measurement and (iii) only a thin surface layer can be measured [64].

Similar to x-ray diffraction, neutron diffraction can be used to examine the applied or residual stress profiles within a material. The diffraction angle of the rays is related to the interlattice spacing of the different atomic planes. Under suitable conditions, profiles up to several centimeters in depth can be evaluated. However, the technique requires large capital costs and has considerable potential hazards as the neutron source is a nuclear reactor.

In view of its deeper penetration, absence of potentially hazardous operating conditions, relatively low capital cost and the associated acoustoelastic effects, research efforts have been made to measure stress ultrasonically. Numerous techniques have been employed. These include longitudinal bulk waves, shear bulk waves, birefringent shear waves, surface skimming waves and wave harmonics.

The longitudinal wave technique measures the change in speed of a longitudinal wave travelling perpendicular to the plane of stress [65, 66]. The change of flight time is measured through several techniques, such as pulse-echo overlap, ultrasonic sing-around, pulse repetition and pulse interval measurement. A similar technique has been developed employing shear waves. The shear waves are generated when a water coupled longitudinal wave strikes the specimen between the longitudinal and shear critical angles of the material [67]. The oblique path travelled by the shear waves limits the usefulness of this technique to thin sections. A third technique is based on the birefringence of the acoustic shear wave in a stress field [68]. In this case, ultrasonic shear waves transmitted perpendicularly across the stress field develop a phase shift proportional to the difference in principal stresses. All of these techniques have generally been applied to specimens assuming a constant through thickness stress. Depth varying stress can only be measured if there is access to a surface perpendicular to the plane containing the stress variation. Stresses near the surface cannot be measured due to edge-scattering of the wave [65].

Surface or surface skimming wave techniques have been developed in an attempt to measure near surface stress gradients. Examples of these techniques include the work of Hirao [69] who investigated the use of Rayleigh waves and Bray et al. [70] who employed critically refracted longitudinal waves. Both of these techniques result in a change in the wave velocity due to the averaged stress over the depth of penetration. In this case, the penetration depth is governed by the wavelength or frequency of the propagated wave. Both of these works employed contact transducers.

Wave harmonics have also been used to examine the stress at a point [71]. The principle of measurement in this case relies on the premise that when two beams, either longitudinal or shear waves, intersect at an angle a third beam will emerge from the intersecting point when a resonant condition occurs. The amplitude of the resulting beam has been found to be a function of the applied stress [71]. However, prior knowledge of the material variation is required to be able to focus the beam at the appropriate position.

Leaky Lamb Wave

In spite of the limited success in determining the applied stress field, ultrasonic techniques continue to hold great promise. Specifically, it is postulated that guided waves (leaky Lamb waves) can successfully be used to determine the residual stress field in engineering components. The reasons for this are outlined below.

The leaky Lamb wave (LLW) method provides richer information and better diagnosis of the in-depth changes of wave speeds in the material than body-wave and surface-wave methods [72-75]. In the LLW method, a transducer insonifies a small area of the immersed test component at an oblique angle. The wave is refracted as well as mode converted to include guided waves which propagate parallel to the surface of the test component. To maximize the guided wave interaction with the specular reflection, the emitting and receiving transducers must be at equal angles and their height above the test component must be carefully adjusted to generate a null zone in the recorded signals. As a result of the destructive interference of the specularly reflected part and the guided wave, minima are introduced to the amplitude spectrum of the received reflected signals (Fig. 2-12). The locations of the minima in the frequency domain are used in the LLW method to quantify the wave speeds of the test sample. These minima can be precisely located and are sensitive to subsurface and in-depth acoustoelastic changes [74, 75]. The profile of the wave speeds in the test component can then be obtained through inversion of the measured data by using the leaky Lamb wave theory. The non-contact nature of the LLW method allows for a thorough scan of the sample and the acquisition of the Lamb modes at desired locations.

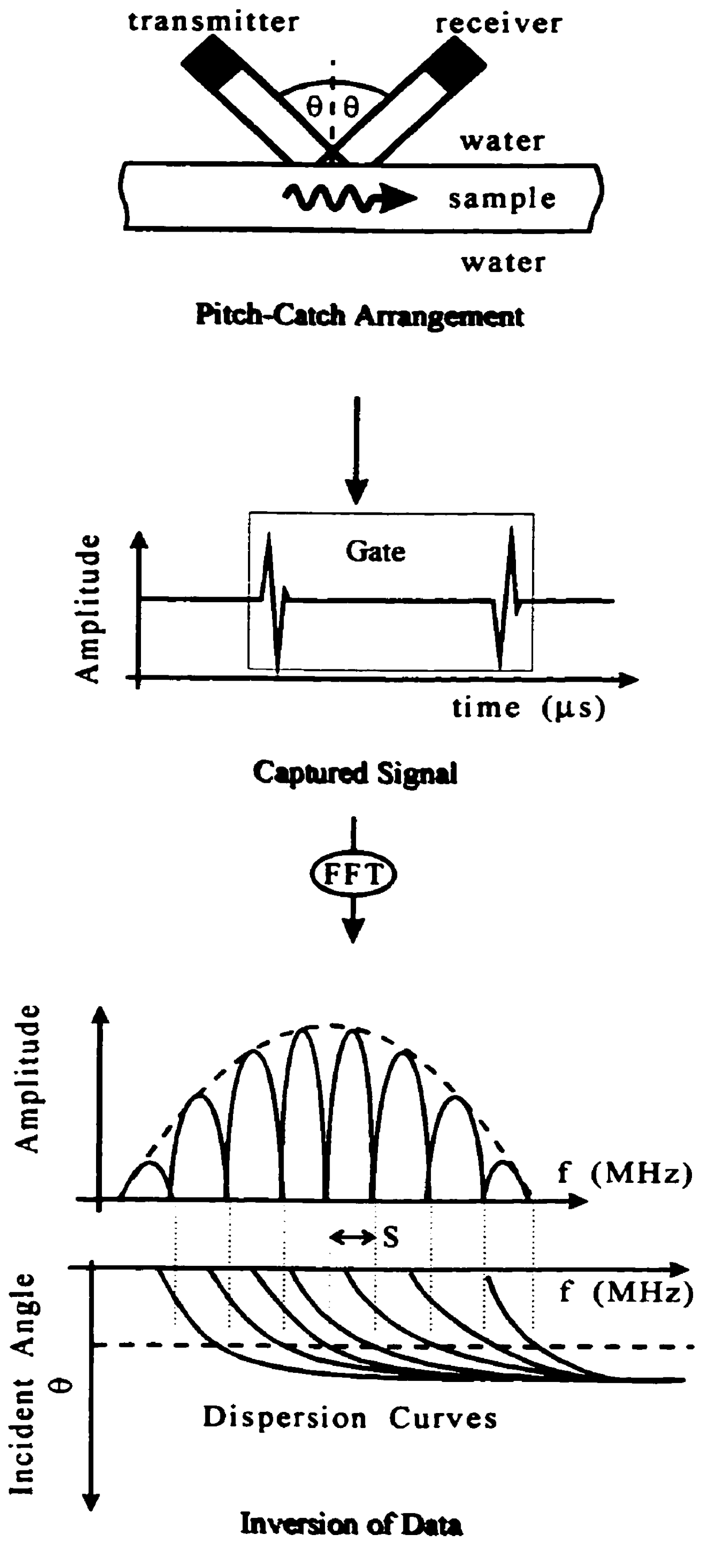

Fig. 2-12 Schematic of the leaky Lamb wave technique.

Chapter 3 Finite Element Modelling of Mechanically Induced Residual Stresses

Summary: In this chapter, two non-linear finite element models are developed. The first, which is quasi-static, simulates the cold expansion of two fastener holes, while the second, which is dynamic, is devoted to the modelling of the shot peening process. Both models were carried out using the commercial finite element code ANSYS. In these models, material and geometrical non-linearities, contact and load history were carefully considered in determining the plastic zone development, its growth and the resulting unloading residual stresses. The FE models were then validated using an extensive test program detailed in the following chapter. This chapter also treats the modelling of the leaky Lamb wave and the effect of a varying stress profile upon the dispersion modes of a tested component.

3.1 Mechanically Induced Residual Stresses

Mechanically induced residual stresses develop in metallic materials as a result of inhomogeneous plastic deformation followed by unloading. In the following sections, two examples are considered: cold expansion of two fastener holes in close proximity and shot peening of metallic targets. These cold working treatments are generally characterised by inhomogeneous plastic deformation, contact stresses, loading history dependence, strain rate effects and interaction effects. It is with this in mind that we examined the above mentioned techniques.

In the following sections, we summarise the approach adopted in developing the quasi-static finite element model used to simulate the cold expansion process and the dynamic model of the shot peening process. In both cases, the model was treated using three dimensional elements and accounted for the main parameters that influence the resulting plastic zone and residual stresses.

3.2 Cold Hole Expansion

As indicated earlier, residual stresses resulting from the inhomogeneous plastic deformation of cold worked fastener holes extend the fatigue life of the hole. It is the purpose of this section to employ the finite element method to characterise the mechanically induced residual stress field. Existing work in this area has concentrated on a single hole model, where the residual stress field can be obtained from simple analytical and/or numerical two dimensional analyses. The most recents efforts to address this problem were carried out by Papanikos [36]. However, his work was devoted to fatigue crack growth and primarily examined two dimensional analyses. The importance of examining the effect of separation distance, size and orientation of adjacent fastener holes on the three dimensional residual stress field is apparent for the damage tolerant design of airframes. This chapter addresses these issues using three dimensional elasto-plastic finite element analysis of cold worked holes made from aluminium 7075-T651. However, for the sake of comparison with the three dimensional solution, as well as completeness of the work, some attention was devoted to two dimensional analysis. This allowed the establishment of baseline values for the field variables. Throughout this work, the ANSYS finite element code was utilised.

3.2.1 Two Dimensional Finite Element Model

A plane stress finite element model was conducted, along the lines proposed by Papanikos, using a plate containing two holes each of radius R with a centre distance $2c$ between the holes, as shown in Fig. 3-1(a). The dimensions of the plate were: width w=40R and height h=40R. These dimensions were determined carefully, so as to avoid the effect of the boundary on the results. In view of symmetry, only one quarter of the plate was discretised. Six-noded triangular elements were used. A higher density mesh was used in the neighbourhood of the hole to capture the large stress variation in that region.

A number of convergence runs were conducted using different discretised geometries. As a compromise, the mesh provided in Fig. 3-1(b) was selected for the two dimensional analysis. The expansion level was imposed by applying a radial displacement at the hole boundaries. This assumes a rigid mandrel configuration. The mechanical properties of the target material are provided in Table 3-1.

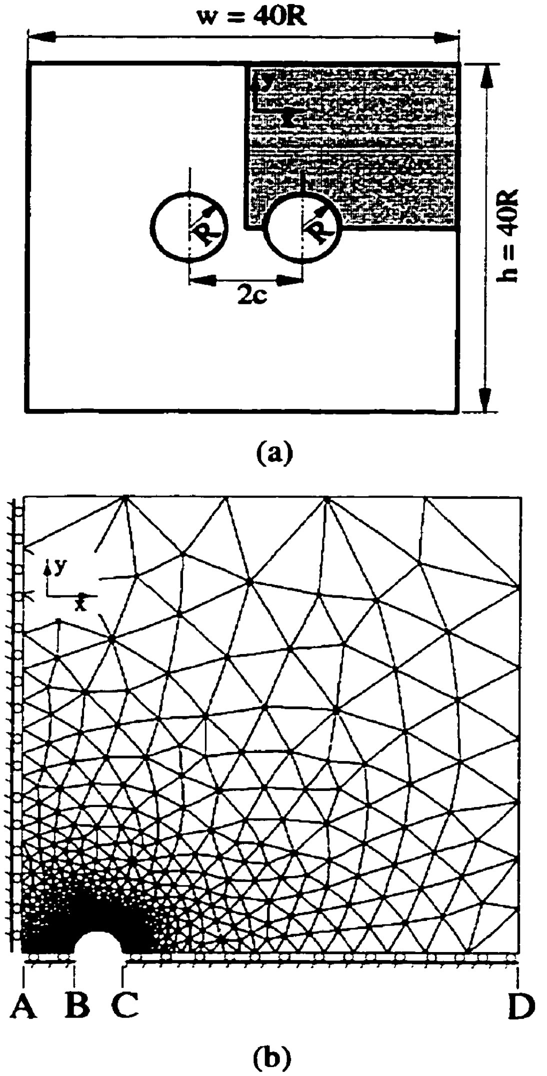

(a)

(b)

Fig. 3-1 Cold expansion of two adjacent holes: (a) schematic of geometry used, and (b) finite element mesh.

Attention was then devoted to the case where the expansion was conducted sequentially. Fig. 3-2 shows the discretised mesh for the geometry. In this case, an alternate expansion of 4% was applied to each of the holes.

Property	Value
Young's Modulus, E [GPa]	72.32
Poisson's Ratio, ν [-]	0.32
Initial Yield Stress, σ_0 [MPa]	506
Strain Hardening Coefficient, H' [MPa]	360 (0.5% E)

Table 3-1 Material properties of hole expansion model.

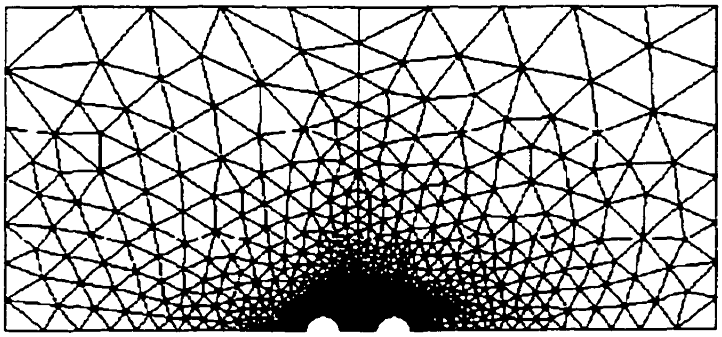

Fig. 3-2 Finite element mesh used for the sequential expansion of the two holes.

3.2.2 Three Dimensional FE Model of Two Adjacent Holes

Unlike the earlier work of Papanikos on a single expanded hole [36], the current thesis examines the elastoplastic behaviour of a plate containing two holes each of radius R with a centre distance c between the holes, as shown in Fig. 3-3(a). The dimensions of the plate were: width $w=2c+12R$, height $h=12R$ and thickness $t=1.2R$. These dimensions were determined carefully so as to avoid the effect of the boundary. The results presented were

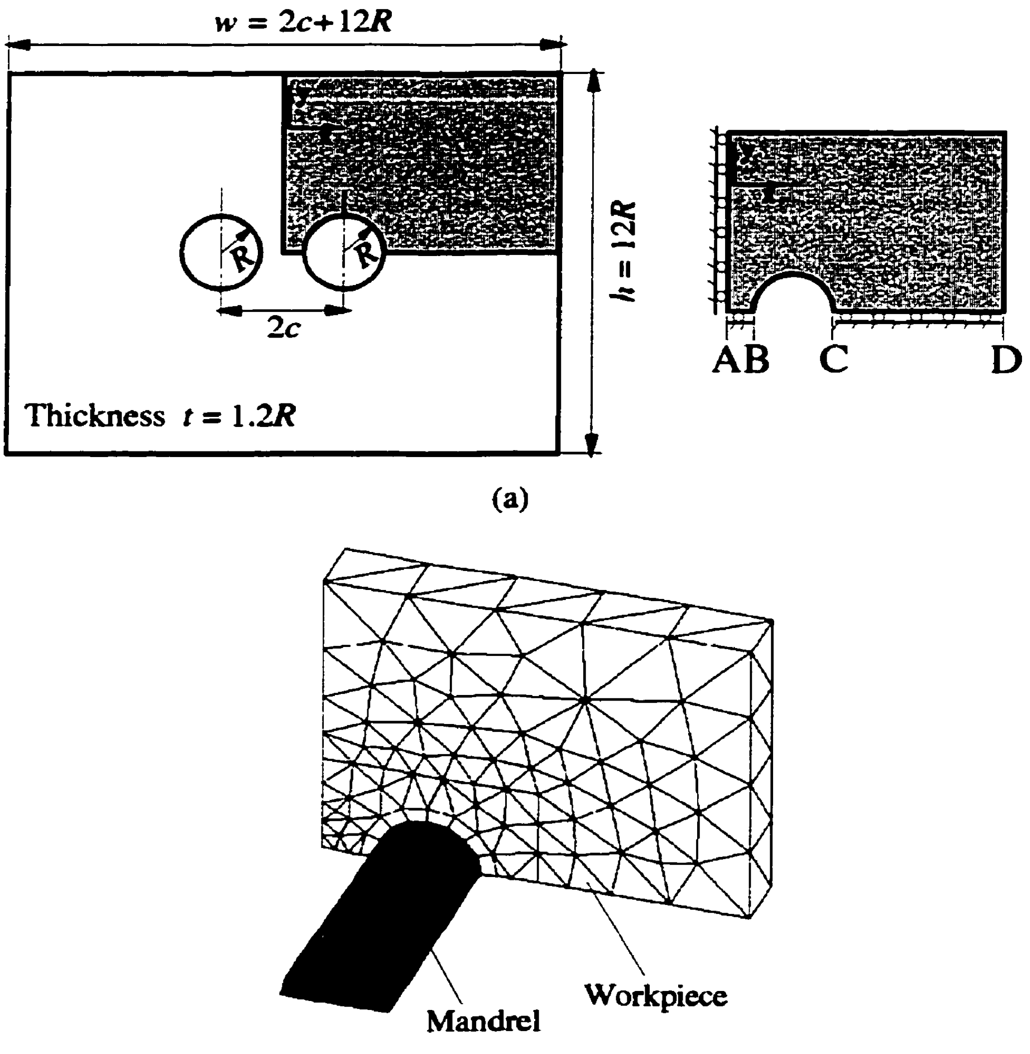

(a)

(b)

Fig. 3-3 Cold expansion of two adjacent holes: (a) schematic of geometry used, and (b) 3D finite element mesh.

obtained for R=2.5 mm. In view of symmetry, only one quarter of the plate was discretised. Twenty-noded hexahedral elements were used in the neighbourhood of the mandrel to capture the large stress variation in that region. The remaining region of the plate was conveniently discretised using ten-noded tetrahedral elements. A number of convergence runs were conducted using different discretised geometries and the mesh provided in Fig. 3-3(b) was selected for the investigation.

The interface between the mandrel and the hole surface was modelled using contact elements. The three dimensional contact element used, depicted in Fig. 3-4, adopts a contact node-target segment approach in conjunction with the penalty function method. Elastic Coulomb's friction with a coefficient of friction $\mu=0.15$ was used.

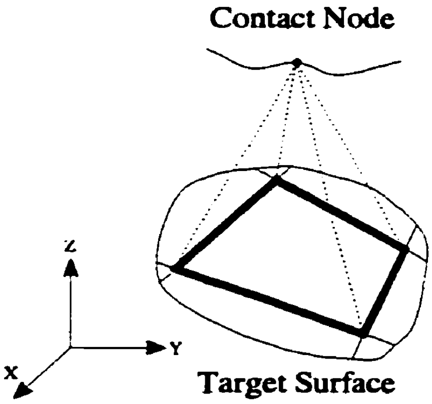

Fig. 3-4 Schematic of three dimensional contact element used.

A major problem in the implementation of contact elements is the assignment of values to the normal (K_n) and tangential (K_t) stiffnesses, which govern the convergence and accuracy of the solution. The values of K_n and K_t are required to be very large. However, the use of excessively high values of K_n and K_t results in ill-conditioned global stiffness matrices, leading to numerical errors and divergence. On the other hand, the use of smaller values of K_n and K_t results in convergence to the wrong solution allowing for large interpenetration and incorrect estimates of the stick and slip regions. In the current study, the appropriate values of the normal and tangential stiffnesses were selected from convergence tests, where only minimal interpenetration was allowed. As a result of numerous test runs, the following values of K_n and K_t were selected: 10^{12} and 10^{8} N/m, respectively.

Validation of Three Dimensional Finite Element Model

A model specifically tailored to the instrumented plate (detailed in section 4.2) was developed as part of the verification of the finite element results. The model of the sequential expansions of adjacent holes, accounting for friction, was then compared to the actual test data of the expansion process. The details of the model are provided in Fig. 3-5 and Fig. 3-6. Due the interaction between the materials and lubricants in the interference fit of the expanded holes during the expansion process, it was difficult to assess the appropriate coefficient of friction. Guidelines indicated that the value could fall between 0.03 and 0.45 for the steel mandrel through an aluminium plate [76]. In order to address this, reduced three dimensional models, shown in Fig. 3-6 (a), were first investigated to select a suitable coefficient of friction. The results for μ= 0.0, 0.15 and 0.3 were compared with the recorded strains at equivalent locations from the actual sequential expansion (4.2) of the plate. The results indicated that μ=0.30 was the most suitable selection for the specific case of the steel mandrel expanding the 7075-T651 plate.

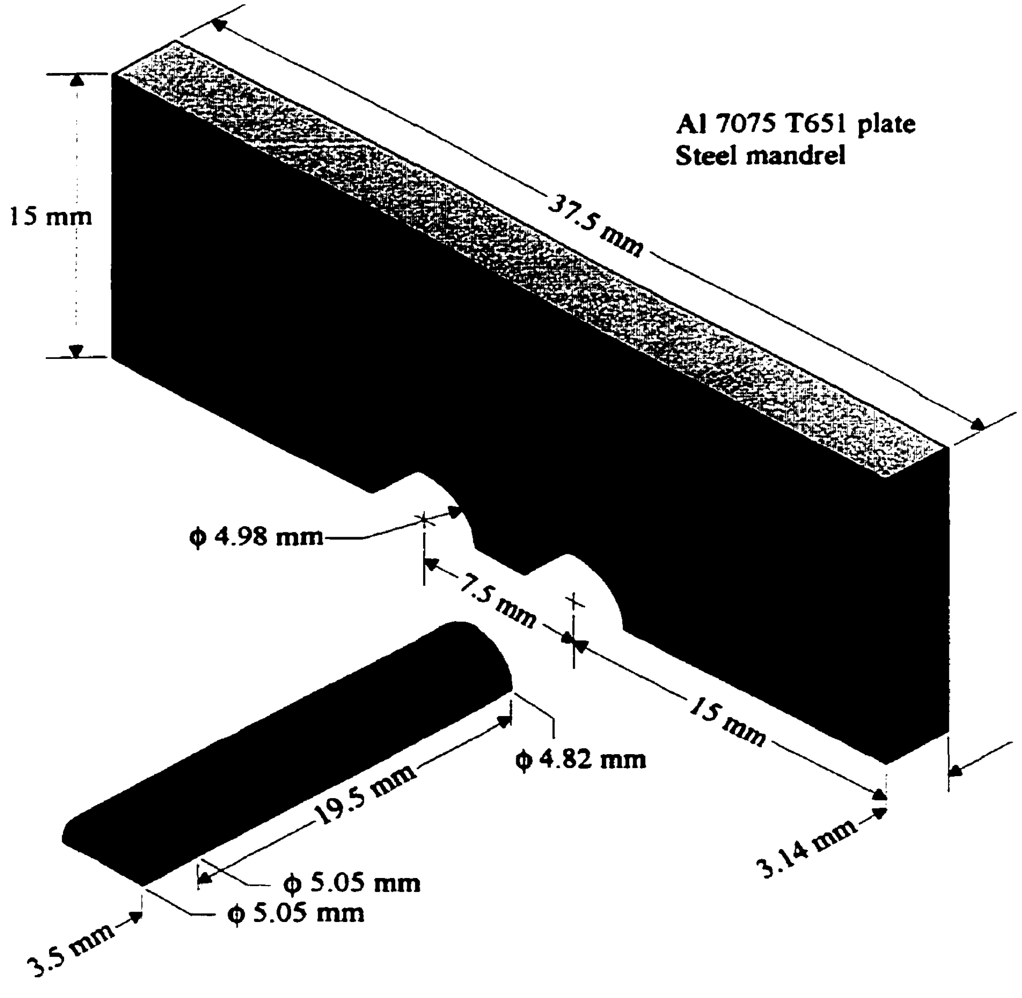

Fig. 3-5 Details of hole expansion model.

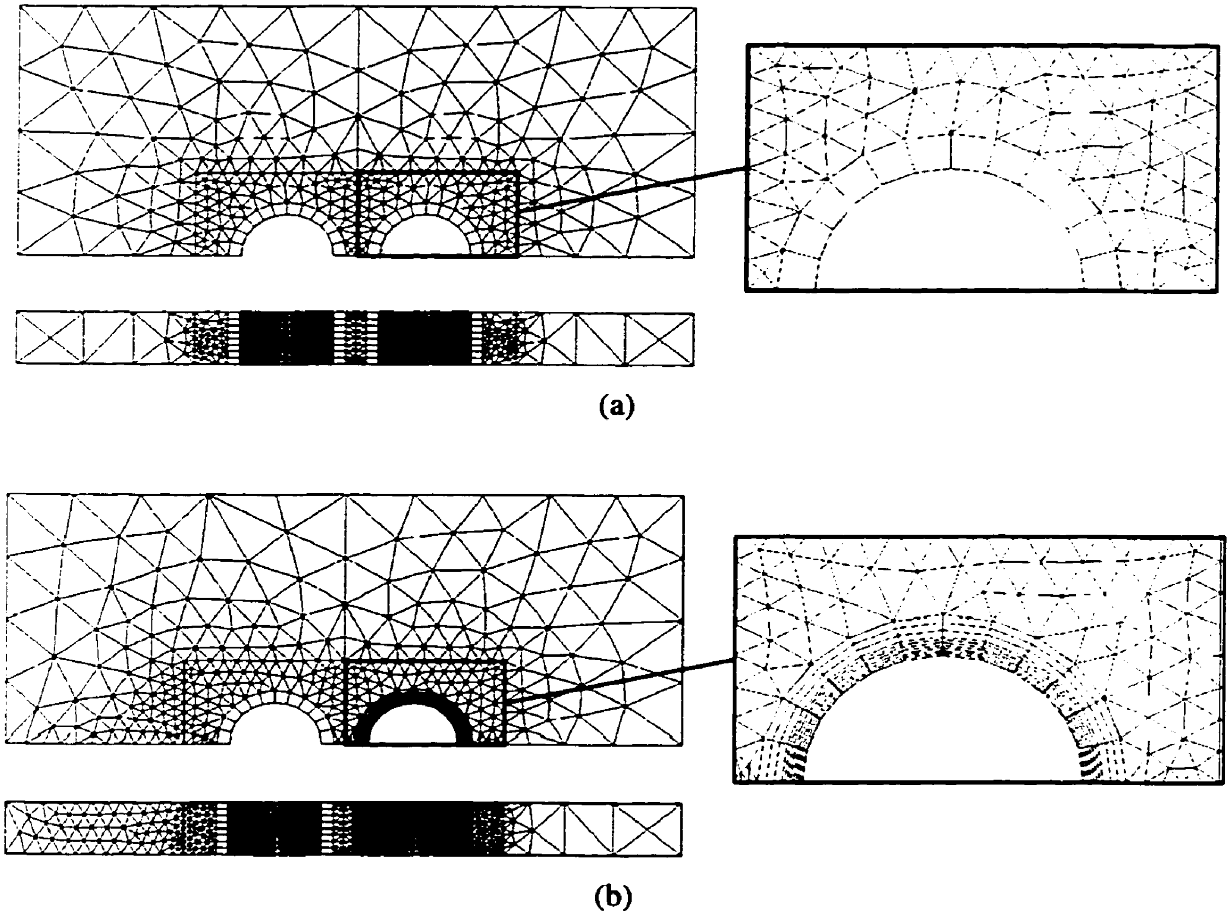

Fig. 3-6 **Different meshes used to model expansion and reaming tests (a) friction verification models and (b) high resolution model.**

3.3 Three Dimensional Dynamic FE Modelling of Shot Peening

Four main models were considered using the commercial finite element code ANSYS. The first was concerned with a single shot impinging at normal incidence, the second was a single shot impinging the target obliquely, the third was twin shot studies and the final model was of multiple shots impinging at normal incidence.

3.3.1 Three Dimensional Dynamic Single Shot Model

Due to symmetry, only one quarter of the single shot model was discretised, as depicted in Fig. 3-7(a). The following dimensions were selected for the target: width W=7R, height H=4R and breadth B=5R, where R was the radius of the shot. These dimensions were carefully determined as a result of numerous axisymmetric model analyses to establish the effect of the boundary [47, 48]. The target material properties are provided in Table 3-2.

Both eight-noded brick and four-noded tetrahedral finite elements, with large strain and displacement capabilities, were used to discretise the target. In view of their higher accuracy, brick elements were used in the impact region around the common normal. The remaining regions of the target were conveniently discretised using tetrahedral elements. Convergence tests were conducted using the meshes depicted in Fig. 3-7 (b-d), revealing only minor distortion.

Property	Value
Young's Modulus, E [GPa]	210
Poisson's Ratio, ν [-]	0.28
Initial Yield Stress, σ_0 [MPa]	600
Strain Hardening Coefficient, H' [MPa]	50, 800, 1600 (0.025, 0.4, 0.8% E)

Table 3-2 Material properties of shot peening model.

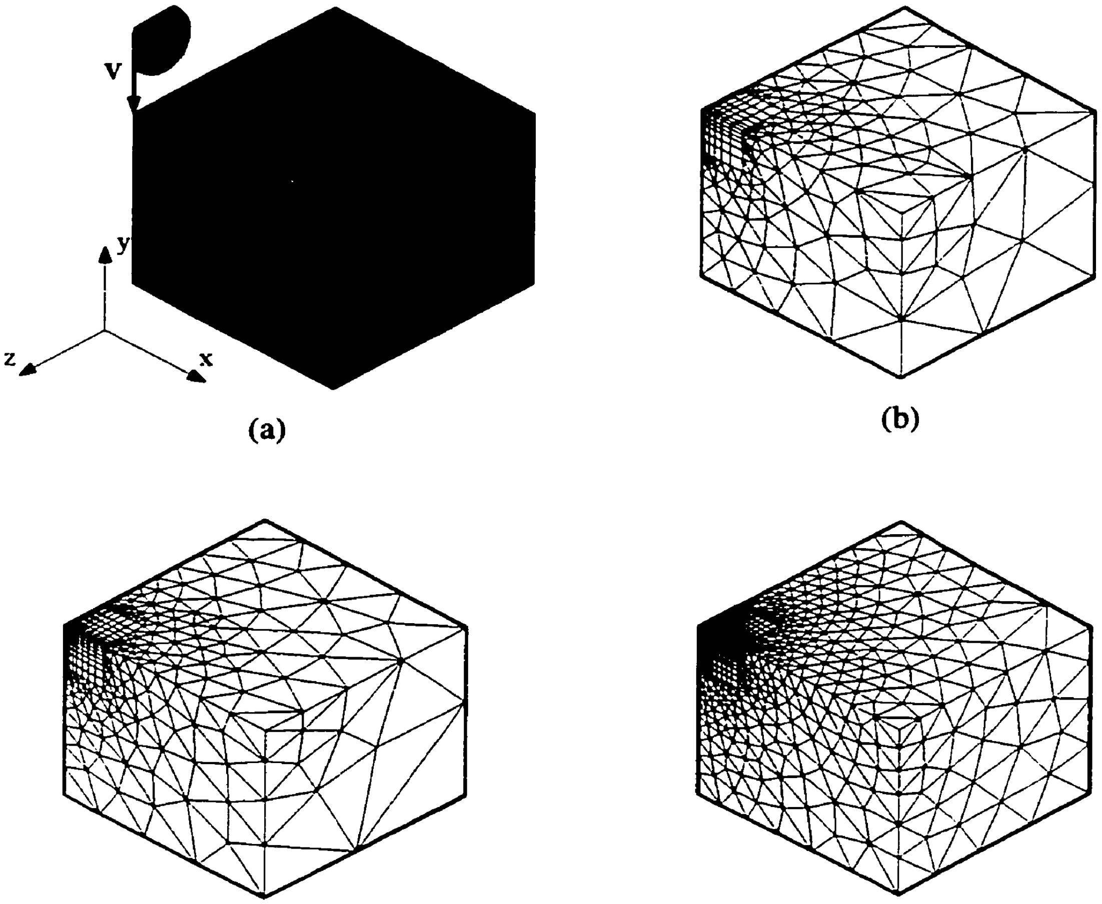

(a) (b)

(c) (d)

Fig. 3-7 Geometry and discretised models used in the single shot model: (a) one-quarter of geometry, and (b), (c) and (d) three discretised geometries of target with different mesh densities.

To model the shot-target interface, contact elements were used on both bodies. The three dimensional contact elements adopt a contact node-target surface approach in conjunction with the penalty function method [77]. The contact nodes were created on the top surface of the peened target around the common normal. The target segments were generated only on the lower half of the shot surface (Fig. 3-7), since contact would take place only in that area. Elastic Coulomb's law, with friction coefficient μ=0.25, was used.

As detailed in section 3.2.2 above, the selection of the penalty parameters for the contact elements must be carefully selected. After several trial runs in which the values of K_n and K_t were tested, the values of 10^8 N/m and 10^6 N/m were selected, respectively.

A number of preliminary runs were conducted to establish the appropriate mesh design and to ensure the convergence of the model. The dynamic analysis was carried out using Newmark implicit time integration scheme with adjustable time steps. The total integration time was t_k=10 μs. As a result of these runs, the mesh given in Fig. 3-7(b) was used for the single shot dynamic analysis.

Oblique Shot Model

In practice, the majority of shots do not impinge normal to the surface of the component. The reasons for this are twofold. Firstly, the geometries being treated can be quite complex and access to the surface to be treated may not be direct. Secondly, there is a degree of randomness in the process. As discussed in Chapter 2, shots are either carried by a stream of air or are mechanically accelerated against the target using a bladed wheel. As well as the resulting spread, there occurs contact and impact of different shots within the stream, as well as with the shots rebounding from the target. The perfectly normal incident contact may well be a rarity. To investigate the effect of possible shot obliquity, the single shot impact model was extended to half-symmetry. The angle of impingement was then varied between 0° and 60° from normal incidence and the coefficient of friction μ was varied from 0.0 to 0.8 at a selected incident angle of 45°.

Strain Rate Effects

The behaviour of materials under high strain rates may differ significantly from that observed in quasi-static loading. Rate sensitivity is observed primarily as a variation of the yield and flow stresses. As a result, it is necessary to determine the behaviour of the material under conditions which match the expected deformation rates in the process. In view of the fact that the impingement during the peening process takes place in a very short time, it is anticipated that strain rates will be quite large and that strain rate effects will play a significant role in determining the peening effects. Various empirical expressions have been proposed to represent uniaxial strain rate sensitivity [78-81]. The expressions result from the best fit to strain rate test data. These include polynomial, power law and logarithmic expressions. Cowper and Symond found that the simple empirical equation

$$\dot{\varepsilon}^{pl} = C\left(\frac{\bar{\sigma}}{\sigma_o} - 1\right)^p \qquad (3.1)$$

provided a reasonable estimate of the dynamic flow stress recorded during many dynamic, uniaxial constant strain rate tests on mild steel [82, 83]. In (3.1), $\dot{\varepsilon}^{pl}$ is the plastic strain rate, $\bar{\sigma}$ is the equivalent stress, σ_o is the initial yield stress and C and p are material constants. Jones [84], in examining structural collisions, proposed values of C=1300 and p=5.

Accordingly, a number of runs were carried out with LS-Dyna 3D using the Cowper and Symond model. It is worth noting that the strain rates experienced during the peening process are very high, on the order of 10^6 per second. Material data in this range does not exist in the literature. It was therefore decided to employ the coefficients proposed by Jones to:

(i) examine the effect of strain rate on the global behaviour of the material,
(ii) compare the resulting field with rate independent model to highlight any possible anomalies, and
(iii) to obtain an estimate of the influence of strain rate effects upon the resulting residual stress field.

3.3.2 Three Dimensional Dynamic Twin Shot Model

The study was extended to examine the effect of twin shot impact upon the residual stress field. Fig. 3-8(a) shows two spheres each of radius R impinging a target. The separation distance between the spheres is 2C. Fig. 3-8(b) shows the discretised geometry of the target using the same element types discussed earlier. The boundary conditions imposed on the above models were as follows: symmetry boundary conditions on the z=0 and x=0 planes, and a fully constrained workpiece bottom surface. For the purpose of this study,

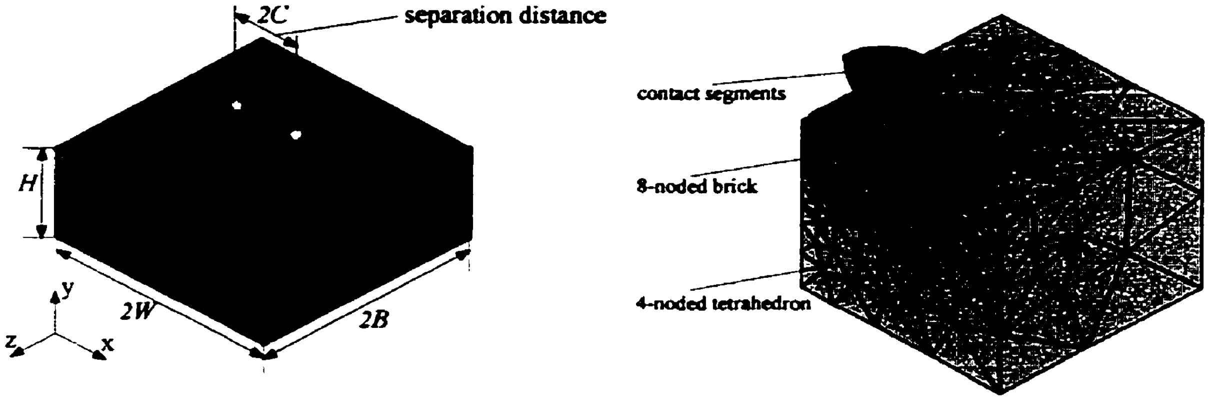

(a) (b)

Fig. 3-8 Geometry and discretised model used in dynamic simultaneous impact studies: (a) geometry and notation used and (b) discretised geometry showing contact elements.

the shot was assumed to be rigid. This rigidity stems from the relatively high yield and hardness values of typical steel shots compared to the target material. It is worth noting that the effect of strain rate and elastic wave propagation was not considered in the study.

3.3.3 Multiple Shot Model: Shot-peening

The research was further extended to examine the effect of multiple simultaneous and sequential impacts on the plastic zone development and growth, and the resulting residual stress field. Four successive waves of impacting shot were modelled, as depicted in Fig. 3-9. By ignoring boundary effects, this model could be discretised into the symmetry cell shown in Fig. 3-9(b). The spatial separation of the shot within a wave was varied between C=R and C=2R. This corresponded to the case of sequential waves overlapping or impinging adjacent to the previous shots location. The depth of the cell was again taken to be H=4R to eliminate/minimize boundary effects. The shot was modelled as rigid and the target as having the properties in Table 3-2, and no interference between subsequent waves of shot was assumed.

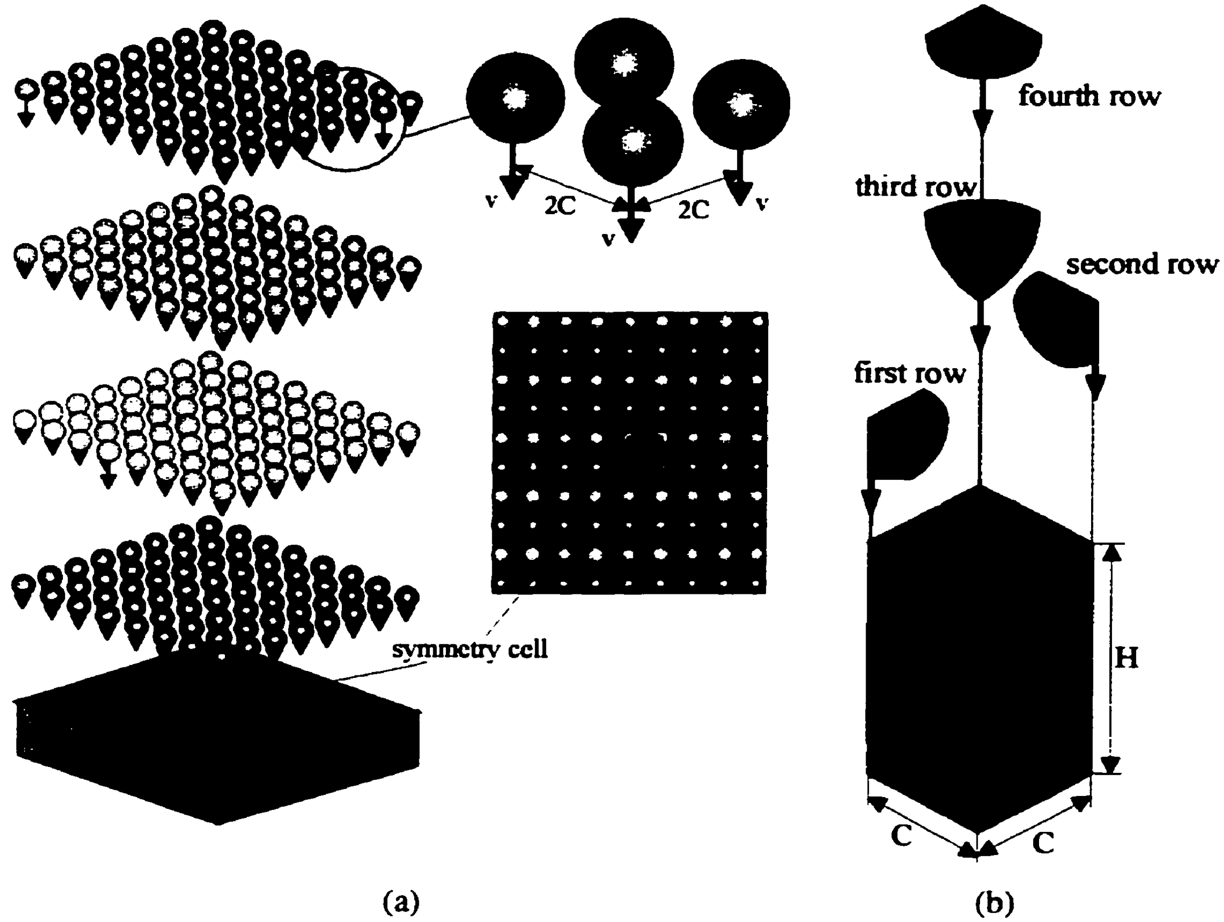

(a) (b)

Fig. 3-9 Geometry and discretised model used in multiple shot studies: (a) overview of the model, and (b) discretised geometry of the symmetry cell.

3.4 Leaky Lamb Wave Modes

The theoretical foundation for the modelling of the Lamb wave propagation [85] and the variation thereof due to applied and residual stresses in plates is based upon the wave equation:

$$\sigma_{ij,j} = \rho \ddot{u}_i \tag{3.2}$$

For propagation in an isotropic plate, the equation becomes:

$$(\lambda + \mu) u_{j,ji} + \mu u_{i,jj} = \rho \ddot{u}_i \tag{3.3}$$

where λ and μ are the Lamé constants. Considering the in-plane (P-SV) case, we denote the displacements as u_x, u_z and the stresses as $\tau_{xx},\tau_{zz},\tau_{xz}$. The potentials ψ and φ are introduced such that

$$\begin{pmatrix} u_x \\ u_z \end{pmatrix} = \begin{bmatrix} \partial/\partial x & -\partial/\partial z \\ \partial/\partial z & \partial/\partial x \end{bmatrix} \begin{pmatrix} \varphi \\ \psi \end{pmatrix} \tag{3.4}$$

and

$$\begin{pmatrix} \tau_{xx} \\ \tau_{zz} \\ \tau_{xz} \end{pmatrix} = \begin{bmatrix} \lambda \nabla^2 + 2\mu \partial^2/\partial x^2 & -2\mu \partial^2/\partial x \partial z \\ \lambda \nabla^2 + 2\mu \partial^2/\partial z^2 & 2\mu \partial^2/\partial x \partial z \\ 2\mu \partial^2/\partial x \partial z & \mu(\partial^2/\partial x^2 - \partial^2/\partial z^2) \end{bmatrix} \begin{pmatrix} \varphi \\ \psi \end{pmatrix} \tag{3.5}$$

A time harmonic dependency of the problem is assumed, and as a result the time dependence $e^{-i\omega t}$ in all field quantities is suppressed, where ω is the circular frequency. Accordingly ψ and φ represent solutions of the reduced system of equations, viz.

$$\nabla^2 \psi + k_s^2 \psi = 0 \tag{3.6}$$

$$\nabla^2 \varphi + k_p^2 \varphi = 0 \tag{3.7}$$

where k_p and k_s are the wave numbers associated with the P (longitudinal) and S (shear) waves, respectively. Assuming a biharmonic form of solution for ψ and φ leads to:

$$\varphi(x,z) = (A_1 \sinh(\nu_p z) + A_2 \cosh(\nu_p z)) e^{ikx} \tag{3.8}$$

$$\psi(x,z) = \left(B_1 \sinh(v_S z) + B_2 \cosh(v_S z)\right)e^{ikx} \tag{3.9}$$

with
$$v_P = \sqrt{k^2 - k_P^2}; \quad v_S = \sqrt{k^2 - k_S^2};$$

$$k_P = \frac{\omega}{V_P}; \quad k_S = \frac{\omega}{V_S};$$

$$k = k_P \sin\theta$$

and
$$V_P = \sqrt{\frac{\lambda + 2\mu}{\rho}}; \quad V_S = \sqrt{\frac{\mu}{\rho}}$$

where A_1, A_2, B_1, B_2 represent the respective incident and transmitted waves at the upper and lower boundaries of the plate. Ewing et al. [85] expressed the symmetric and antisymmetric dispersion (Fig. 3-10) equations resulting from the general solution of the wave equation in the form :

$$\frac{\tanh[v_P(h/2)]}{\tanh[v_S(h/2)]} = \frac{(v_S^2 + k^2)^2}{4k^2 v_P v_S} \tag{3.10}$$

$$\frac{\tanh[v_P(h/2)]}{\tanh[v_S(h/2)]} = \frac{4k^2 v_P v_S}{(v_S^2 + k^2)^2} \tag{3.11}$$

where h is the thickness of the plate. For an isotropic solid at high frequencies, between the longitudinal and shear wave critical angles, the spacing S between adjacent modes can be expressed as

$$S = \frac{1}{2h}\left[\frac{1}{V_S^2} - \frac{\sin^2\theta}{V_{water}^2}\right]^{-1/2} \tag{3.12}$$

where it is assumed that the solid is immersed in a water bath and a plane wave impinges at an angle θ to the surface normal [73].

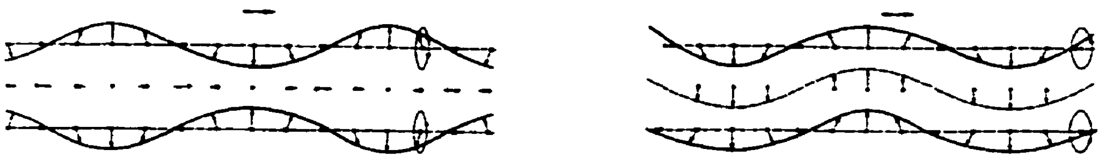
(a) (b)

Fig. 3-10 Lamb modes for an isotropic plate: (a) symmetric and (b) antisymmetric modes.

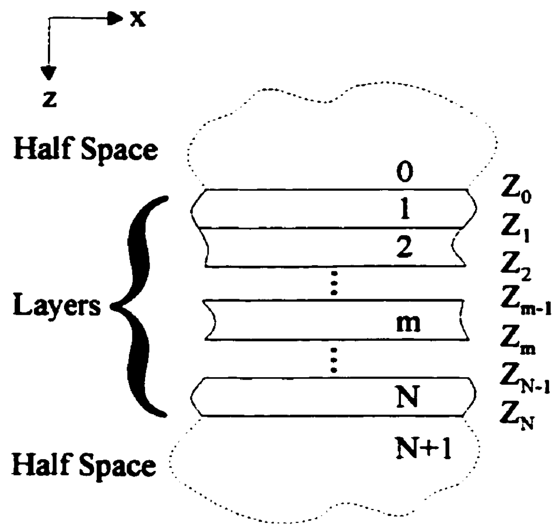

Fig. 3-11 Details of a layered medium.

3.4.1 Multi-Layer Isotropic Lamb Modes

Fig. 3-11 shows the geometry of a layered medium with traction free upper and lower surfaces. In the absence of body forces, equations (3.8) and (3.9) can be expressed in the m^{th} layer (m=1,2...N) as:

$$\phi = [A_1(k)e^{-v_P(z_m - z)} + A_2(k)e^{-v_P(z - z_{m-1})}]e^{ikx} \tag{3.13}$$

$$\psi = [B_1(k)e^{-v_S(z_m - z)} + B_2(k)e^{-v_S(z - z_{m-1})}]e^{ikx} \tag{3.14}$$

where A_1, A_2, B_1 and B_2 are constants to be determined. In order to account for the dissipative nature of materials, quality factors Q_P and Q_S are introduced such that:

$$k_P = (1+0.5i/Q_P)\omega/V_P \tag{3.15}$$

$$k_S = (1+0.5i/Q_S)\omega/V_S \tag{3.16}$$

$$\mu = \rho V_S^2/(1+5i/Q_S)^2 \tag{3.17}$$

$$\lambda + 2\mu = \rho V_P^2/(1+5i/Q_P)^2 \tag{3.18}$$

Let $\{C\} = [A_1\ A_2\ B_1\ B_2]^T$ and $\{S\} = [U_x\ U_z\ T_{xz}\ T_{zz}]^T$ such that

$$\{S(k,z)\} = [Q(k)][E(k,z)]\{C\} \tag{3.19}$$

Then $\{S\}$ in the m^{th} layer may be represented by means of the matrix product,

$$[E(k,z)] = Diag[e^{-v_P(z_m - z)} \quad e^{-v_P(z - z_{m-1})} \quad e^{-v_S(z_m - z)} \quad e^{-v_S(z - z_{m-1})}] \tag{3.20}$$

$$[Q] = [Q^- \quad Q^+] \tag{3.21}$$

where

$$[Q^-] = \begin{bmatrix} ik & -v_S \\ v_P & ik \\ 2ik\mu v_P & -\mu(2k^2 - k_S^2) \\ \mu(2k^2 - k_S^2) & 2ik\mu v_S \end{bmatrix}, \quad [Q^+] = \begin{bmatrix} ik & v_S \\ -v_P & -ik \\ -2ik\mu v_P & \mu(2k^2 - k_S^2) \\ \mu(2k^2 - k_S^2) & 2ik\mu v_S \end{bmatrix} \tag{3.22}$$

The continuity of displacements and stresses at the interfaces of the layered medium connects the unknown coefficient vectors $\{C\}$ and displacement-stress vectors $\{S(k,z)\}$ of the adjacent layers. These connections form a global linear system. Again using m to denote the layer, this continuity condition can be expressed as:

$$[Q_{m+1}(k)][E_{m+1}(k,z)]\{C_{m+1}\} - [Q_m(k)][E_m(k,z)]\{C_m\} = \{0\} \tag{3.23}$$

where z_m is the depth of the interface between the mth and $(m+1)$th layers. On the surfaces $z=0$ and $z=z_N$, the traction free conditions are applied by enforcing:

$$\begin{Bmatrix} T_{xz} \\ T_{zz} \end{Bmatrix} = \begin{Bmatrix} 0 \\ 0 \end{Bmatrix} \tag{3.24}$$

After the assembly of equations (3.23) for $m=1,2,\ldots,N$, a linear system is obtained:

$$[Q]\{C\}=\{B\} \tag{3.25}$$

The global matrix $[Q]$ is composed of submatricies obtained from $[Q_m(k)]$, $[E_m(k,z_m)]$ and $[E_{m+1}(k,z_m)]$, $m=1,2...N$. This matrix represents the physical properties of the layered medium in the k-domain. Vector $\{B\}$ is a global arrangement of the right hand side of (3.23). For the in-plane problem of an N-layered plate, the dimension of $[Q]$ is $4N$. When no external forces or dislocations are present at any interface, $\{B\}$ is a null vector and the only nontrivial solution of $\{C\}$ in (3.25) is given by

$$|Q|=0 \tag{3.26}$$

which gives all the guided wave modes.

3.4.2 Transversely Isotropic Lamb Modes

In a transversely isotropic medium, the isotropic elastic constants, λ and μ, are replaced by C_{11}, C_{33}, C_{13}, C_{44} and C_{66}. In addition, P and SV waves are no longer decoupled and are called quasi P and SV waves. As a result, matrices $[Q^-]$ and $[Q^+]$ in equation (3.22) are replaced by:

$$[Q^-]=\begin{bmatrix} -kv & k\eta \\ -(v^2-\beta^2)\alpha & (\eta^2-\beta^2)\alpha \\ -C_{44}k[v^2-(v^2-\beta^2)\alpha] & C_{44}k[\eta^2-(\eta^2-\beta^2)\alpha] \\ -v[C_{13}k^2+C_{33}(v^2-\beta^2)\alpha] & \eta[C_{13}k^2+C_{33}(\eta^2-\beta^2)\alpha] \end{bmatrix} \tag{3.27}$$

$$[Q^+]=\begin{bmatrix} -kv & k\eta \\ (v^2-\beta^2)\alpha & -(\eta^2-\beta^2)\alpha \\ C_{44}k[v^2-(v^2-\beta^2)\alpha] & -C_{44}k[\eta^2-(\eta^2-\beta^2)\alpha] \\ -v[C_{13}k^2+C_{33}(v^2-\beta^2)\alpha] & \eta[C_{13}k^2+C_{33}(\eta^2-\beta^2)\alpha] \end{bmatrix} \tag{3.28}$$

where v, η are wave numbers in the z-direction for quasi P and SV waves. Their definitions are:

$$\alpha = \frac{C_{44}}{C_{13}+C_{44}} \qquad \beta^2 = \frac{C_{11}}{C_{44}}k^2 - \frac{\omega^2\rho}{C_{44}}$$

$$\begin{Bmatrix} \eta^2 \\ \nu^2 \end{Bmatrix} = \frac{q}{4C_{44}C_{33}}[(k^2 - \frac{\omega^2\rho}{q_a}) + (k^2 - \frac{\omega^2\rho}{q_b})] \mp$$

$$\frac{1}{2}\left\{ \frac{q^2}{4C_{44}^2C_{33}^2}[(k^2 - \frac{\omega^2\rho}{q_a}) + (k^2 - \frac{\omega^2\rho}{q_b})]^2 - \frac{4C_{11}}{C_{33}}(k^2 - \frac{\omega^2\rho}{C_{11}})(k^2 - \frac{\omega^2\rho}{C_{44}}) \right\}^{\frac{1}{2}}$$

where

$$q = C_{33}C_{11} + C_{44}^2 - (C_{13}+C_{44})^2$$

$$q_a = \frac{q}{2C_{33}} \qquad q_b = \frac{q}{2C_{44}}$$

As indicated earlier, the appropriate formulations are made for each layer, with the global matrix formed by considering the continuity requirements and then solving for the Lamb wave modes.

3.4.3 Leaky Lamb Wave Model of Shot Peened Plate

In order to study the effect of shot peening upon the LLW dispersion curves, a model based upon a transversely isotropic layered medium was developed. Fig. 3-12 illustrates schematically the procedure used to model the influence of shot peening residual stresses upon the LLW modes for an isotropic plate. Assuming an initial isotropic condition, the estimate of residual stress profile obtained from finite element studies of the shot peening process is imposed on the plate. This is then discretised into a series of layers, each layer having a uniform stress level. Each layer is then assumed to be transversely isotopic, with the stress level being mapped to a variation of the ultrasonic velocity in the layer, for which the appropriate values of C_{11} through C_{66} are calculated.

Two models were studied (Fig. 3-13). The first consisted of a single compressive layer at the upper and lower surfaces of the plate with a single sub-surface tensile layer. The second consisted of three compressive layers at each surface of the plate, with varying compressive stresses and a single central tensile layer. The finite element models studied were for steel shot impacting a steel plate. The acoustoelastic effect in steel is approximately an order of magnitude lower than that for aluminium. The stress distribution for the steel plate was normalised by the yield stress, and the resulting stress field applied to a 6 mm thick aluminium plate LLW model. The effects of acoustoplasticity and surface roughness were neglected. Published acoustoelastic constants [86] were used to evaluate the velocities in each layer and the corresponding acoustoelastic constants, as listed in Table 3-3.

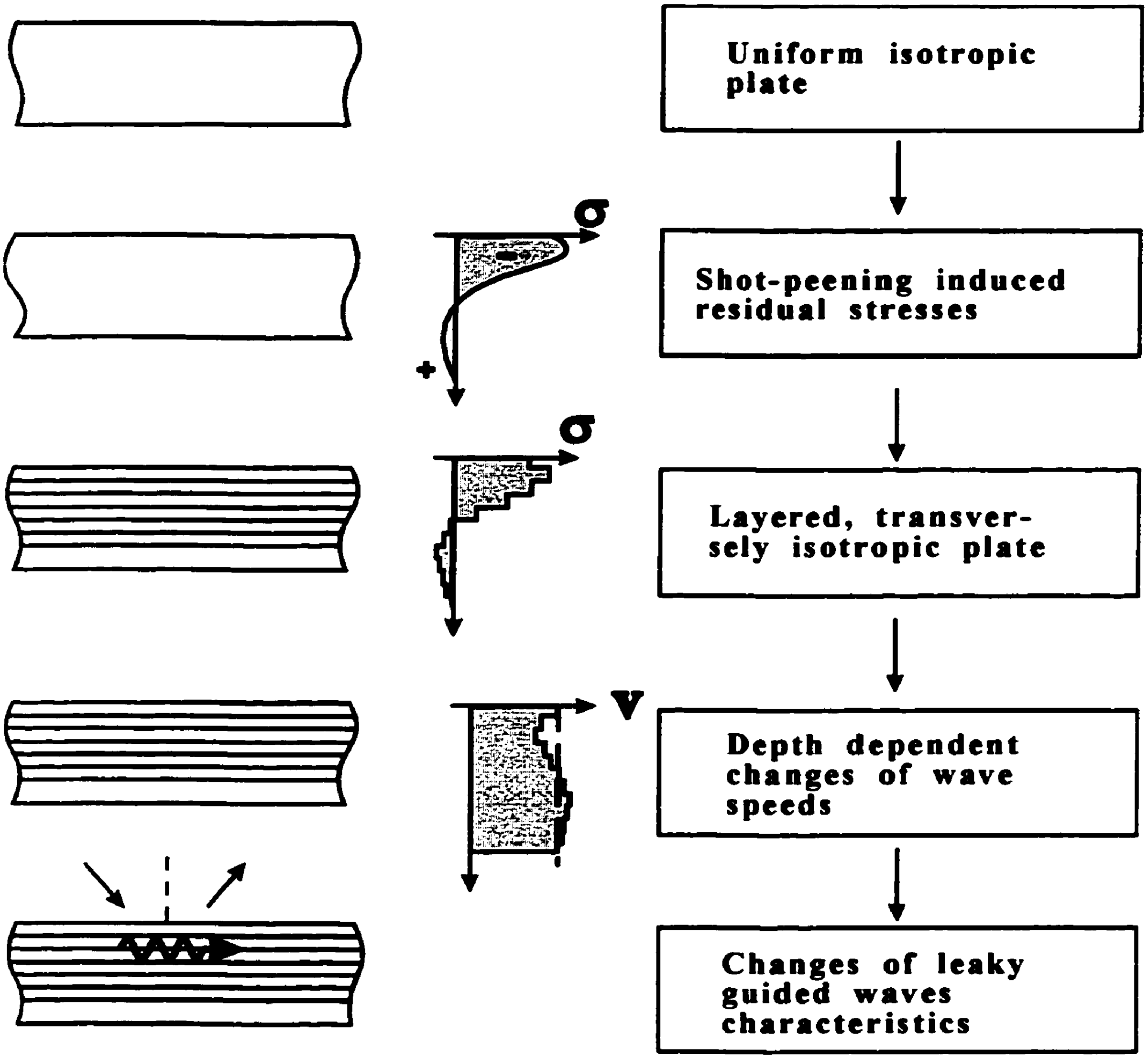

Fig. 3-12 Schematic of modelling of peening residual stresses for evaluation of LLW modes.

(a) (b)

Fig. 3-13 Models of peened specimen: (a) single compressive layer and (b) three compresive layers.

Model	Layer Thickness	Stress	C_{11}	C_{13}	C_{33}	C_{44}	C_{66}
	[mm]	$[\sigma/\sigma_0]$	$[10^9\ kg/ms^2]$				
Baseline	6.0000	0.000	107.844	54.941	107.844	26.452	26.452
Single compressive layer	0.6200	-0.997	107.394	58.489	118.288	27.344	27.008
	4.7600	+0.046	107.865	54.783	107.373	26.411	26.426
	0.6200	-0.997	107.394	58.489	118.288	27.344	27.008
Three compressive layers	0.0861	-0.936	107.422	58.264	117.630	27.289	26.973
	0.2716	-1.503	107.166	60.367	123.754	27.802	27.291
	0.2623	-0.495	107.621	56.674	112.965	26.893	26.727
	4.7600	+0.046	107.865	54.783	107.373	26.411	26.426
	0.2623	-0.495	107.621	56.674	112.965	26.893	26.727
	0.2716	-1.503	107.166	60.367	123.754	27.802	27.291
	0.0861	-0.936	107.422	58.264	117.630	27.289	26.973

Table 3-3 Material properties for modelling of LLW response based upon acoustoelastic constants reported in Krautkrämer and Krautkrämer [86].

Chapter 4 Experimental Work

Summary: This chapter is divided into two main sections. The first is concerned with the modification and application of the incremental hole drilling technique to determine shot peening residual stresses. The second is devoted to the application of a new leaky Lamb wave methodology, supported by C-scan measurements, to evaluate residual stresses in typical aerospace alloys.

4.1 Hole Drilling

This section is devoted to the incremental hole drilling technique for measuring residual stresses, and specifically with the determination of the appropriate calibration coefficients for evaluating non-uniform residual stress fields in titanium (Ti-6Al-4V); a common material for aircraft compressor disc assemblies.

4.1.1 Determination of Non-uniform Residual Stresses

The established ASTM E-837 [52] approach to measuring residual stress with the hole drilling technique considers a uniform stress along the depth of the hole increment. This is unsuitable for the large gradients expected in shot peened components. As discussed in Chapter 2, the calibration coefficients available in the literature for calculating residual stresses are not suitable to accurately describe a highly varying stress field such as that resulting from shot peening. In order to improve the technique, four areas were developed, detailed in the following sections. The first was the calculation of calibration constants for the current hole geometry, rosette configuration and depth increments of interest using the integral method. The second was concerned with the accurate determination of the zero depth level. The third was concerned with the treatment of signal noise and the fourth with the management of the data sets.

The Integral Method

In the case of an equal biaxial elastic stress field, similar to that observed in shot peening, the recorded strain relaxation is the same in all directions, and equations (2.1) and (2.2) reduce to:

$$\varepsilon = 2B\sigma = \frac{(1+\nu)}{E} b\sigma \tag{4.1}$$

where b is a constant depending only on hole dimensions and rosette geometry. In the case of a non-uniform residual stress field $\sigma(z)$ across the depth of the specimen (Fig. 4-1), the measured strain relaxation $\varepsilon(h)$, due to drilling a hole of depth h, is the integral of the infinitesimal strain relaxations resulting from stresses at all depths $0 \leq z \leq h$, viz:

$$\varepsilon(h,z) = 2B\sigma = \frac{(1+\nu)}{E}\int_0^h b(z,h)\sigma(z)dz \qquad 0 \leq z \leq h \tag{4.2}$$

where $b(z,h)$ is the strain relaxation per unit depth caused by a unit stress at depth z. The dependency of $b(z,h)$ on the depth z represents the unequal contribution to the relaxed surface strain from stresses at different depths z. On the other hand, the variation of b with the hole increment h represents the strain variation associated with the change in the compliance due to the change in the hole size. If the function $b(z,h)$ is known and the strain relaxation $\varepsilon(h)$ is measured continuously, the residual stress field $\sigma(z)$ can be obtained by solving the above integral equation.

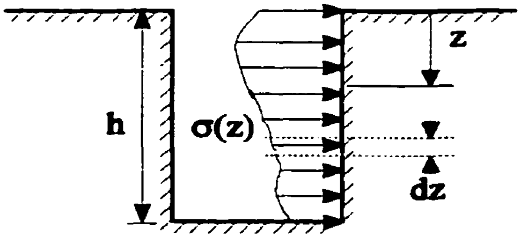

Fig. 4-1 Non-uniform residual stress distribution with hole depth.

In practice, however, the strain relaxation is measured for a limited number of hole increments. For this reason, equation (4.2) is rewritten in a discrete form for the i^{th} hole depth as

$$\sum_{j=0}^{j=i} b_{ij}\sigma_j = \frac{E}{(1+\nu)}\varepsilon_i \tag{4.3}$$

where σ_j is the equivalent uniform stress for increment j within the hole depth i, as illustrated in Fig. 4-2. Equation (4.3) can be written in a matrix form as:

$$\begin{bmatrix} b_{11} & & & \\ b_{12} & b_{22} & & \\ \vdots & \vdots & \ddots & \\ b_{1n} & b_{2n} & \cdots & b_{nn} \end{bmatrix} \begin{bmatrix} \sigma_1 \\ \sigma_2 \\ \vdots \\ \sigma_n \end{bmatrix} = \frac{E}{(1+\nu)} \begin{bmatrix} \varepsilon_1 \\ \varepsilon_2 \\ \vdots \\ \varepsilon_n \end{bmatrix} \tag{4.4}$$

where n is the number of increments. If the calibration coefficients b_{ij} are known and ε_i is measured for selected hole depths, the residual stresses σ_i are then obtained by inverting the lower triangular matrix b_{ij}. In this case, the actual residual stress distribution is obtained as a stepwise approximation.

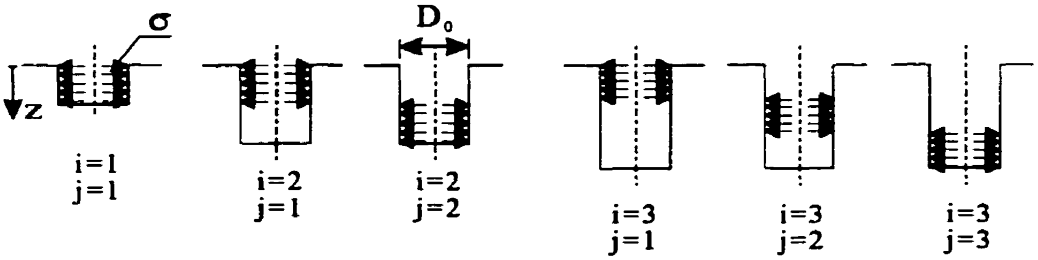

Fig. 4-2 Load configuration for different hole increments.

Evaluation of Coefficients

For a specific hole diameter and strain gauge location, the coefficients b_{ij} represent the recorded strain relaxation caused by a unit equal biaxial stress field located at the j^{th} increment (Δh_j) in the i^{th} hole depth (h_i). Therefore, b_{ij} can be evaluated using axisymmetric linear-elastic finite element calibration for specific strain gauge rosette geometry and selected hole increments.

The calibration coefficients were calculated using the ANSYS finite element code [88] for the mesh geometry shown in Fig. 4-3. The high mesh density mesh was se;lected in the milling region following a large number of convergence tests pertaining to the coefficients. The mesh selected corresponded to three elements per milling increment. The diameter of the hole (1.82 mm), the length of the strain gauge (1.59 mm) and its location from the axis of symmetry (2.57 mm) correspond to the configuration of the strain gauge rosette TEA-13-062RK-120. The simulated specimen radius R and depth H were selected so that boundary effects were eliminated [52].

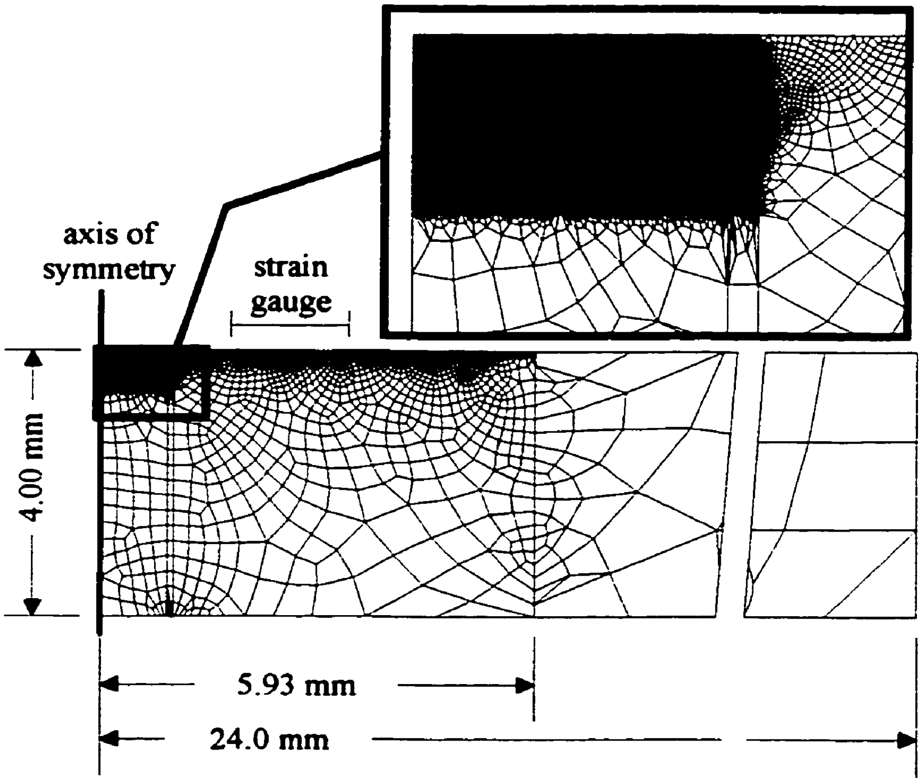

Fig. 4-3 Sample finite element mesh for hole drilling calibration.

A four-noded isoparametric element was used in the analysis and convergence checks were performed to optimise the finite element mesh to that of Fig. 4-3. To account for the high gradient in shot peening residual stresses close to the surface, it was necessary to compute the calibration constants using very small increments. The calibration coefficients were calculated for increments of 12.7 μm (0.0005 in), 25.40 μm (0.001 in), 63.5 μm (0.0025 in) and 127 μm (0.005 in) with 4, 20, 14 and 10 increments respectively. The values of the coefficients are tabulated in Appendix A.

Zero Level Determination

As the increment of the depth resolved decreases, the error becomes predominantly controlled by the initial zero level determination. The established technique evaluates the zero level by observing a 3 με change in the microstrain reading. This technique could not be applied as it would obscure the initial stress level of interest. The technique adopted was therefore to approach the gauge in steps finer than the desired inversion increment. After each approach the end mill was backed off and the gauge inspected under 4x magnification. Zero level was determined when a complete circle of bare metal was observable in the centre of the gauge. This level was confirmed audibly by observing the sound of the system as the end mill approached. A ring was heard upon the end mill first contacting metal. After the test was completed, this procedure was carried out on either side of the initial hole to ensure that the system remained in calibration. This provided determination of the zero level within 6.35 μm.

Filtering

Two sources of variability in the signal are from variations in temperature and errors in the depth of the drilled hole. Global fluctuations in temperature were montiored by an independent strain gauge bridge on a coupon adjacent to the tested work piece. A MicroMeasurements Group System 5000 multichannel strain gauge reader was used to monitor the temperature induced microstrain as well as the relieved microstrains. These were monitored in real time and logged at 2 s intervals. In order to minimize the temperature rise due to machining, small machining increments (6.35 μm) were carried out at low feed rates (4×10^{-4} m/min). Once the machining increment was completed, the end mill was withdrawn and the gauge readings allowed to stabilise.

Errors in the measured depth of the hole were addressed by milling in increments smaller than those required for the inversion procedure. The results were then mathematically filtered to obtain smooth curves. The inversion was then carried out on the smoothed data.

Data Management

A custom program, implemented in MatLab, was developed to automate the calculation of residual stresses. This interactive program incorporated the ability to filter the data through the evaluation of local means, curve fitting, and strain channel averaging as well as adjust for zero level offsets and perform error bound estimation, with graphical and numerical output.

4.1.2 Verification of Incremental Hole Drilling Method

The accuracy of the calibration coefficients and measurement techniques were checked by measuring bending stresses in a cantilever beam with a known stress field. The bar was made of aluminium 6061-T6 with cross sectional dimensions of 76 mm×8.1 mm and length 300 mm. The given elastic modulus and Poisson's ratio were E=70 GPa and ν=0.331, respectively. A strain gauge rosette (TEA-13-062RK-120) was mounted on the centreline of the upper surface, 180 mm from the applied load. A T rosette (CEA-13-062WT-120) was mounted on the centreline, 60 mm closer to the load application point. The beam was loaded incrementally to 135 N. To eliminate the effect of residual stresses that may exist in the beam, the load was removed during each drilling operation. The corresponding strains were recorded before and after drilling each hole increment as well as before and after each load application. The final hole depth was 1.2 mm. The strain relaxation due to the introduction of the hole increments was obtained from the difference of the strains after and before drilling.

Although the calibration matrices, b_{ij}, were evaluated for an equal biaxial stress field, they could be used in the current example by using a modified equation that relates b_{ij} to the uniaxial bending stress. For a general biaxial stress state, the principal stresses were obtained as:

$$\sigma_{I} = \frac{\varepsilon_1 + \varepsilon_3}{4B} - \frac{\sqrt{2}}{4C}\sqrt{(\varepsilon_1 - \varepsilon_2)^2 + (\varepsilon_2 - \varepsilon_3)^2} \tag{4.5}$$

$$\sigma_{II} = \frac{\varepsilon_1 + \varepsilon_3}{4B} + \frac{\sqrt{2}}{4C}\sqrt{(\varepsilon_1 - \varepsilon_2)^2 + (\varepsilon_2 - \varepsilon_3)^2} \tag{4.6}$$

Combining the above two equations with equation (4.3), we obtain

$$\sum_{j=0}^{j=i} b_{ij}(\sigma_{I} + \sigma_{II})_j = \frac{E}{(1+\nu)}(\varepsilon_1 + \varepsilon_3)_i \tag{4.7}$$

Making use of the first stress invariant ($\sigma_{I} + \sigma_{II}$) and the first measured strain invariant ($\varepsilon_1 + \varepsilon_3$), the calibration matrix b_{ij} in the above equation can be calculated using the above axisymmetric finite element model. It follows that the in-depth distribution of the stress invariant ($\sigma_1 + \sigma_2$) can be calculated using the calibration matrices obtained in the previous section. In a uniaxial stress field, the applied stress is obtained directly using equation (4.7).

A least squares fit was obtained for each inverted data set to minimize the influence of errors. From this, the calculated surface stress for inversion increments of 25.40 μm, 63.5 μm and 127 μm was found to be within 10% to 15% of the theoretical stress obtained using beam theory and finite element modelling. For the finest increment (127 μm) much larger errors in stress measurements were observed. For example, errors in the range of 90 to 175 MPa were obtained. These correspond to a very small error in strain measurement (1-2 με). Accordingly, care must be taken when employing the incremental hole drilling method for very fine increments.

4.2 Instrumented Cold Hole Expansion

In order to evaluate the accuracy of the finite element method in modelling the cold expansion process, an instrumented plate was subjected to sequential cold expansion. An aluminium 7075-T651 plate (150×45×3.14 mm) with two 4.95 mm diameter holes along the centreline was prepared. The centre-to-centre separation of the holes was 7.5 mm. Two EA-13-031MF-120 strain gauges were mounted along the centreline of the plate and a CEA-13-062WT-120 T rosette was mounted between the two holes, offset to one side (Fig. 4-4 (a)). The plate was clamped in a fixture to maintain alignment and provide guides for the mandrels (Fig. 4-5), with spacers to protect the gauges and connection wires. The holes were then sequentially expanded, with the hole near the two gauges G1 and G2 being expanded first, and the strains being recorded at 1 Hz with a MicroMeasurements System 5000 data acquisition system. The recorded strain approached the extension limits of the gauges during the expansion operation. Subsequent

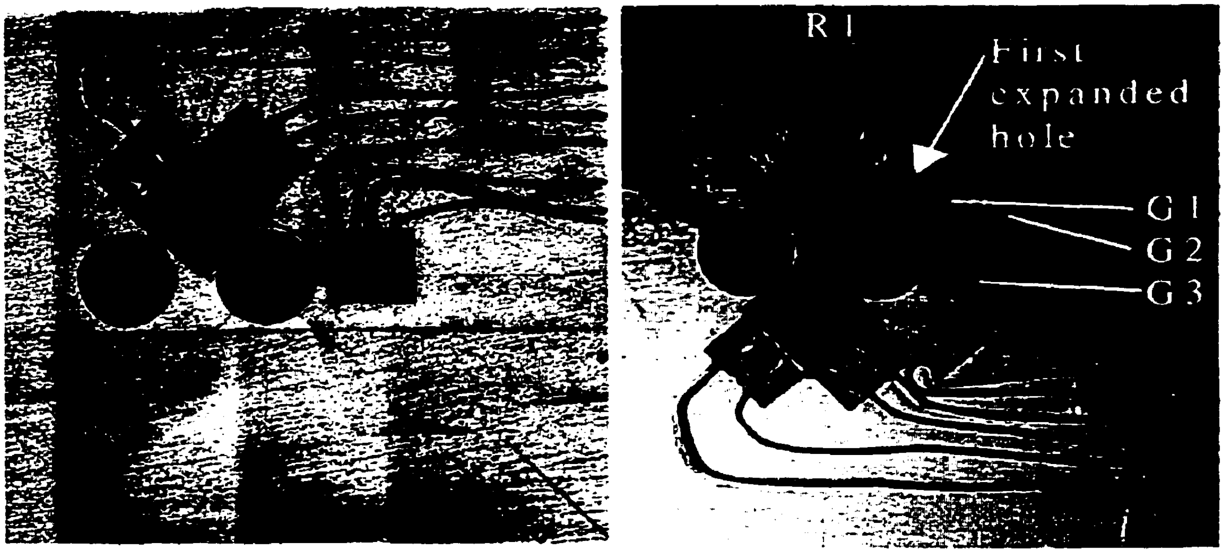

(a) (b)

Fig. 4-4 Instrumented plate: (a) before and (b) after cold expansion.

to the expansion process, an additional EA-13-031MF-120 gauge was bonded at a 45° angle to the centreline of the plate, in line with the centre of the first hole. Additionally, a second CEA-13-062WT-120 T rosette was bonded between the holes (Fig. 4-4 (b)). The strains were recorded from all gauges during subsequent elastic bending. This permitted the verification that the original strain gauges were not damaged when subjected to the large inhomogeneous strains experienced during the expansion process.

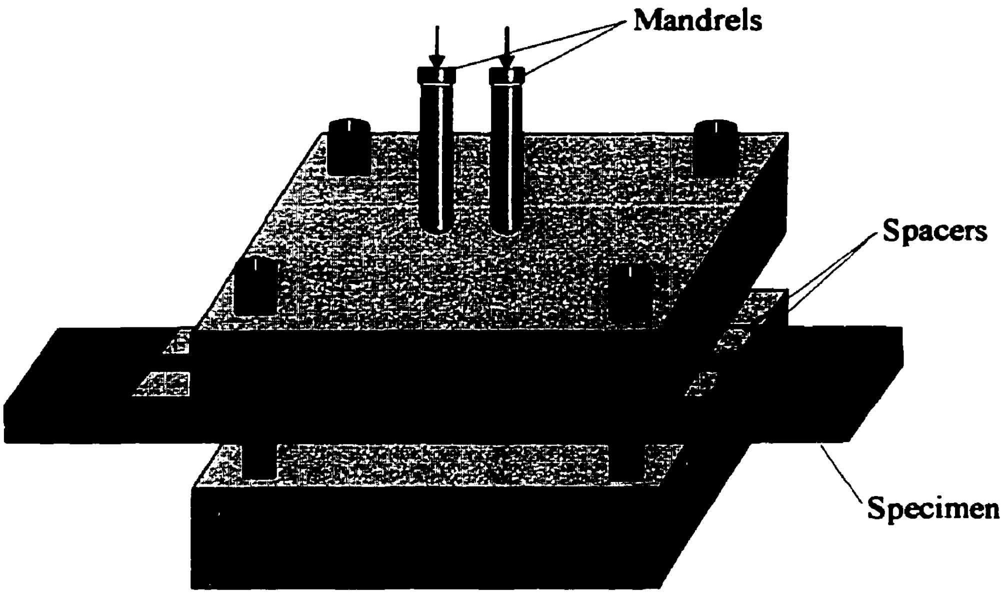

Fig. 4-5 Schematic of fixture for cold hole expansion.

4.3 LLW Measurement of Residual Stresses

4.3.1 Experimental Setup

Leaky Lamb Wave Apparatus

Fig. 4-6 illustrates the general setup of the ultrasonic delivery system for LLW measurement of stress. The test sample is immersed in a water tank. With two transducers positioned in a pitch-catch arrangement with the aid of a guiding arc, the ultrasonic analyser (KFJ HIS-1; frequency response 1.5-100 MHz) provides a pulse to the transmitter transducer through a preamplifier (KFJ HIS-1901). The pulse excites the transducer, which obliquely emits ultrasonic waves into the test sample through the water. The reflected signals are then picked up by the receiver transducer, which passes them to the ultrasonic analyser through another preamplifier. The receiver signal is conditioned, amplified, and transferred to the digital oscilloscopes (Phillips PM 3365A, 100 MHz, 100 MS/s and/or Philips PM 3380A, 100 MHz, 10 GS/s) for viewing. To facilitate determination of the locations of the specimen, measurement of surface features and allow the capability of traditional A, B and C scans, a third transducer is mounted at the apex of the arc along the centreline. The XYZ positioning of the guiding arc is controlled by stepper motors with an accuracy of 2.5 μm. The synchronous angular positioning of the probes on the guiding arc is also controlled by a stepper motor with an accuracy of 0.050°.

Data Acquisition and Processing

The data acquisition system developed employed a PC to control the linear motion of the guiding arc and the angular positioning of the probes. In an LLW scan, a number of test locations and incident angles were involved. At each selected test location and incident angle, the height of the guiding arc with respect to the surface of the specimen was adjusted to obtain equal amplitude pulses from the upper and lower surfaces of the specimen [73]. Noise beyond these two pulses was filtered by digital gating. Signals were acquired until criteria for repeatability are met, and then the signal with the most deeply developed minima was stored. These criteria included the depth of the minima with respect to the overall signal, the repeatability of several acquisitions at the same point and the consistency of the ratios of the echo from the upper and lower surfaces of the specimen. The Fast Fourier Transform (FFT) technique, with 32 padding, was then used to obtain the amplitude spectrum from the time signal. As a result, using the PM 3365A, the time resolution of the signal is 5 ns and the frequency resolution of the amplitude spectrum is 6.10 kHz. The PM 3380A acquires up to 32×1024 data points, with a 200×10^6 samples/s in single shot mode, and up to 1×10^9 samples/s through the use of random interleave sampling on repetitive signals. The latter results in a lower signal to noise ratio.

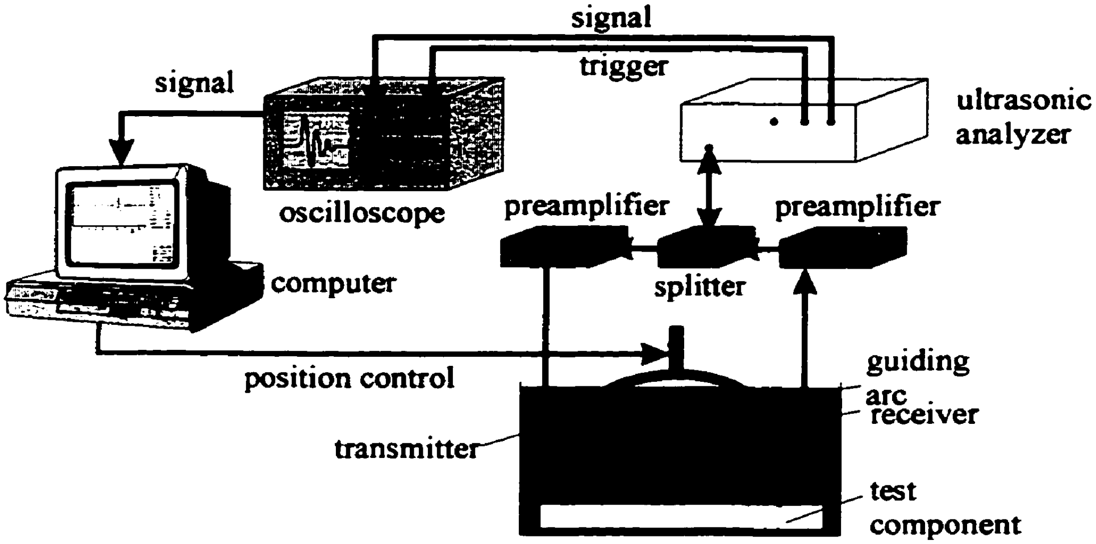

Fig. 4-6 Schematic of leaky Lamb wave test facility.

4.3.2 Leaky Lamb Wave Measurement of Applied Direct Stress

The test sample was a modified version of the standard ASTM tensile specimen (Fig. 4-7) [89]. The test sample (aluminium 7075-T651) was placed in a loading frame, which was immersed in a water tank. The loading frame used a hydraulic cylinder with a double-acting pump to apply axial force on the test sample, as shown in Fig. 4-8. The calibration of the pump pressure versus applied force was obtained through the use of strain gauged test samples. A check valve placed in line between the cylinder and the pump was used to maintain a constant pressure for the duration of the test cycle. This was monitored periodically through a dial pressure gauge. This system was evaluated in a servo-hydraulic load frame assembly to verify the capability to maintain a given pressure with a variation of 3% for a period of 24 hours.

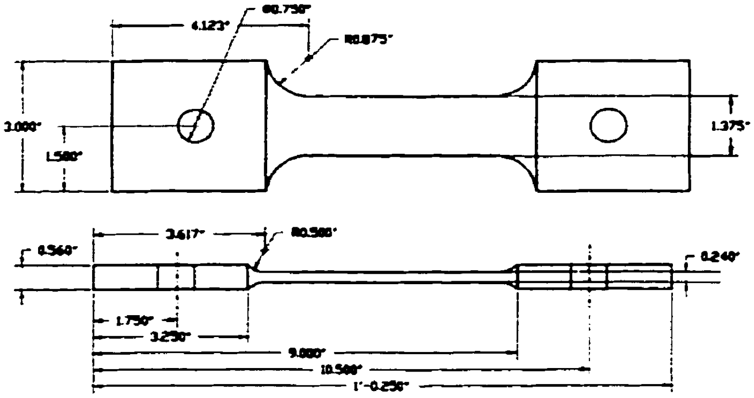

Fig. 4-7 Details of specimens used for calibration.

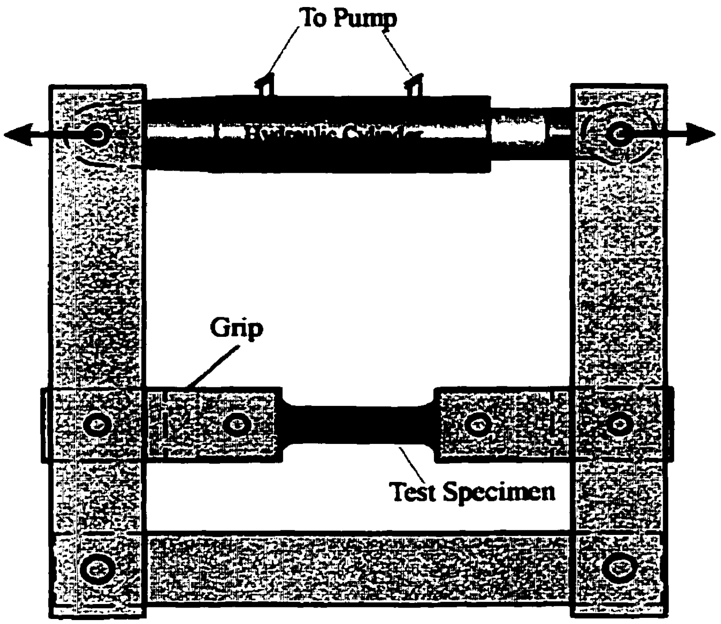

Fig. 4-8 Loading of specimen for applied stress measurements.

4.3.3 Cold Hole Expansion

The LLW technique was applied to evaluate the variation of the Lamb wave velocity around the expanded holes. An aluminium 7075-T651 plate (150×45×3.14 mm, Fig. 4-9) with two 4.98 mm diameter holes located along the centreline, with a centre to centre separation distance of 7.5 mm was scanned. Measurements were carried out before and after a 2% expansion. The scans were carried out with the polarisation of the Lamb waves both parallel and transverse to the centreline of the plate. The transducers selected were 0.5", 3" focused, 5 MHz broadband for both the transmitter and receiver. Incident angles of 16° and 22° were investigated.

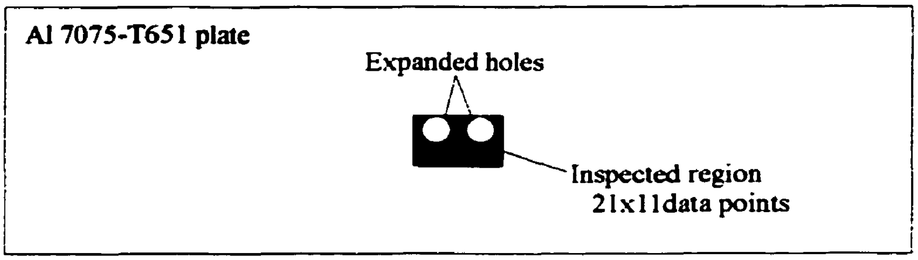

Fig. 4-9 Details of leaky Lamb wave scanned cold expanded plate.

4.3.4 Shot Peening

Plates of aluminium 6061-T6 with dimensions of 96.8×38.1×6.35 mm were subjected to shot peening treatment on the upper surface. Half of the specimen was masked off to preserve the original condition (Fig. 4-10). A grid of 150×3 points across the specimen was scanned for each specimen at angles of 16°, 18° and 20° with the Lamb wave polarisation being parallel to the 96.8 mm dimension. Angular corrections were carried out to account for the curvature induced by the peening process. In analysing the data, points near the interface between the peened and unpeened sections were ignored, as they would incorporate aspects of both. The remaining points in each section were averaged in order to obtain an aggregate and reduce the variations due to random errors resulting from electrical noise and microstructural variations.

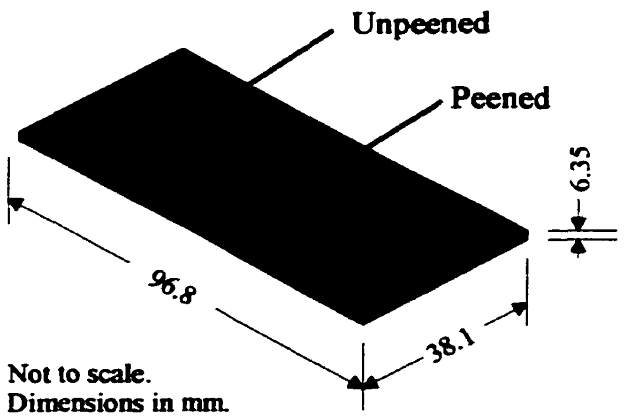

Not to scale.
Dimensions in mm.

Fig. 4-10 Detailed geometry of shot peened specimens.

4.4 Ultrasonic C-Scan

The equipment used to carry out the ultrasonic C-scan of the specimen with the cold expanded holes was the same as that used to carry out the LLW measurements. The normal incidence mount at the centreline of the guiding arc was used with a KFJ-MPC 35 MHz, 5 inch focus transducer. Using the same specimen as detailed in 4.3.3, two grids (illustrated in Fig. 4-11) were measured. The time domain signals were recorded from both the PM 3365A and the PM 3380B simultaneously and then analysed using Matlab 5. The time of flight data from both the PM 3365A and the PM 3380B were evaluated and averaged over 3 and 4 reflections, respectively. Furthermore, autocorrelation of the PM 3380B data was carried out to obtain an estimate of the time of flight. This reduced the sensitivity to the noise inherent in the random interleave sampled data.

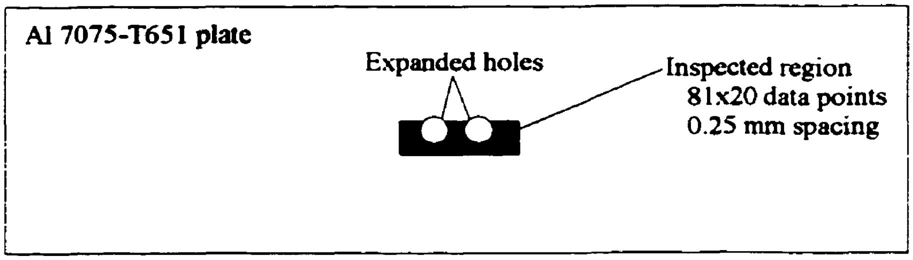

Fig. 4-11 Details of C-scanned cold expanded plate.

Chapter 5 Results and Discussion

Summary: In this chapter three issues are addressed. First, the developed finite element models are validated. The models are then used to investigate the processing parameters of the cold hole expansion and shot peening processes upon the residual stress distribution in the treated components. Secondly, destructive experimental techniques are used to investigate the mechanically induced residual stresses. A series of incremental hole drilling measurements used to investigate several of the parameters investigated in the FE study are detailed. Finally, ultrasonic measurements are applied to the investigation in two ways. In one way, LLW and C-scan measurements were carried out on treated components. In the other, the effects of shot peening residual stresses upon the LLW dispersion curve are evaluated and studied.

5.1 Cold Expansion of Interacting Fastener Holes

5.1.1 Two Dimensional Analysis

The material properties used were that of aluminium alloy 7075-T651 with $E = 72$ GPa and $\nu = 0.32$. The elasto-plastic behaviour was assumed to be bilinear with isotropic hardening and an initial yield stress of 506 MPa. Fig. 5-1(a-c) show the variation of the normalised equivalent stress trajectories for three different expansion levels (2%, 4% and 6%), while Fig. 5-1(d) shows the unloading residual stress field corresponding to the 6% expansion level. The figures show clearly the growth of the plastic zone with the increase of the expansion. They also show interaction effects in the region contained between the two fastener holes. Fig. 5-2(a) and Fig. 5-2(b) show the variation of the normalised tangential residual stress versus the distance along the lengths variation of the normalised tangential residual stress versus the distance along the lengths AB and CD, measured from the central line of the workpiece, respectively. Fig. 5-2(a) reveals the presence of tensile residual stresses at the central distance between the holes for an expansion level of 2%. Increasing the expansion level results in a reduction in the tensile field, leading to a purely compressive residual stress field at an expansion level of 6%. This is compensated for by the increase in the tensile residual stress along the length CD of Fig. 5-2. Fig. 5-2(b) also reveals that maximum compressive residual stresses occur at the hole boundary.

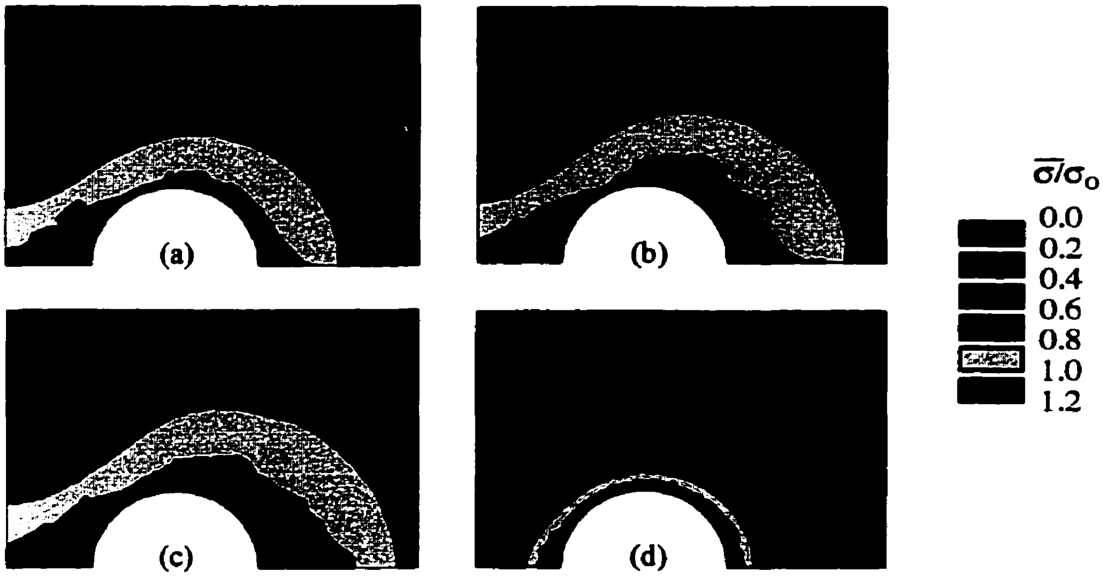

Fig. 5-1 Details of equivalent stress $\bar{\sigma}$ contours for different expansion levels: (a) 2%, (b) 4%, (c) 6%, and (d) unloading from 6% expansion.

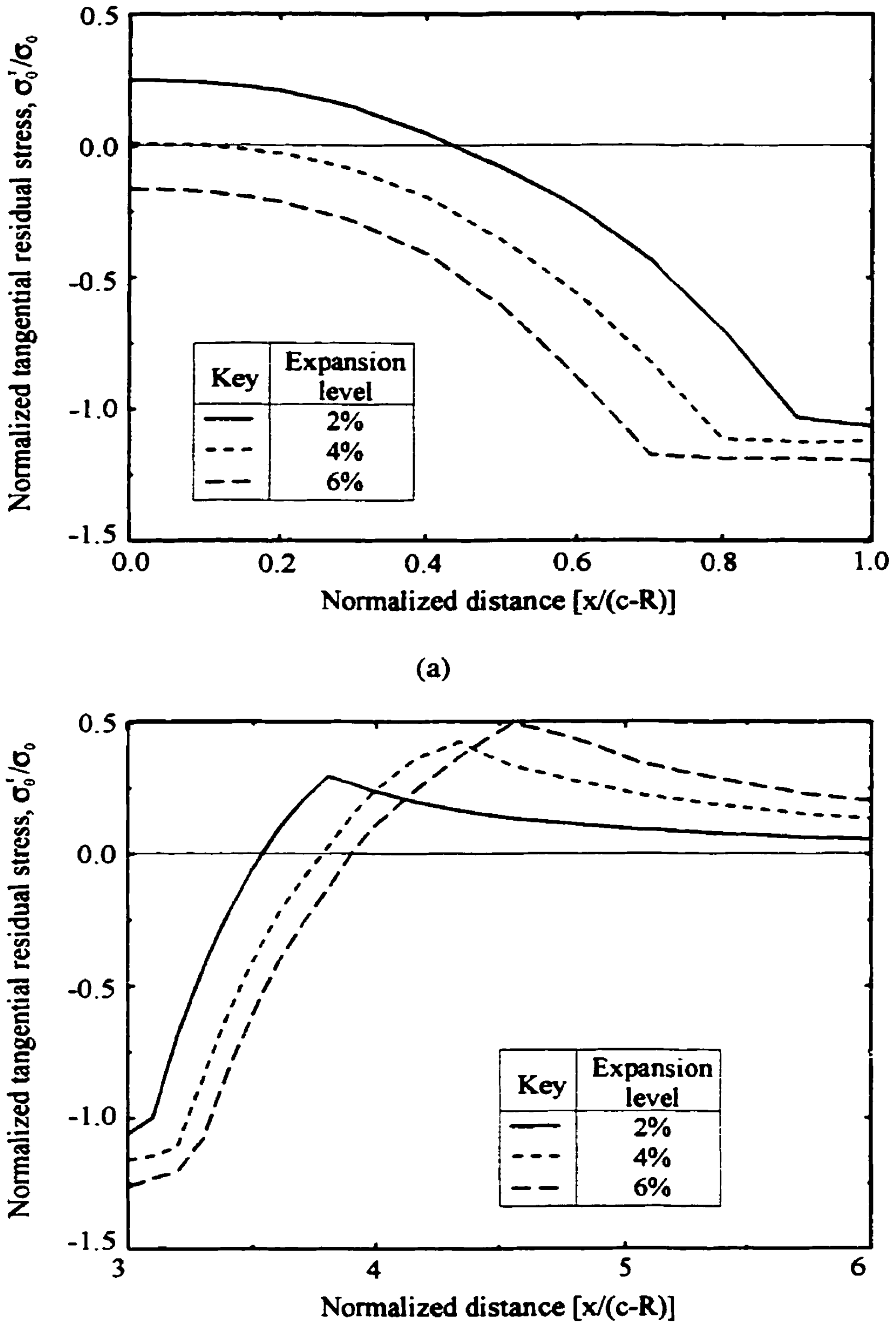

Fig. 5-2 Variation of normalised tangential residual stress σ_θ^r/σ_0 along lengths (a) AB, and (b) CD for 2c = 4R and H/E = 1%.

Fig. 5-3 shows the normalised tangential residual stress versus the distance along the length AB for an expansion of 6%. The figure reveals the relatively high tensile residual stresses for the case where 2c = 6R. No tensile residual stresses were observed for 2c = 4R. Fig. 5-4 shows the insignificant effect of the strain hardening rate upon the residual stress field along length AB. In all the above trials, the two fastener holes were expanded simultaneously.

We now turn our attention to the case where the expansion was conducted ***sequentially***. Using the mesh from Fig. 3-2 an alternate expansion of 4% was applied to each of the holes. Fig. 5-5 shows the residual stress results for a single hole expansion; sequential expansion; and simultaneous expansion of the two fastener holes. The figure reveals the dramatic difference resulting from the ***order*** of the expansion. It indicates that large tensile residual stresses are developed in the case where the mandrel is applied sequentially to the holes.

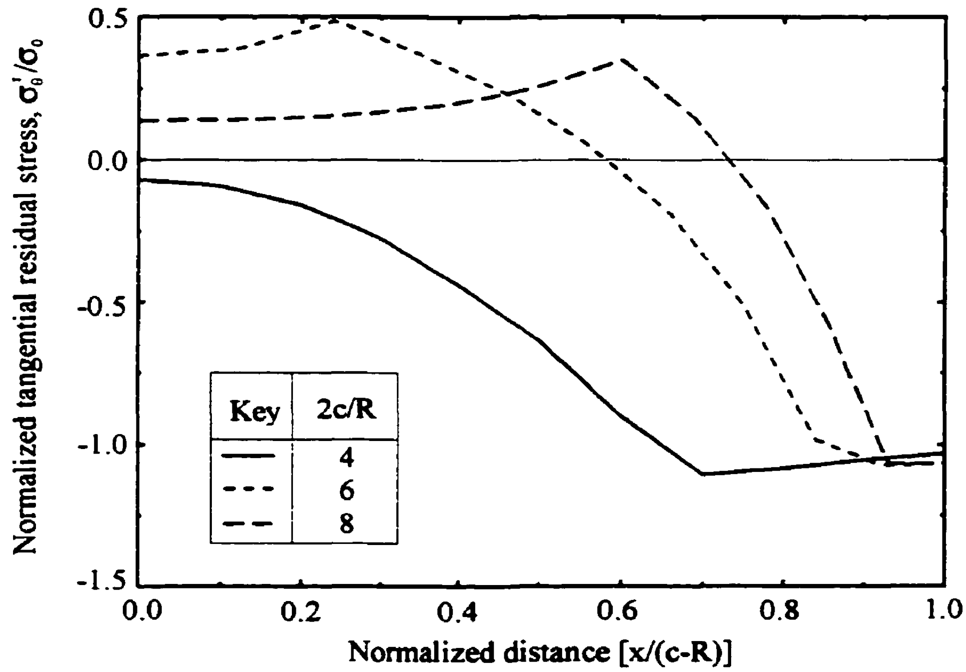

Fig. 5-3 Variation of normalised tangential residual stress σ_θ^r/σ_0 along length AB for a 6% expansion and H'/E = 0.1%.

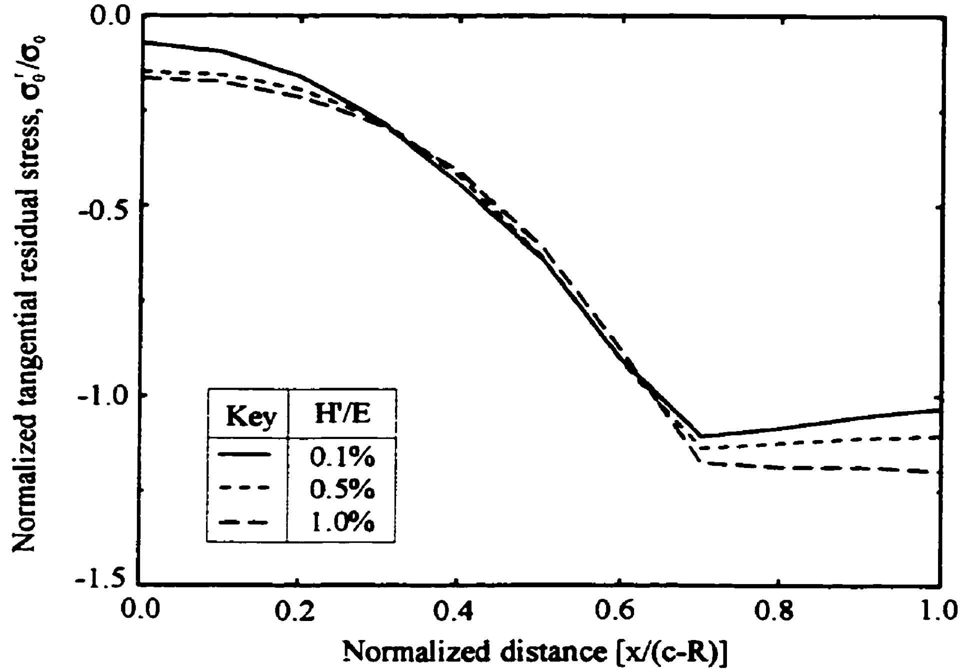

Fig. 5-4 Variation of normalised tangential residual stress σ_θ^r/σ_O along length AB for a 6% expansion with 2c = 4R.

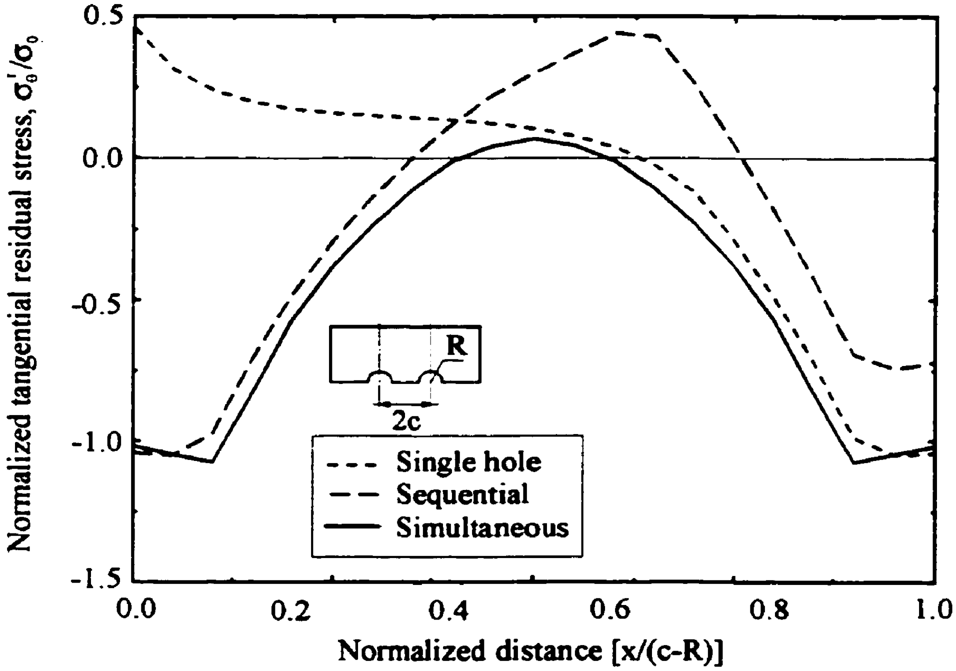

Fig. 5-5 Variation of normalised tangential residual stress σ_θ^r/σ_O for sequential expansion with 2c = 4R, 4% expansion and H'/E=0.1%.

Limitations of the Two Dimensional Model

The two dimensional model described above suffered from the following shortcomings. First, it ignores the asymmetric nature of the current cold expansion process. Second, it did not account for contact conditions at the interface between the mandrel and the hole. It assumed a rigid mandrel, as evidenced by the imposition of the displacement at the boundary of the workpiece. Finally, it was incapable of accounting for friction as well as surface roughness variations through the thickness of the plate during the cold expansion process. These shortcomings will manifest themselves in the deformed geometry, development and growth of plastic zone and unloading residual stresses. This has motivated the three dimensional finite element modelling described below.

5.1.2 Three Dimensional Analysis: Validation

The three dimensional finite element model was validated by comparing with the experimental measurements conducted by Link and Sanford [30]. Link and Sanford obtained the residual strain field surrounding a single split-sleeve cold expanded hole in 6.35 mm thick 7075-T651 aluminium plates using moiré interferometry. Numerous finite element runs were conducted to examine the effect of the centre distance upon the field variables. The work concluded that virtually no interaction effects are present for the case where $2c/R \geq 10$. Accordingly, the geometry shown in Fig. 3-3(a) with $R = 2.87$ mm, $2c = 28.7$ mm and t=6.35 mm was discretised for comparison with the existing results of Link and Sanford for a 3% expansion. Fig. 5-6 shows the residual radial and tangential strains at the entry face of the specimen. Good agreement between the experimentally obtained distribution and the current finite element predictions was observed.

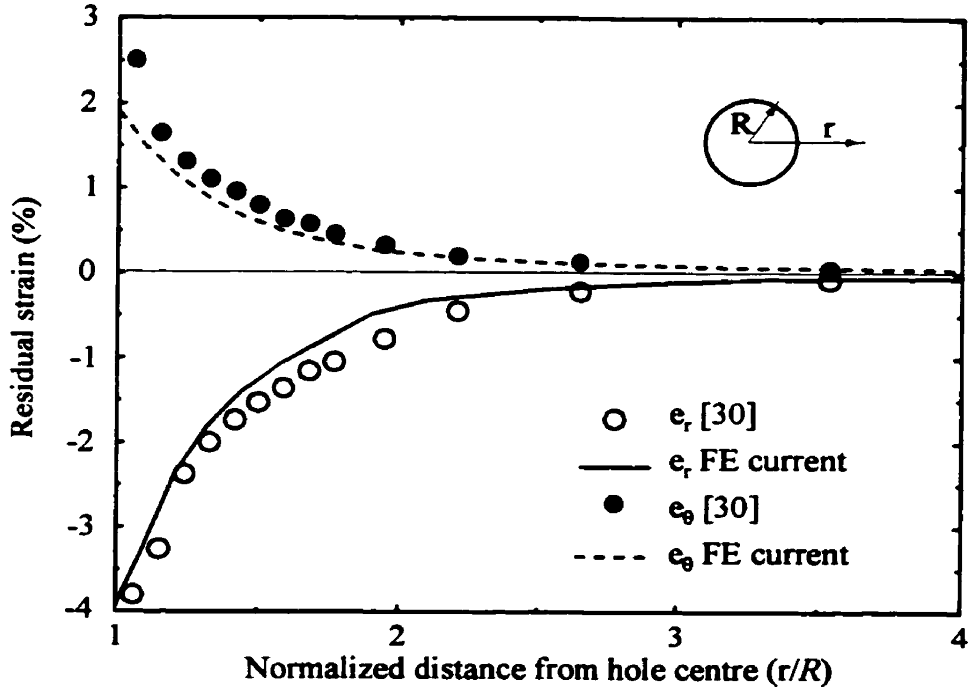

Fig. 5-6 Comparison between FE predictions and interferometry residual strain distribution results, after Link and Sanford [30]

5.1.3 Three Dimensional Analysis: Simultaneous Expansion

To investigate the effect of the geometry, the centre distance between the two holes was varied from 3R to 10R. The outer boundary of the plate, which was rigidly fixed, was selected such that it did not affect the results in the regions surrounding the expanded holes. The total mandrel displacement (16mm) was applied incrementally in 20 steps.

The von Mises stress contours for a centre distance of 4R at four different mandrel positions is shown in Fig. 5-7. Both the entry and the exit views are provided. At the initial entry stage (Fig. 5-7(a)), the mandrel is in contact with a small fraction of the fastener hole. In this case, the equivalent stress trajectories at the entry surface reveal the limited contact between the mandrel and the plate. When the mandrel is pushed further into the plate (Fig. 5-7(b)), both surfaces experience comparable levels of stresses. However, with the additional travel of the mandrel into the hole (Fig. 5-7(c)), the equivalent stress field at exit surface is dramatically increased. Fig. 5-7(d) shows the exit stage of the mandrel. The figure reveals the remarkable difference between the equivalent stress at exit and entry surfaces. This shows clearly the inability of two dimensional modelling to accurately capture the plastic zone development and unloading residual stresses resulting from the cold expansion of two adjacent holes.

The variation of the normalised equivalent stress $\bar{\sigma} / \sigma_0$ across the thickness of the plate at point B is shown in Fig. 5-8 for four different mandrel positions. The figure clearly indicates that during the entry stage (10% and 25% strokes) the equivalent stress is much higher at the entry than at the exit surfaces. At 60% stroke, the equivalent stress distribution is uniform across the thickness. The residual equivalent stress field (mandrel stroke 100%) attains a maximum value at mid-thickness and a minimum value at the entry face.

The effect of the centre distance between the two expanded holes upon the resulting residual stress field is shown in Fig. 5-9 for a 2% expansion. The normalised tangential residual stress at point B is plotted across the thickness of the specimen for the three different centre distances where the interaction effects were dominant. The results show that the centre distance of the two cold expanded holes can lead to a significant change in the residual stress field. The figure also shows that a decrease in the centre distance between the expanded holes results in a decrease in the compressive residual stresses at the entry face and an increase at the exit face of the workpiece. These very low compressive residual stresses have an insignificant effect on the fatigue performance of the cold worked piece. Fig. 5-10 shows the variation of the tangential residual stress contours around the cold worked hole for some of the centre distances examined. The figure reveals the large variation in tangential residual stress in the region of influence.

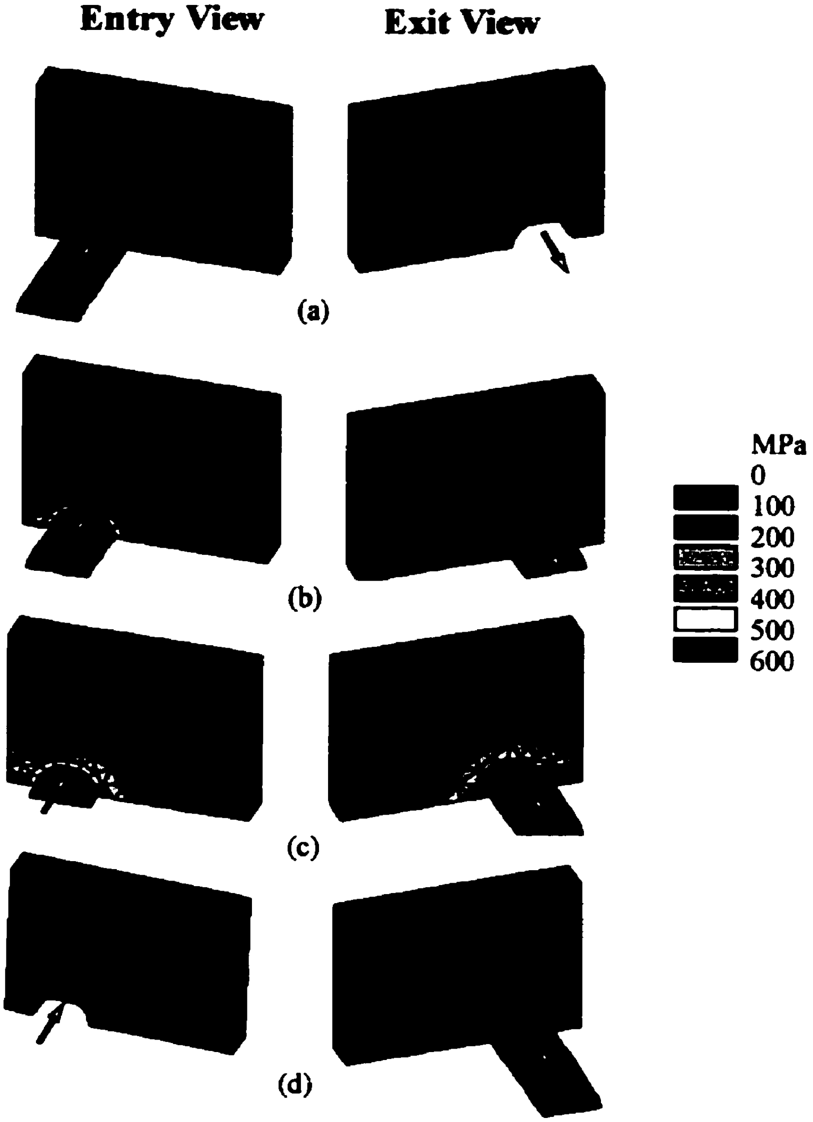

Fig. 5-7 Details of equivalent stress $\bar{\sigma}$ contours at entry and exit for different mandrel strokes: (a) 10%, (b) 25%, (c) 60% and (d) 100%.

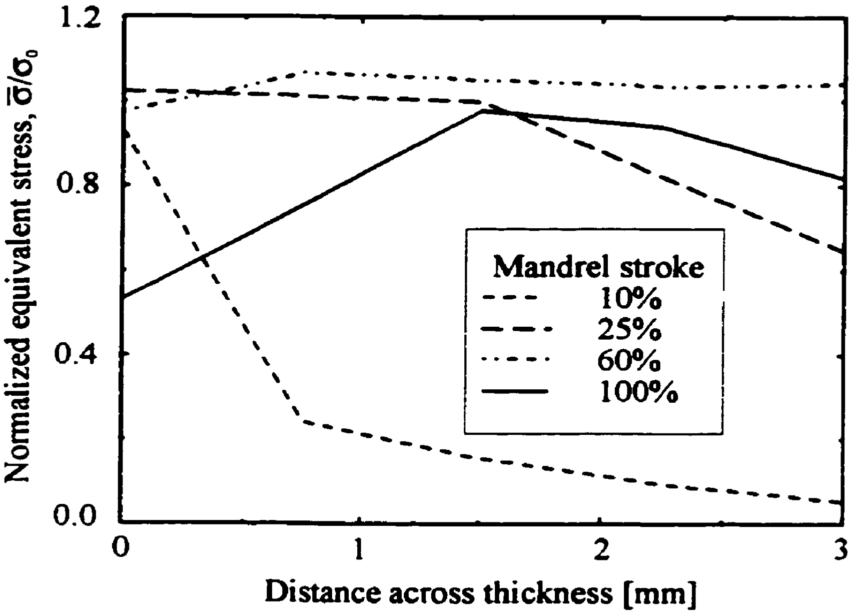

Fig. 5-8 Variation of normalised equivalent residual stress $\bar{\sigma} / \sigma_0$ through thickness at point B.

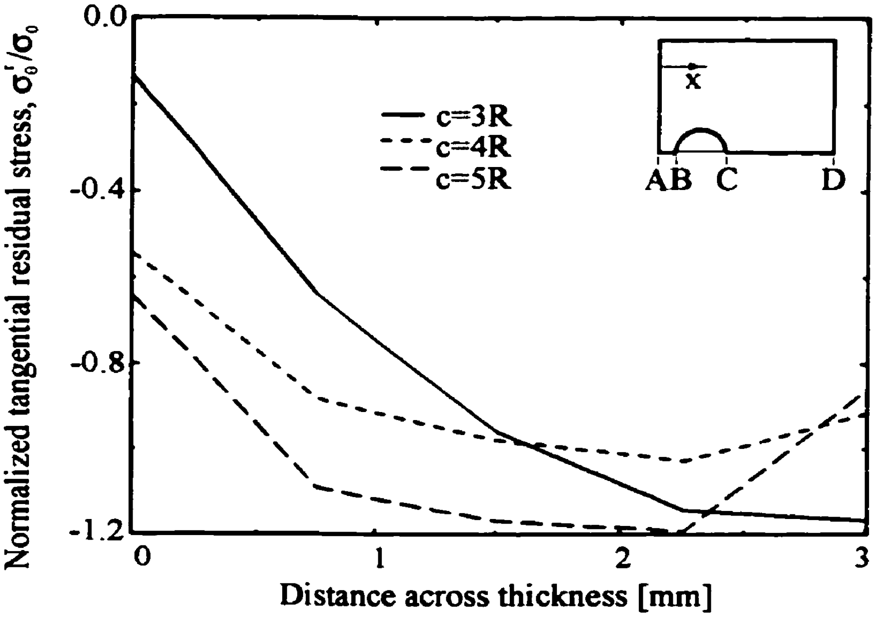

Fig. 5-9 Variation of normalised tangential residual stress σ^r_θ/σ_0 through thickness at point B.

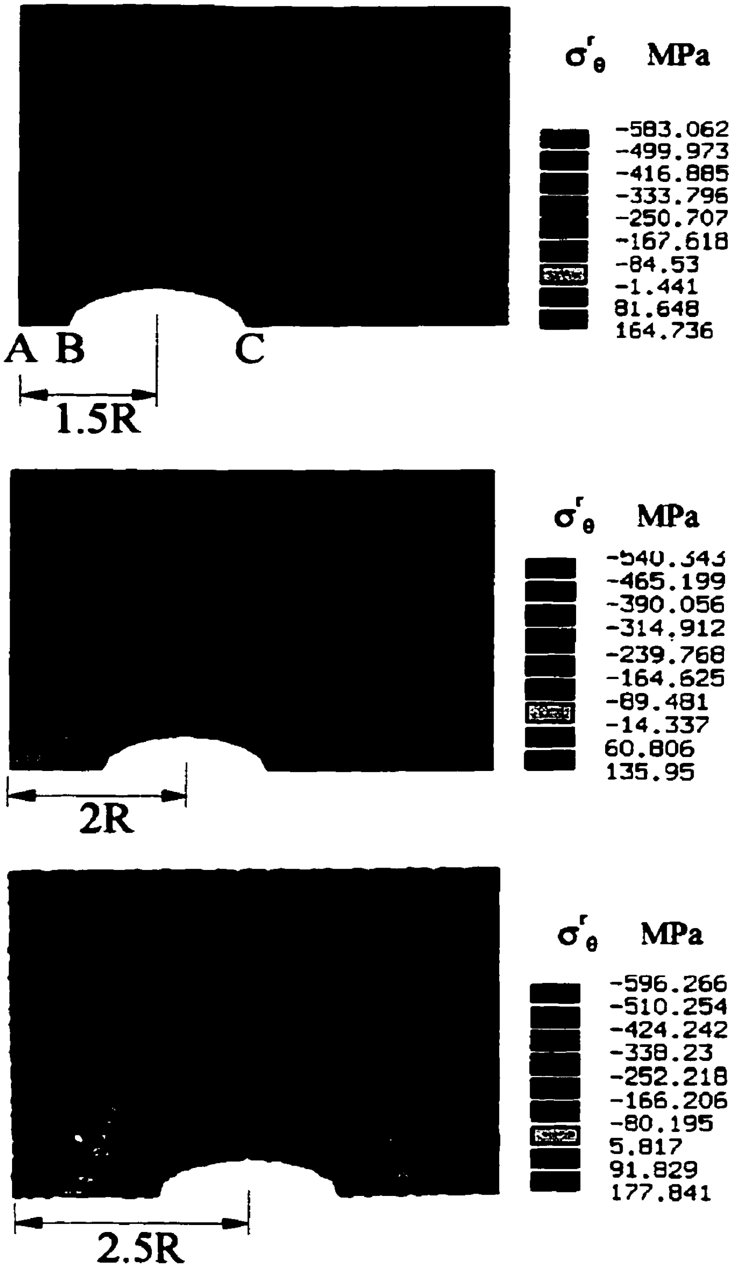

Fig. 5-10 Tangential residual stress σ^r_θ contours for 2% expansion.

The residual stresses at the entry and exit faces of the workpiece are shown in Fig. 5-11(a) and (b) for a centre distance of 4R and 2% expansion. The figures reveal that the smaller compressive residual stresses were always at the entry face of the workpiece. In the region between the two holes (Fig. 5-11(a)), the residual stress changes rapidly from compressive close to the hole edges to highly tensile at the central point A. This tensile stress is, however, more than twice of that predicted by axisymmetric analysis [90]. Fig. 5-11(b) also shows that interacting effects between the adjacent holes can lead to high tensile residual stresses even along the length CD. These high tensile residual stresses along lengths AB and CD combined with any tensile stresses resulting from the applied service load could lead to premature failure under conditions of cyclic loading.

5.1.4 Three Dimensional Analysis: Sequential Expansion

The work was further extended to account for the effect of sequential expansion of the two holes upon the residual stress field. In this case, half of the plate was modelled. The hole BC was expanded first, followed by the hole $C'B'$. Fig. 5-12 shows the variation of the tangential residual stress contours across the thickness of the plate at points B and B' for a centre distance of 4R and an expansion of 2%. For comparison, the results of the simultaneous expansion analysis are also provided. It is clear that the sequential expansion leads to lower compressive residual stresses at the exit face of the workpiece, as compared with the simultaneous expansion. The stresses at the entry face vary slightly.

Fig. 5-13 shows the variation of the tangential residual stress field in the region between the two holes for a centre distance of 4R and an expansion level of 2%. The figure indicates that the sequential expansion results in lower compressive residual stresses than the simultaneous expansion, especially at the exit face of the workpiece. It also shows that at the edge of the first expanded hole the residual stress field at the exit and entry faces become comparable.

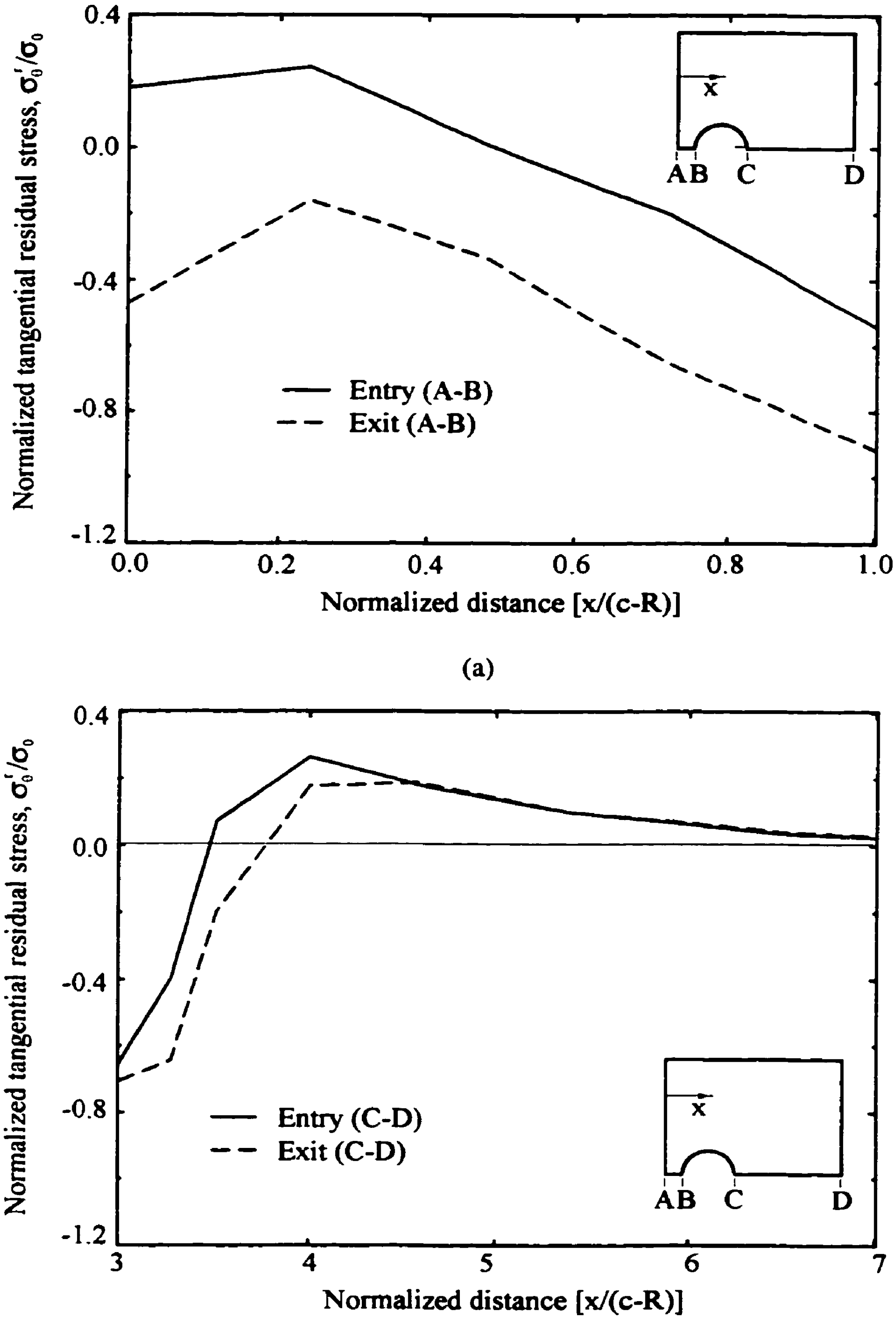

(a)

(b)

Fig. 5-11 Variation of normalised tangential residual stress σ^r_θ/σ_0 along lengths (a) AB and (b) CD.

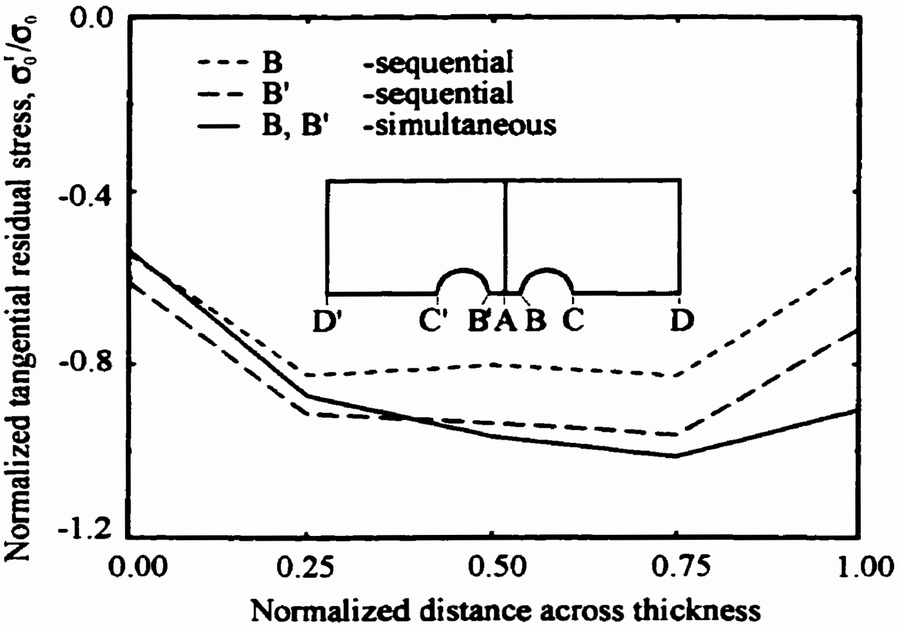

Fig. 5-12 Variation of normalised tangential residual stress σ^r_θ/σ_0 through thickness at points B and B' for sequential expansion.

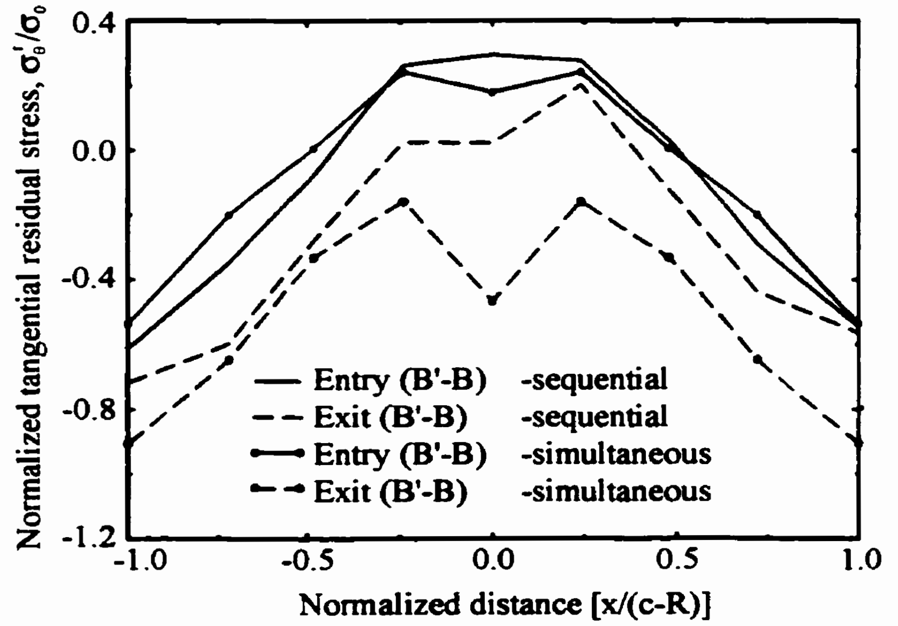

Fig. 5-13 Variation of normalised tangential residual stress σ^r_θ/σ_0 along length BB'.

Three Dimensional Analysis: Instrumented Cold Hole Expansion

The strain data corresponding to the upper face of the plate during the hole expansion were extracted from the ANSYS models (Fig. 3-6) with different coefficients of friction. MatLab was then used to obtain estimates of the strains over the required gauge locations. Fig. 5-14 compares the finite element results with the strains recorded during the sequential hole expansion process, for the first expansion. For both gauges G1 and G2 (see Fig. 4-4), the finite element results capture the overall response of the system. The overall pattern of the experimental and modelling results confirms that a simple two dimensional model would not be capable of capturing the three dimensional nature of the expansion process. The recorded strains for G1 of 4.5%, which would be considered the *average* value over 1.5 to 1.8 R, shows that even for a 2% level of expansion, there is a large plastic zone. The response of the gauges applied before and after the expansion process was consistent in subsequent loading. This demonstrated that the gauges were not damaged during the expansion process, and that the recorded strains are valid.

The closest agreement of the experimental results and the model were obtained for μ=0.30. This value was then used in the high resolution finite element model. The tangential stress results of the model are shown in Fig. 5-15.

The figure shows the results of a 2% expansion level experienced by the model shown in Fig. 3-6(b) for a separation distance 3R. The fine mesh in the vicinity of the hole helps in capturing the high stress gradient. The surface and subsurface compressive stresses vary by 50% through the thickness of the plate, and by up to 70% around the circumference of the fastener hole. The reduced stiffness of the component due to the closely spaced adjacent fastener hole is exhibited in the reduced peak stress observed on the left side with respect to the right side. Of particular interest is Fig. 5-15(b), which illustrates that the subsequent expansion of the adjacent fastener hole reduces the compressive tangential stresses at *both sides* of the original hole. Furthermore, there exists large tensile residual stresses between these adjacent holes. This emphasises that extreme care must be taken in the analysis of the fatigue fracture behaviour, when closely spaced fastener holes are considered.

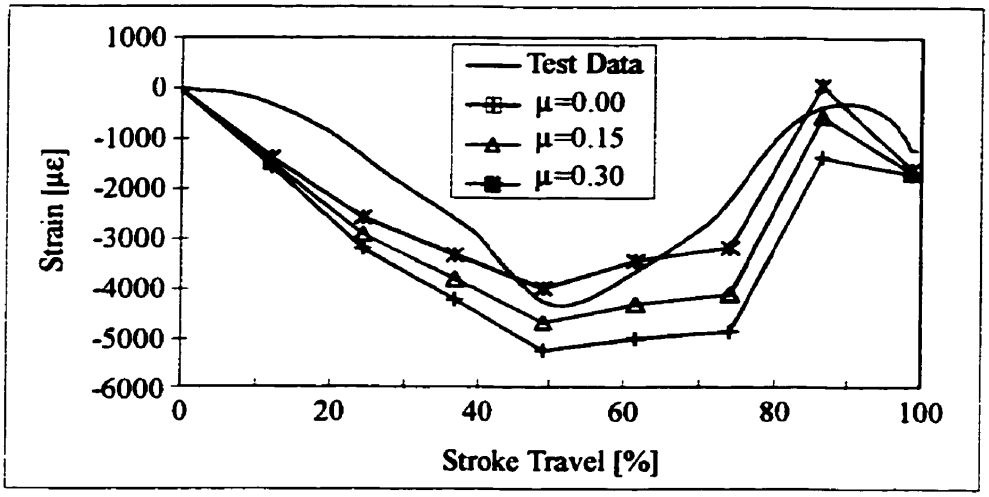

(a)

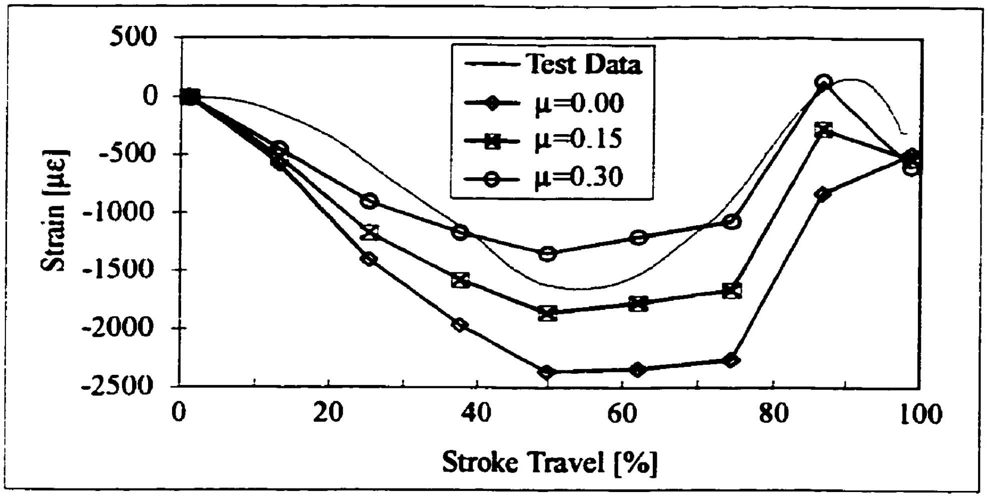

(b)

Fig. 5-14 Comparison between measured and finite element predicted strains at surface of plate during cold hole expansion at gauge locations (a) G1 and (b) G2.

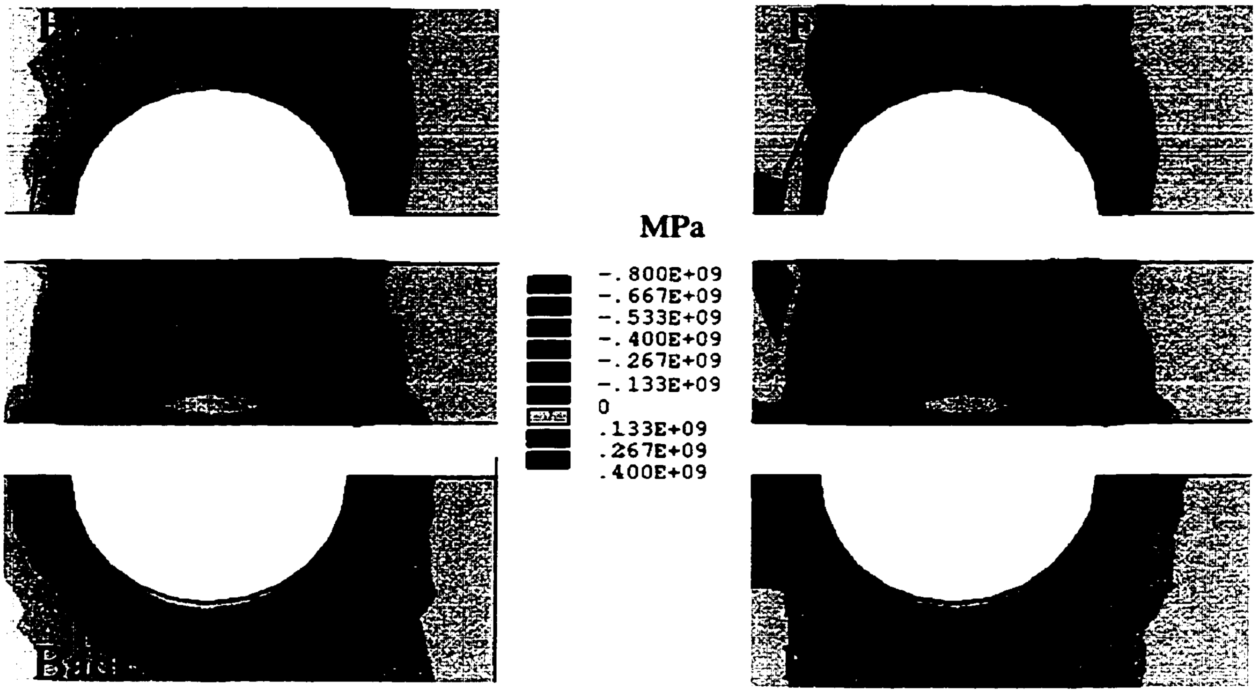

(a) (b)

Fig. 5-15 Tangential residual stress σ^r_θ contours for 2% sequential expansion with a separation distance 3R: (a) after first hole expansion and (b) after adjacent hole expansion.

5.2 Dynamic Modelling of Shot Peening

5.2.1 Validation of the Model

In order to verify our model, a comparison with the work of Edberg et al. [91] was conducted. The target and shot characteristics considered for verification were the same as those selected by Edberg et al. [91]. It should be noted, however, that these parameters do not represent true peening parameters, but this case was the only comparable published work available. While not identical, the results demonstrated substantial agreement.

The algorithms employed in the dynamic analysis of the impact utilise damping coefficients to reduce high frequency oscillations. For the single shot model investigated, this results in a decrease in the total energy of the system of 1.8%. This error resulted in a slight difference between the increase of the internal energy of the target and the change of the kinetic energy of the shot.

5.2.2 The Single Shot Model

Five aspects of the single shot model were examined. The first was concerned with the effect of the shot velocity, the second with the shot size and shape, the third with the effect of shot obliquity and friction, the fourth with the strain hardening coefficient and the fifth with strain rate sensitivity upon the plastic zone development and unloading residual stresses.

Effect of Shot Velocity

The single shot finite element analysis was conducted on high strength steel targets of mass density ρ=7800 kg/m^3 and a modulus of elasticity E=200 GPa. The elasto-plastic behaviour was assumed to be bilinear with an initial yield stress σ_o=600 MPa and a strain-hardening coefficient H'=800 MPa. The shot used was assumed to be rigid with a radius R and velocity v.

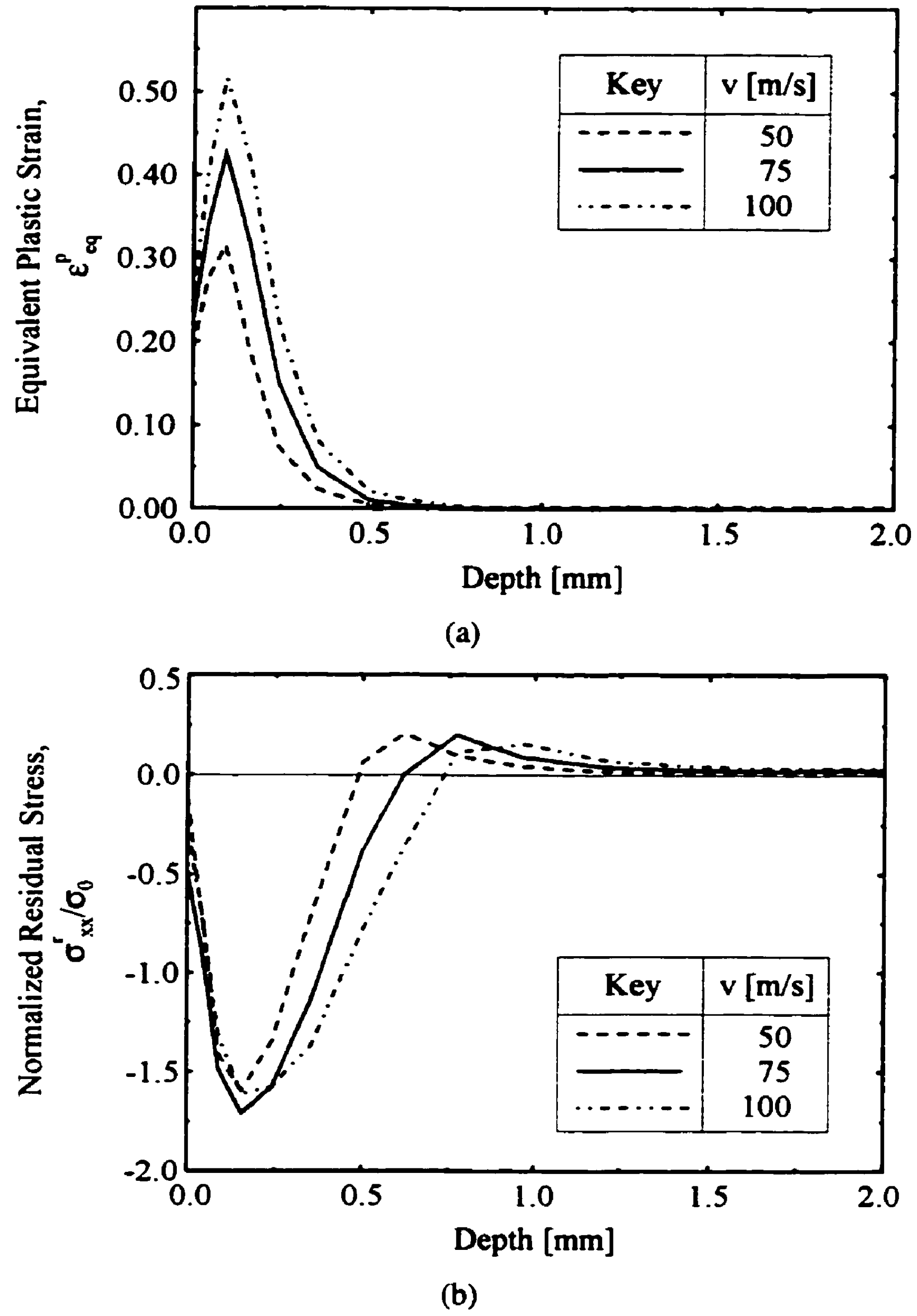

Fig. 5-16 Effect of shot velocity upon (a) equivalent plastic strain versus depth and (b) normalised transverse residual stress versus depth.

Three different impact velocities were used: 50, 75 and 100 m/s. The model was conducted using a steel shot with a radius R=0.5 mm. Fig. 5-16(a) and (b) show the variation of the equivalent plastic strain ε^p_{eq} and normalised unloading residual stress σ^r_{xx}/σ_o, beneath the centre line of the shot, with the depth of the treated target for the three impact speeds selected. These figures reveal that a 100% increase in the shot velocity results in: (i) an increase in the maximum equivalent plastic strain by 65%, (ii) a significant increase in the depth of the compressed layer, and (iii) an insignificant change in the position and the magnitude of the maximum residual σ^r_{xx} stress. It was also interesting to note that the change in the residual stress from compression to tension coincides with the limiting depth of the plastic zone.

Effect of Shot Size and Shape

Fig. 5-17 shows the σ^r_{xx} stress trajectories for the entire target, while Fig. 5-18 shows the corresponding normalised residual stress σ^r_{xx}/σ_o beneath the centre line of the shot for different shot radii. The shot was assigned a velocity v=75 m/s and the target material was assigned a strain hardening coefficient H'=800 MPa. Interestingly, the results indicate that in spite of the increase in the volume of the plastically deformed material with the increase in the shot radius, the magnitude of the surface and maximum subsurface residual stress σ^r_{xx} remain unchanged. However, the position at which the maximum subsurface stress takes place increases with the increase in the shot radius.

The work also accounted for the effect of the shape of the shot upon the normalised residual σ^r_{xx}/σ_o variation with depth. In this case, the shot was modelled in the form of an ellipsoid with major and minor dimensions being a and b, respectively. Mesh refinement was used to ensure the validity of the results. Fig. 5-19 shows clearly the effect of the aspect ratio (a/b), for the same mass of the shot, upon the residual stress field. It was worth noting that the decrease in the aspect ratio results in an increase in the maximum subsurface residual stress σ^r_{xx} . This was, however, coupled with an increase in the surface roughness of the target, as evidenced by Fig. 5-20(a) to Fig. 5-20(c), where a pronounced pile-up was apparent for the case when a/b=0.5. In typical shot peened components, multiple indentations resulting from full coverage will reduce the effect of the pile-up.

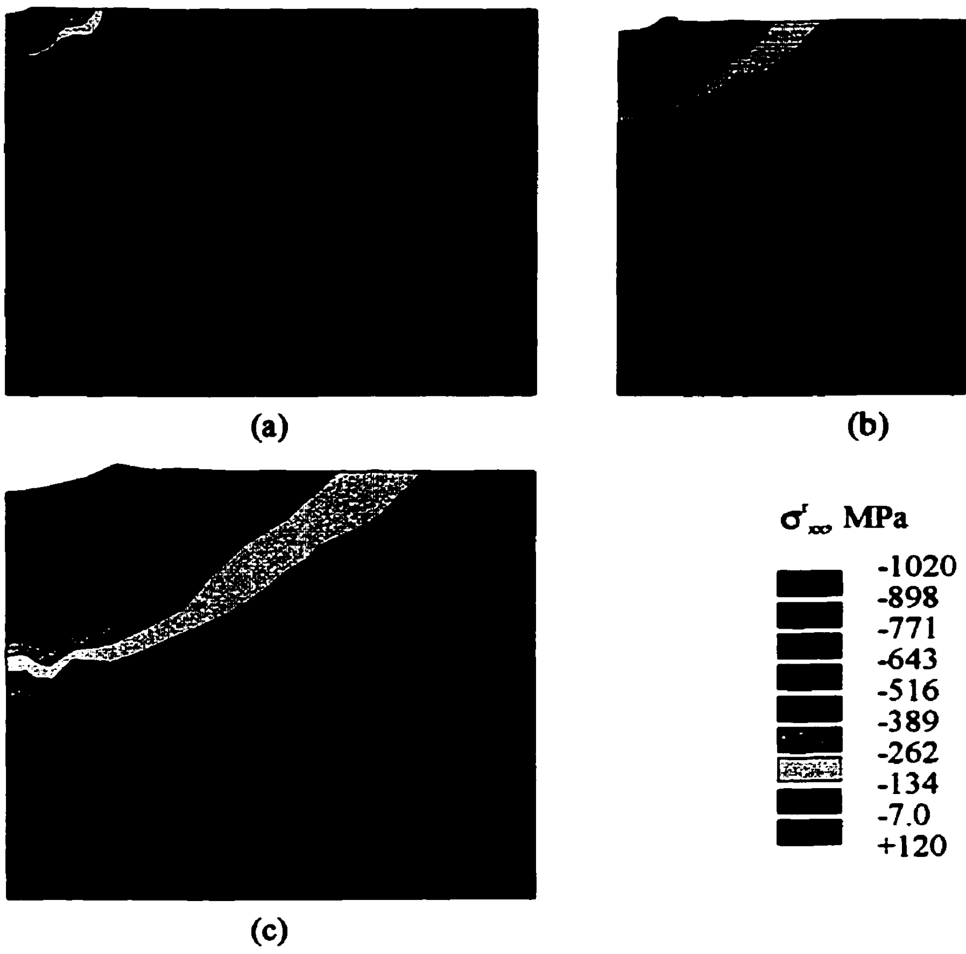

Fig. 5-17 Stress contours for (a) R=0.25 mm, (b) R=0.5 mm and (c) R=1.0 mm.

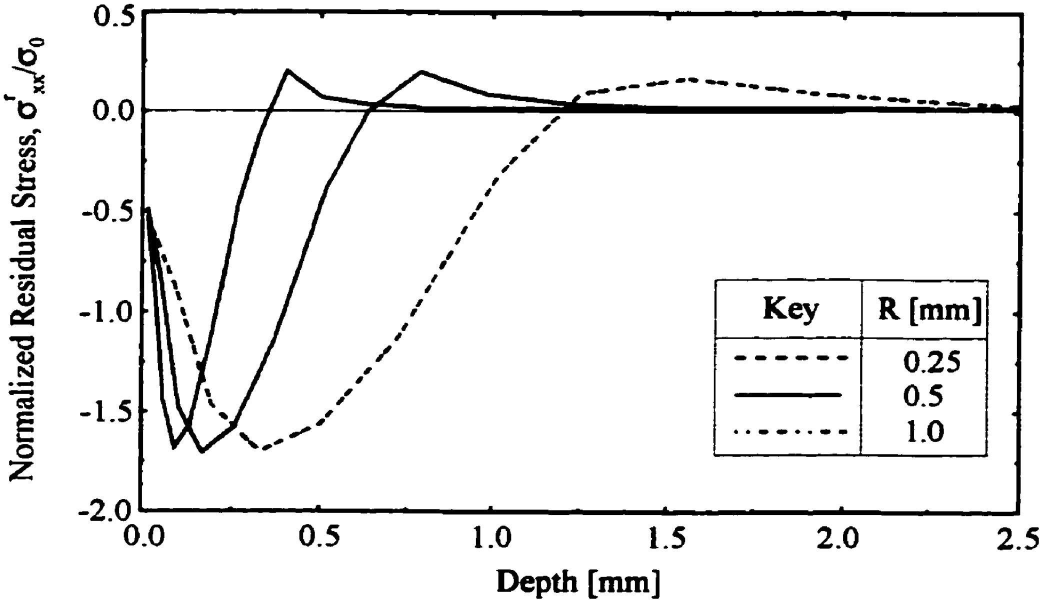

Fig. 5-18 Effect of shot size upon normalised transverse residual stress distribution beneath the centreline of the shot for velocity v=75 m/s and target strain hardening rate H'=800 MPa.

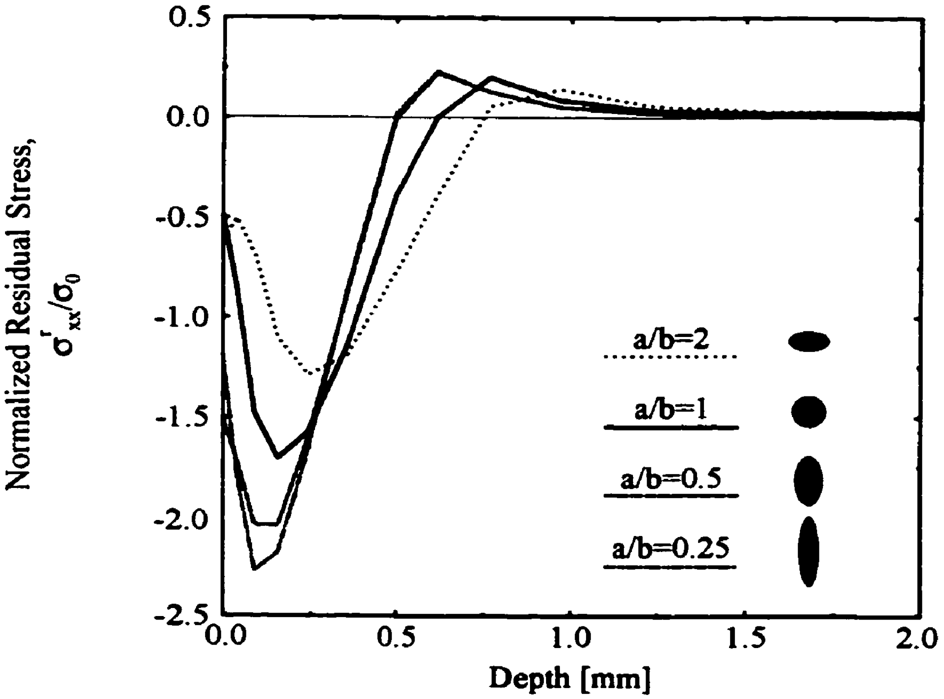

Fig. 5-19 Effect of shot aspect ratio upon normalised transverse residual stress.

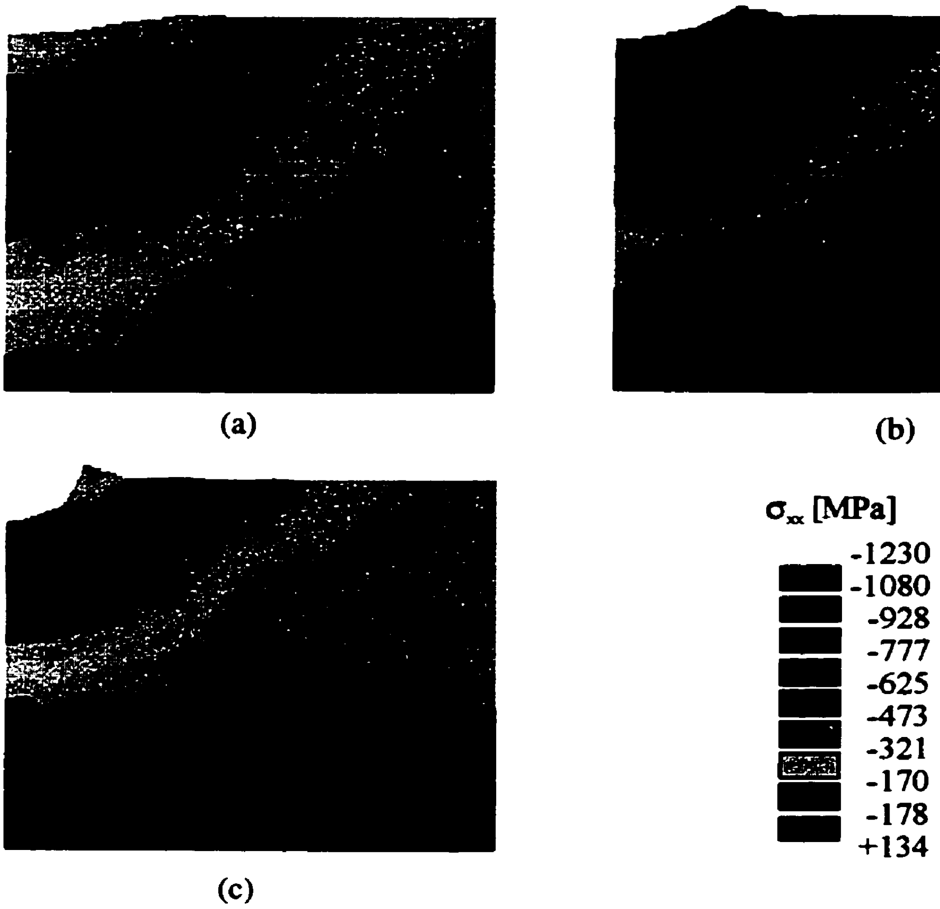

Fig. 5-20 Effect of shot shape upon the transverse residual stress contours: (a) shot aspect ratio $a/b= 2$, (b) $a/b= 1$ and (c) $a/b= 0.5$, for the same shot mass with velocity $v=75$ m/s and target strain hardening rate $H'=800$ MPa.

Effect of Shot Obliquity and Friction

A large amount of the kinetic energy of the shot in any peening treatment is expended in plastic work. If the travelling shot impinges the target obliquely, then the kinetic energy available for plastic work is reduced since only the normal component of the velocity will contribute to it. The tangential component will only influence the geometry but not the depth of the indentation. Fig. 5-21 and Fig. 5-22 show the effect of the impact angle upon the depth of the compressed layer as well as the residual stress field for an impact velocity $v=75$ m/s and obliquity (α) of 0 through 60 degrees using $H'=800$ MPa and $\mu=0.2$. The results show clearly that: (i) depth of the plastic zone decreases with increasing obliquity, (ii) the maximum compressive residual stresses decrease with the increase in obliquity and (iii) an asymmetric plastic zone develops as a result of the obliquity. Fig. 5-23 shows that, for an incident angle of 45°, the depth of the compressive layer beneath the centre of impact was not affected by the coefficient of friction. While increased friction did decrease to a small degree the maximum subsurface stress, it has a significant affect upon the surface stress.

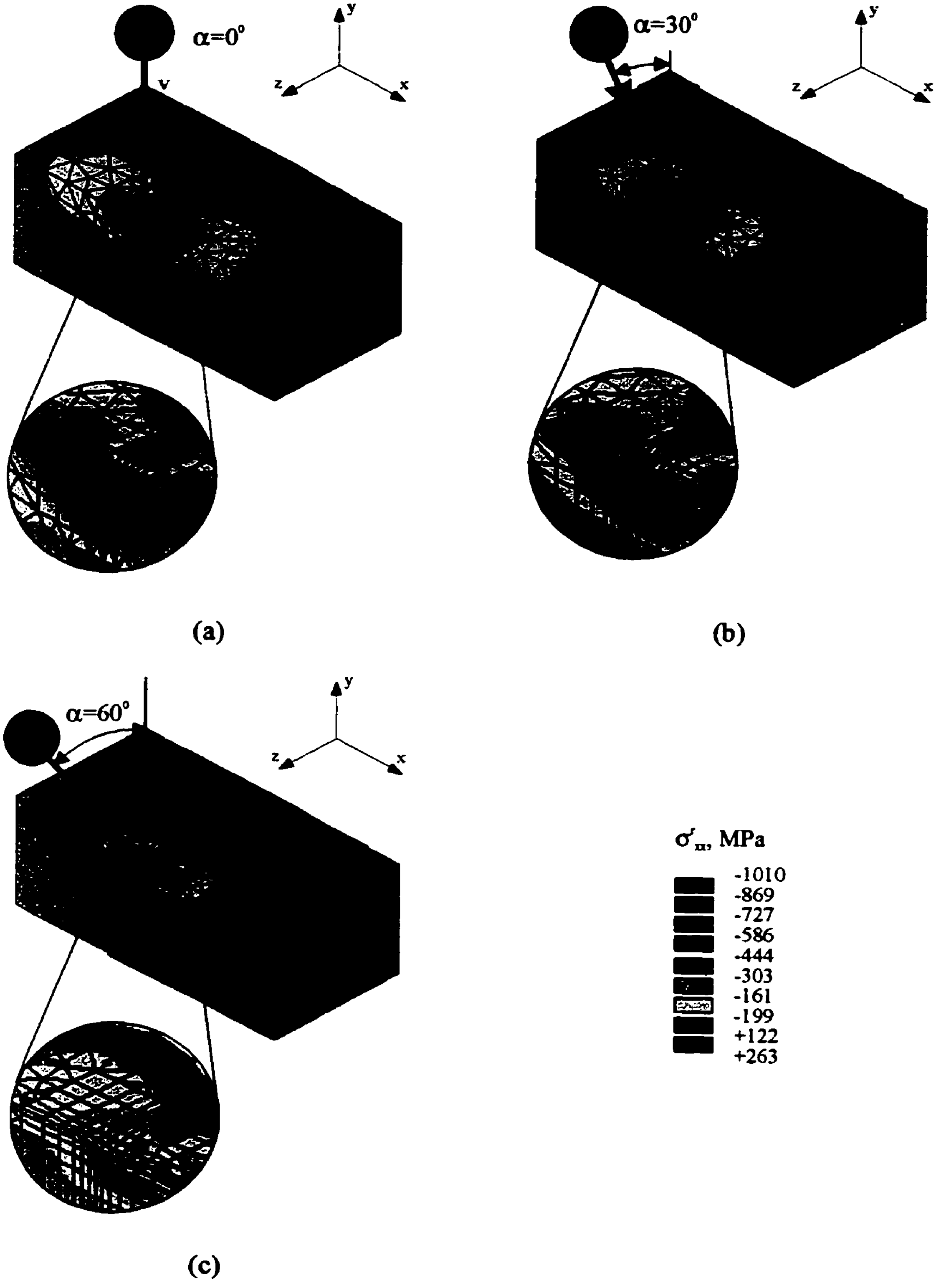

Fig. 5-21 Effect of shot obliquity upon transverse residual stress contours.

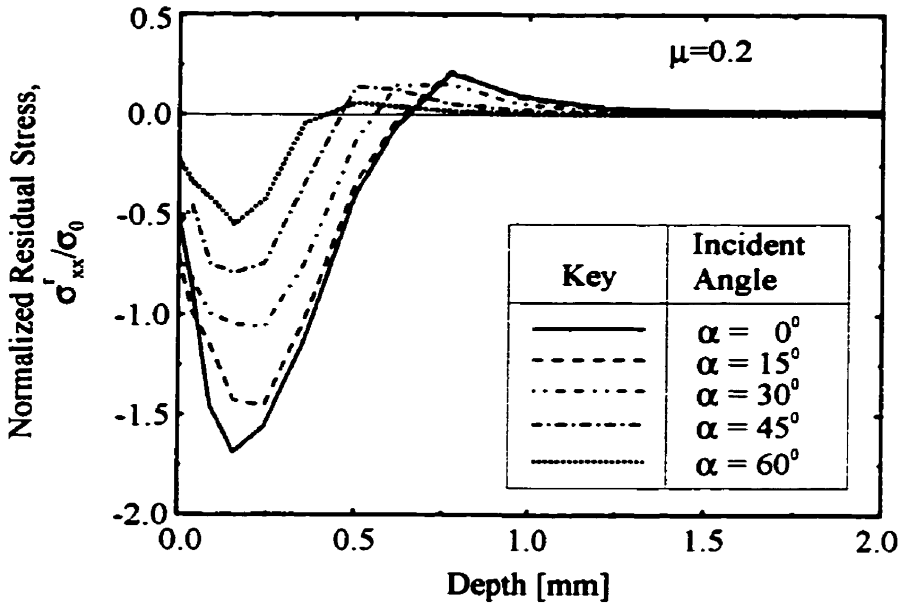

Fig. 5-22 Effect of shot obliquity upon normalised transverse residual stress distribution beneath the centreline of the impact for a velocity v=75 m/s, radius R=0.5 mm and μ=0.2.

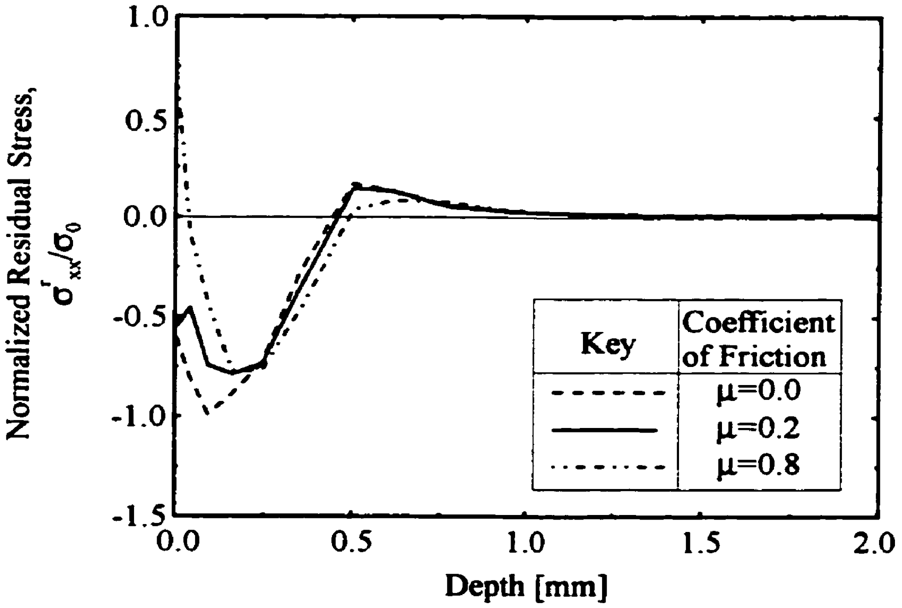

Fig. 5-23 Effect of friction upon normalised transverse residual stress distribution beneath the centreline of the impact for a velocity v=75 m/s, radius R=0.5 mm and obliquity α=45°.

Effect of Target Hardening Characteristics

The effect of target hardening characteristics was examined by assigning different hardening coefficients H' to the assumed bilinear material model. The shot radius and velocity selected were 0.5 mm and 75 m/s, respectively. Fig. 5-24 shows the residual stress variation with the depth of the target for three different values of hardening rates, 50, 800 and 1600 MPa. These values correspond to $H'/E=0.025\%$, 0.4% and 0.8%, respectively. The following observations can be made from Fig. 5-24. Increasing the hardening coefficient of the material results in an increase in the depth of the compressed layer, little or no change in the magnitude of the maximum subsurface residual stress, σ^r_{xx}, and a decrease in the surface residual stress.

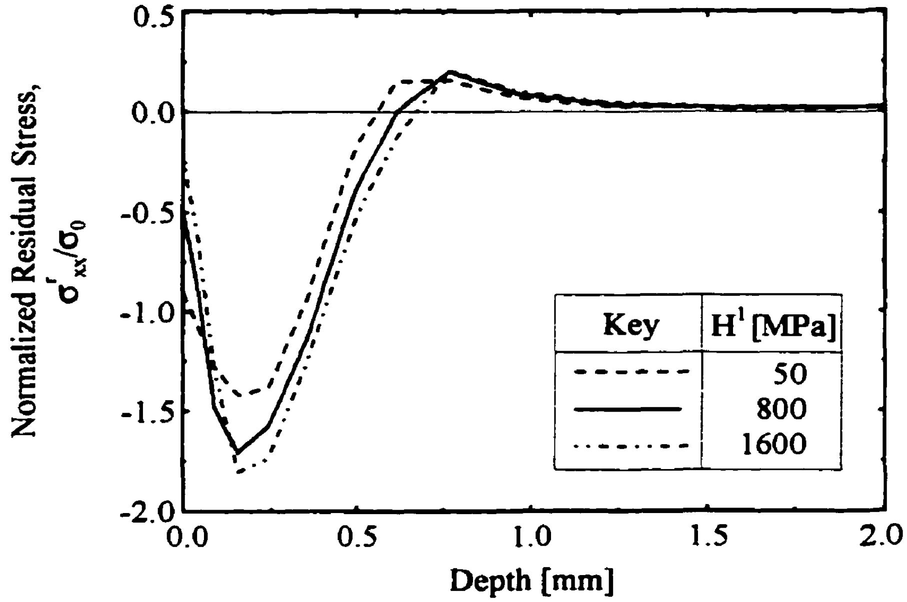

Fig. 5-24 Effect of strain hardening rate upon normalised transverse residual stress distribution beneath the centreline of the shot for a velocity v=75 m/s and radius R=0.5 mm.

Effect of Strain Rate

The commercial code LS-Dyna was used to investigate the effect of strain rate upon the unloading residual stresses and plastic zone development. The shot radius and velocity selected were 0.5 mm and 75 m/s, respectively. LS-Dyna results were compared with ANSYS for rate independent material behaviour. The results of the two codes were in good agreement, providing additional evidence of the accuracy and validity of the finite element models used. The coefficients used in the Cowper and Symond overstress model were C=1200 and p=5 [84]. Peak strain rates were reported to be on the order of 10^6 s^{-1}. The results reveal that the elevated yield stress near the surface results in higher compressive and tensile residual stresses, but have no apparent effect on the surface residual stress (Fig. 5-25). The depth of the compressed zone was also reduced. However, the "overall" features of the strain rate sensitive and insensitive models were comparable. This, combined with the general absence of reliable data in the range of the strain rates experienced in the shot peening process, lead the author to conclude that the strain rate insensitive models were sufficient for evaluating the effect of the parameters investigated within this research.

5.2.3 Dynamic Simultaneous Impact Model

The work was further extended to account for the effect of two shots impinging the target simultaneously. Special attention was devoted to examining the effect of the separation distance between the shots, impact velocity and target hardening characteristics upon the resulting residual stress field.

Let us now focus our attention to the dynamic simultaneous impact results. Fig. 5-26 shows the effect of the separation distance upon the residual stress, σ^r_{xx}. The analysis was conducted using the mechanical properties outlined in the single shot model with separation ratios C/R= 1, 1.5 and 2. The effect of the separation ratio upon the residual stress field is evident at the centre line of the target, where interactions from the co-indenting spheres take place. However, insignificant interactions take place beneath the centre line of each shot, as evidenced by the distribution of the residual stress there.

The effect of the kinetic energy of the impinging shots for different separation ratios is shown in Fig. 5-27 (a) and Fig. 5-28(a) at the centre line of the target and in Fig. 5-27(b) and Fig. 5-28(b) beneath the centre line of the shot. The residual stress distributions of Fig. 5-27(b) and Fig. 5-28(b) resulting from simultaneous impact were very similar to those obtained from the single shot model. However, the single shot model

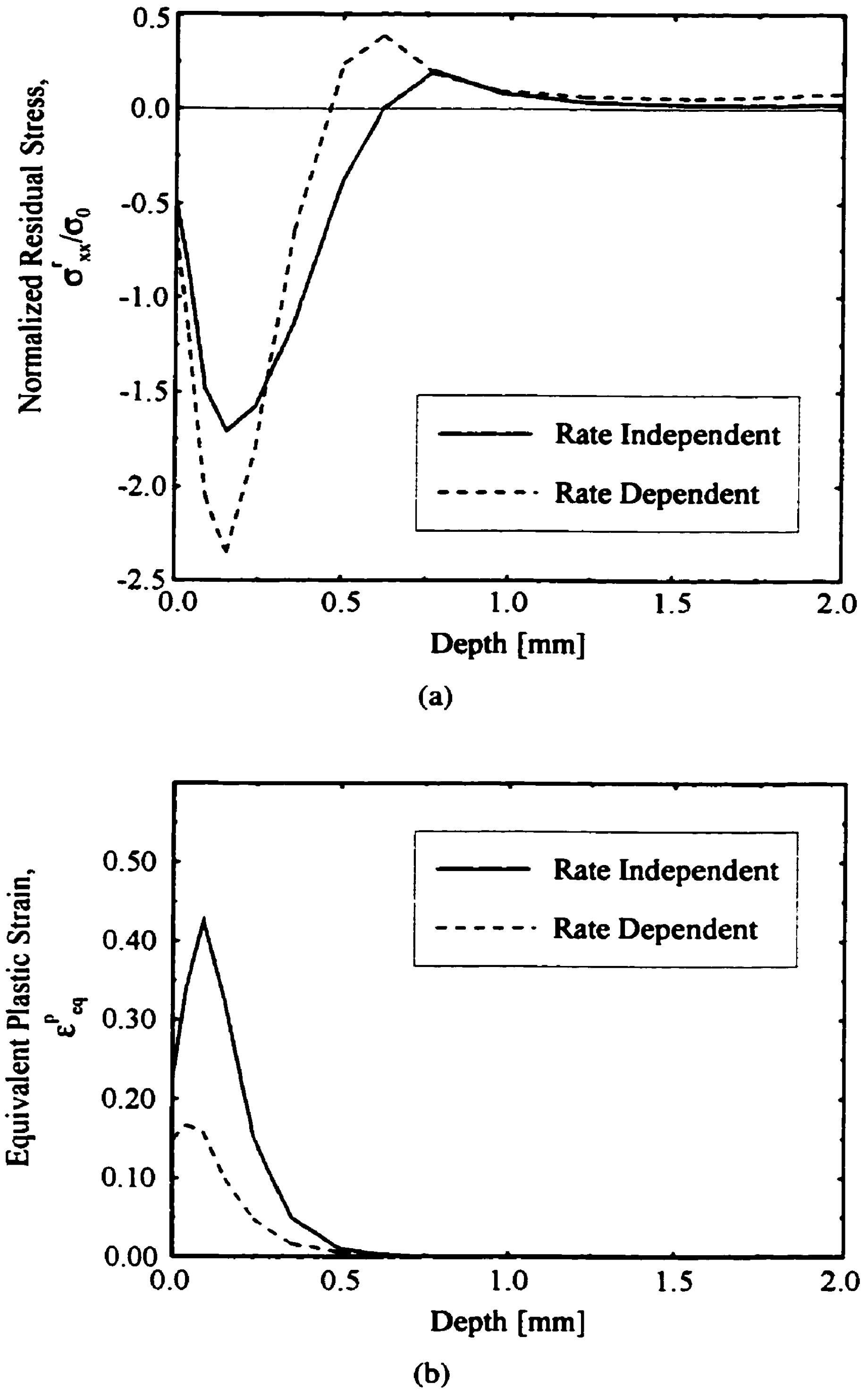

Fig. 5-25 Effect of strain rate hardening upon (a) normalised transverse residual stress distribution and (b) equivalent plastic strain beneath the centreline of the shot for a velocity v=75 m/s and radius R=0.5 mm.

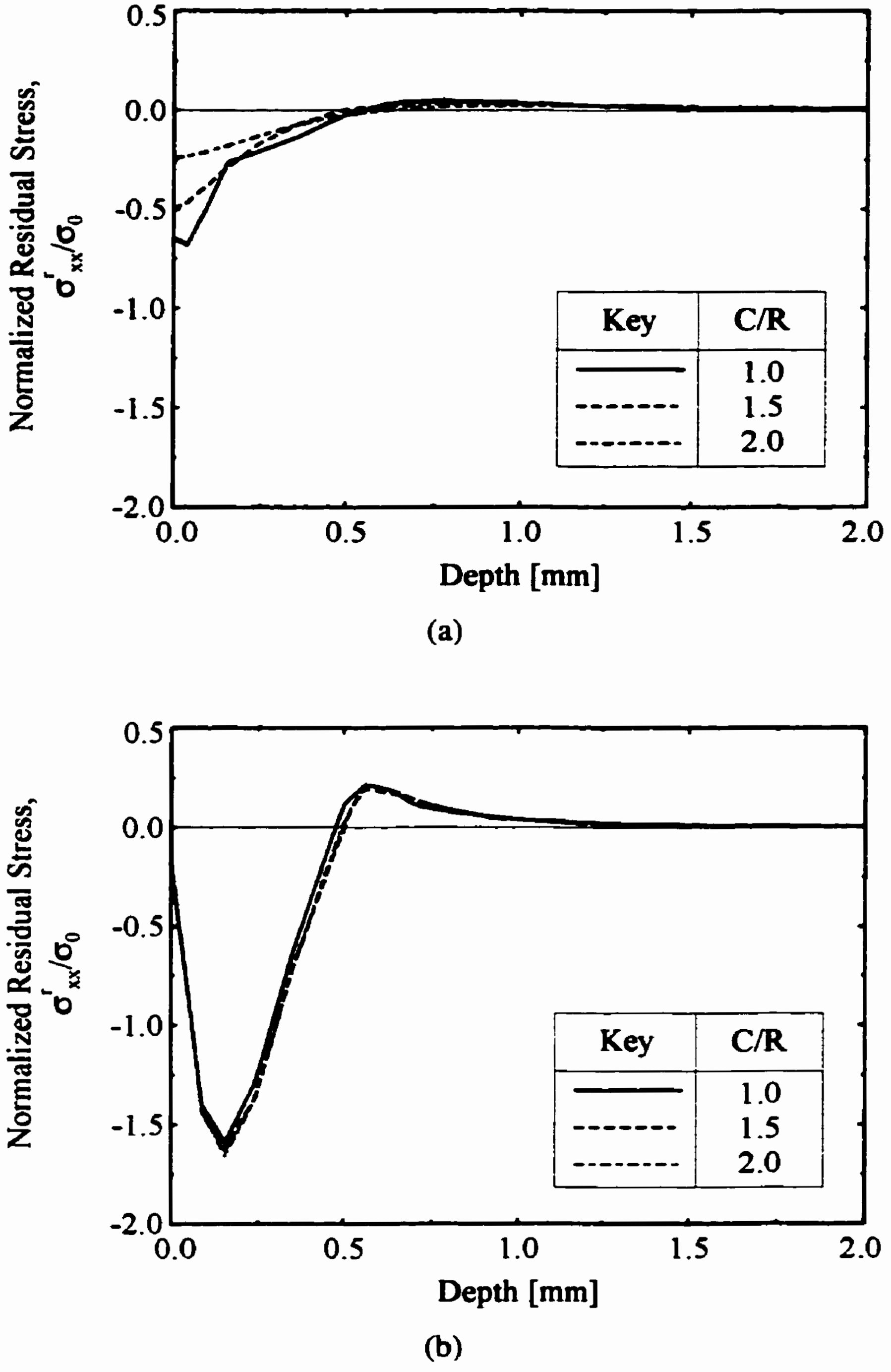

Fig. 5-26 Effect of separation distance between shots upon the normalised transverse residual stress field: (a) at the centre line of the target and (b) beneath the centre line of the shot.

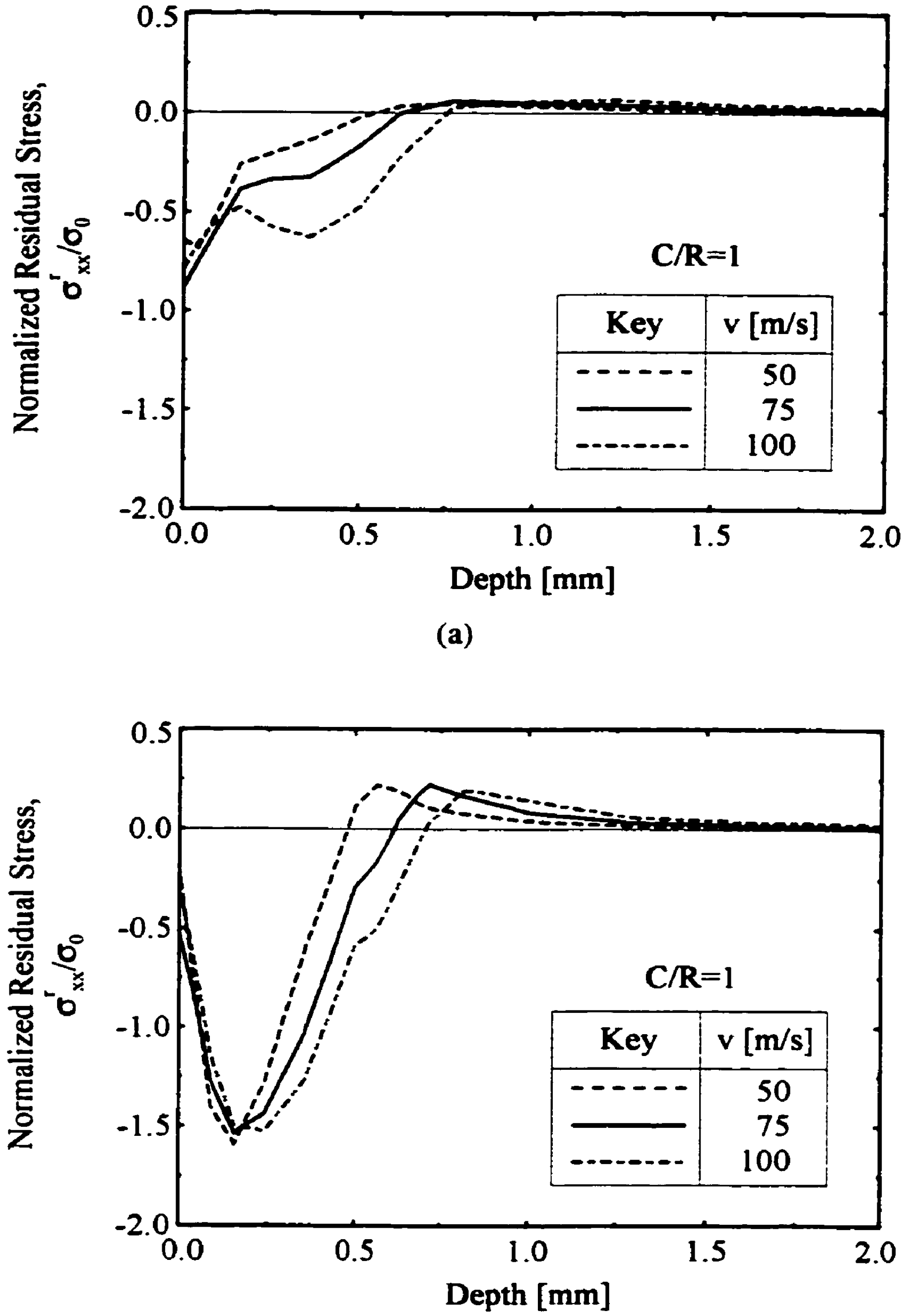

(a)

(b)

Fig. 5-27 Effect of shot velocity upon the normalised transverse residual stress field for separation distance C/R=1: (a) at the centre line of the target and (b) beneath the centre line of the shot.

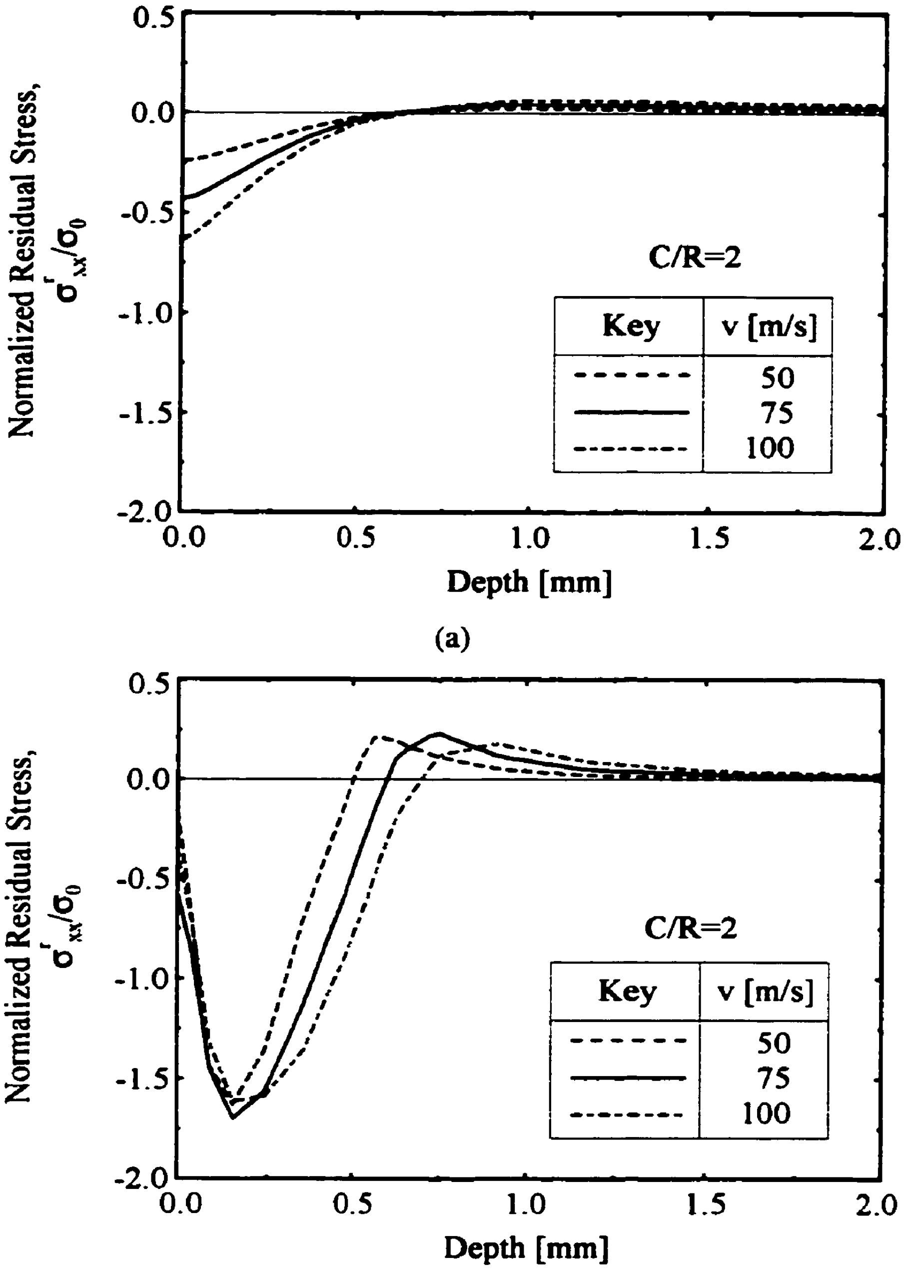

(a)

(b)

Fig. 5-28 Effect of shot velocity upon the normalised transverse residual stress field for separation distance C/R= 2: (a) at the centre line of the target and (b) beneath the centre line of the shot.

is incapable of predicting the relatively large compressive residual stresses present at the centre line of the target between the co-indenting shots, depicted in Fig. 5-27(a) and Fig. 5-28(a). These figures indicate that the maximum compressive stresses occur at the surface of the target. The transition from compression to tension occurs at comparable distances to those observed beneath the shot. The effect of the strain-hardening characteristics of the target was very similar to that observed in the single shot model.

5.2.4 "Realistic" FE Modelling of the Shot Peening Process

Building upon the previous work, a model of multiple arrays of shots, was developed. Of particular interest was the effect of the separation distance and the sequence of impact. The target was modelled as high strength steel and the shot was assumed rigid of radius R=0.5mm and velocity v=75 m/s. Given below are the results from the modelling of four arrays of shots impinging on the target with separation distances of C/R=1 and C/R =2 within a given array of shots. The arrays were offset and no interference between subsequent waves was allowed.

Examining Fig. 5-29, we observe that the stress contours resulting from the fourth array when C/R=2 were similar to those developed after the first array when C/R=1. Examining the corresponding normalised stress profiles beneath the centre of the shot in Fig. 5-30 and Fig. 5-31, as well as for the twin impact model (Fig. 5-26(b)), it was observed that all cases have similar profiles beneath the centre of the shot. It was therefore concluded that the sequence of impingement has little effect upon the resulting residual stress field beneath the shot for $C/R \geq 2$. Comparing Fig. 5-26(b) and Fig. 5-31(b), the depth of the plastic zone beneath the centreline of the shot increased. This was a result of the adjacent impacts limiting the spread of the plastic zone in the plane of the target surface. However, the maximum surface and subsurface compressive residual stresses were unchanged beneath the centre of impact. Study of the residual stress profiles at the centreline between the location of the shot impacts in Fig. 5-26(a) and section B-B in Fig. 5-31(b) shows again an increase in the depth of compressed material without a significant increase in the maximum compressive stress. The resulting profile is significantly different, with the residual stress profile rapidly decaying for the twin impact model. This is because of the large plastic strain induced in the material by the multiple impinging shots.

Fig. 5-30 and Fig. 5-31 highlight several important features arising from the overlap of the impacts from subsequent closely packed shot arrays. Firstly, the maximum surface and subsurface compressive stress increase with the overlapping shot arrays. Secondly, along all three sections in Fig. 5-30, the surface compressive stress increases after the fourth series of impacts. Thirdly, after the fourth array has rebounded, the maximum compressive stress beneath the centreline of the initial shot impact (A-A) was observed to be at the surface. Whilst the surface stress has increased, the maximum compressive stress has decreased significantly. Comparison of C-C after the first impact and A-A after the fourth in Fig. 5-30 shows that both exhibit similar features. However, the final subsurface residual stress beneath the initial impact point is less than that between the shots of the first impact. Moreover, Fig. 5-32 shows that the depth and magnitude of the plastic zone beneath the initial impact did not change. The plastic zone development and elastic recovery from the shots subsequent to the first array effectively negate the initial compressive stresses.

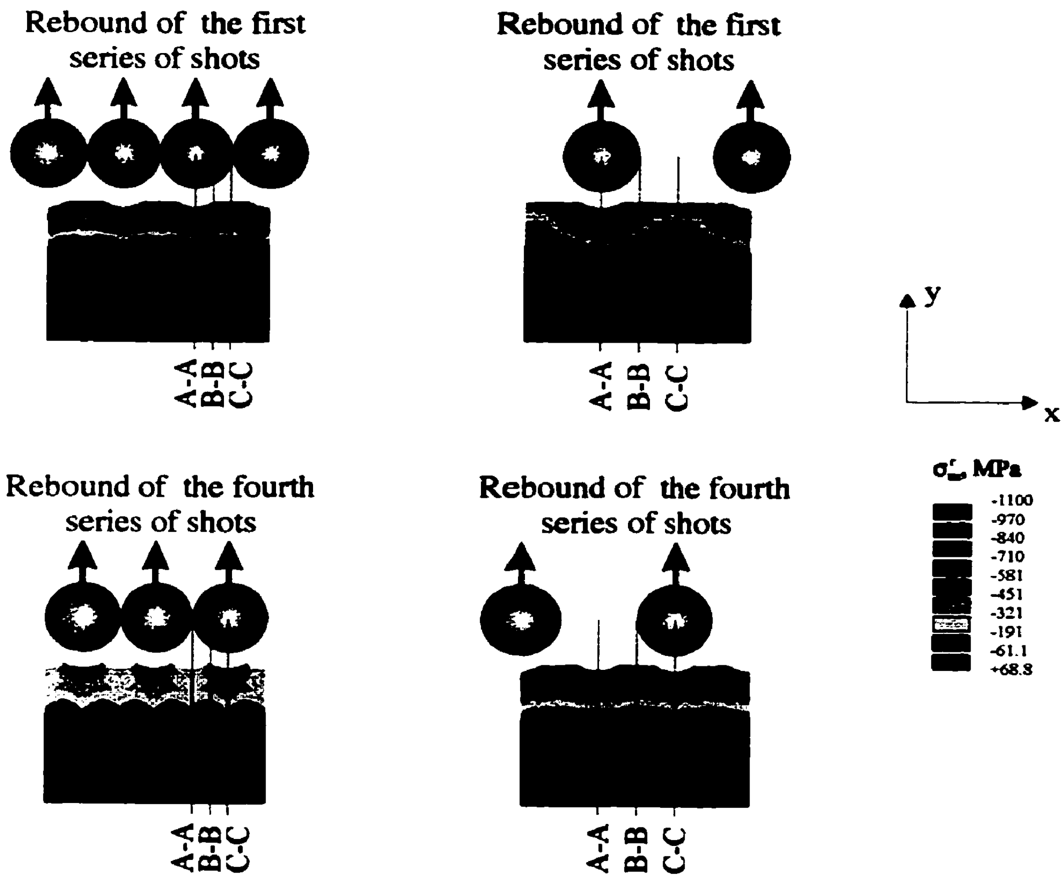

(a) (b)

Fig. 5-29 Residual stress contours for multiple impact for a separation distance of (a) C/R=1 and (b) C/R=2.

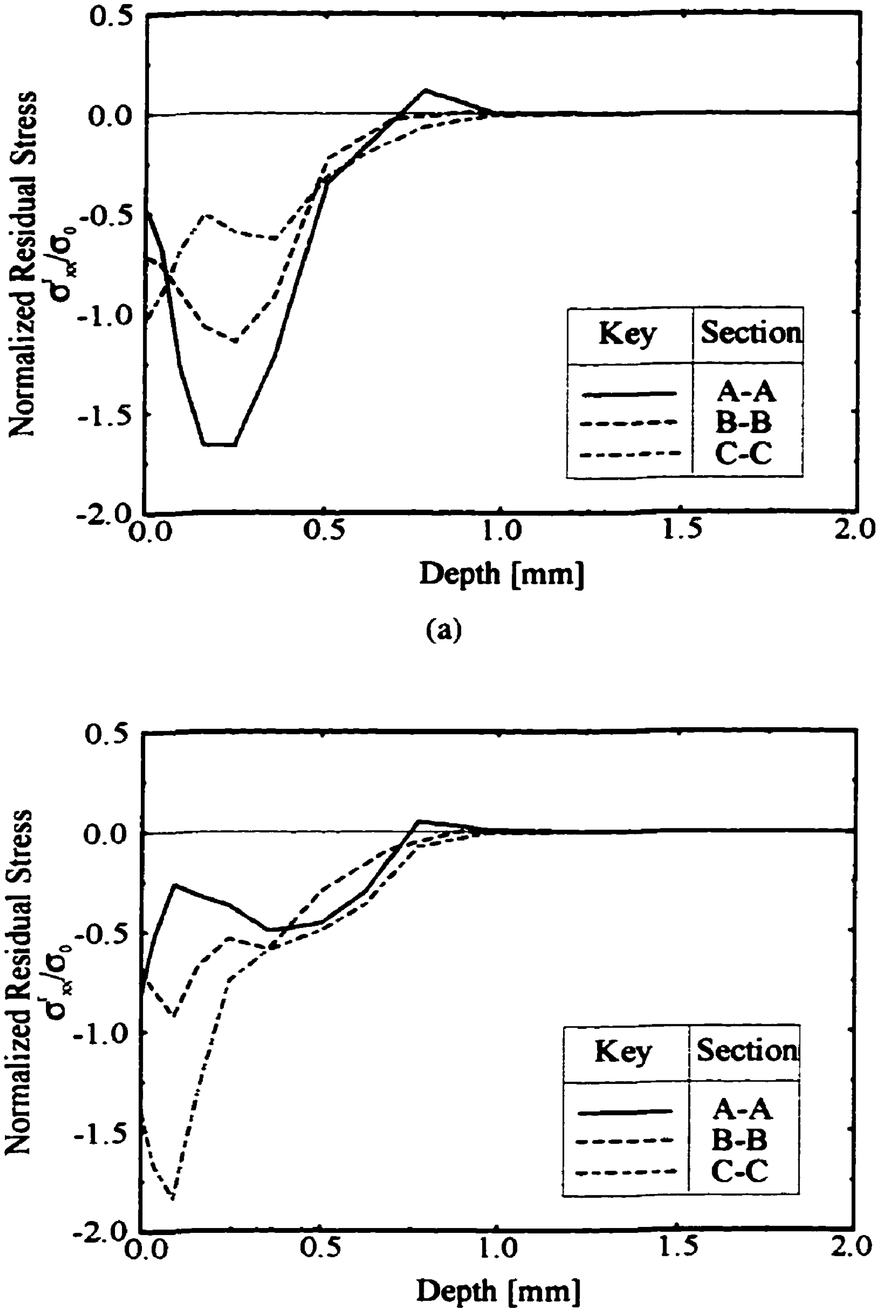

(a)

(b)

Fig. 5-30 Normalised transverse residual stress field for a separation distance of C/R=1 after rebound of (a) first and (b) fourth shot arrays.

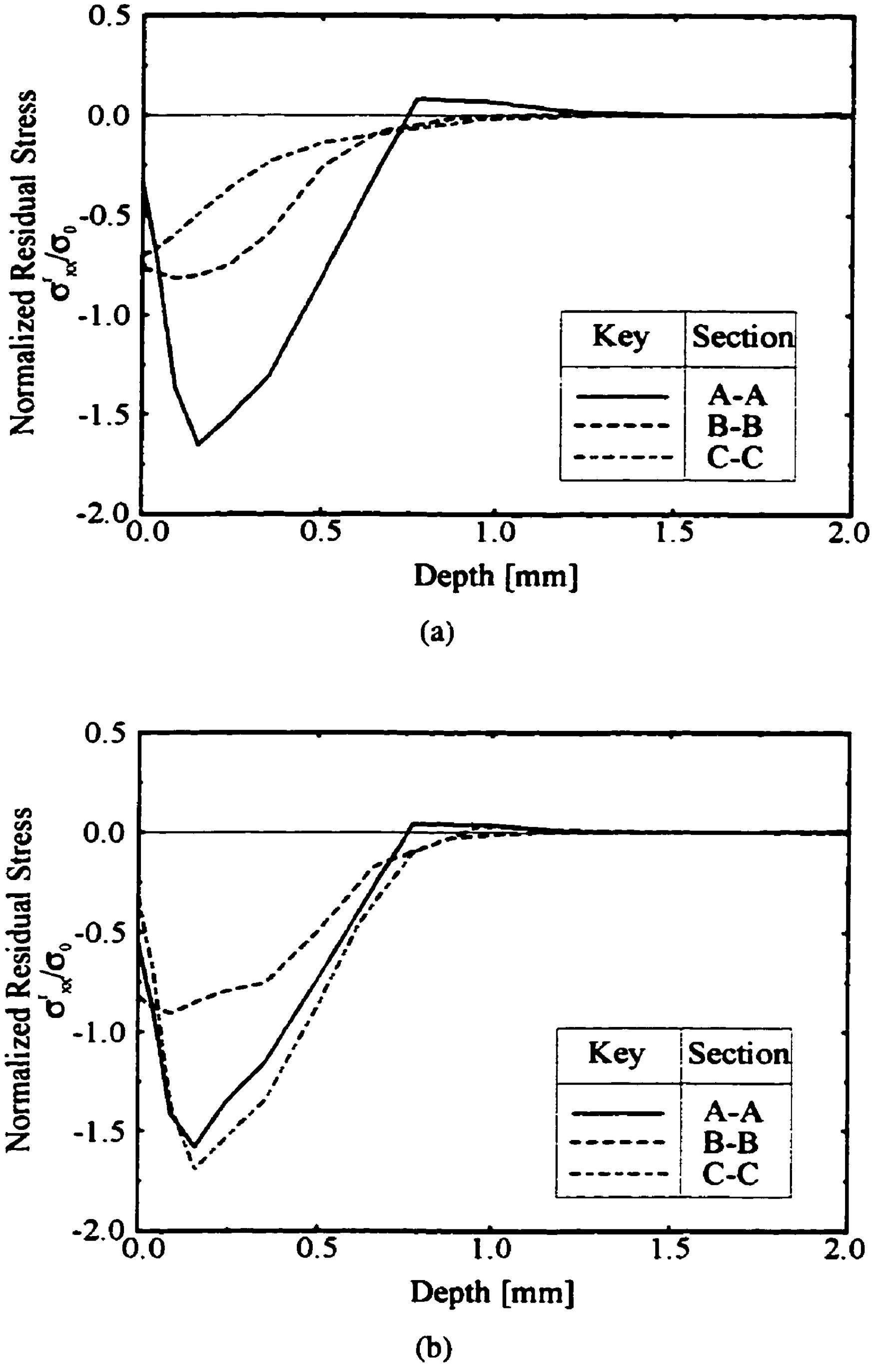

Fig. 5-31 Normalised transverse residual stress field for a separation distance of C/R=2 after rebound of (a) first and (b) fourth shot arrays.

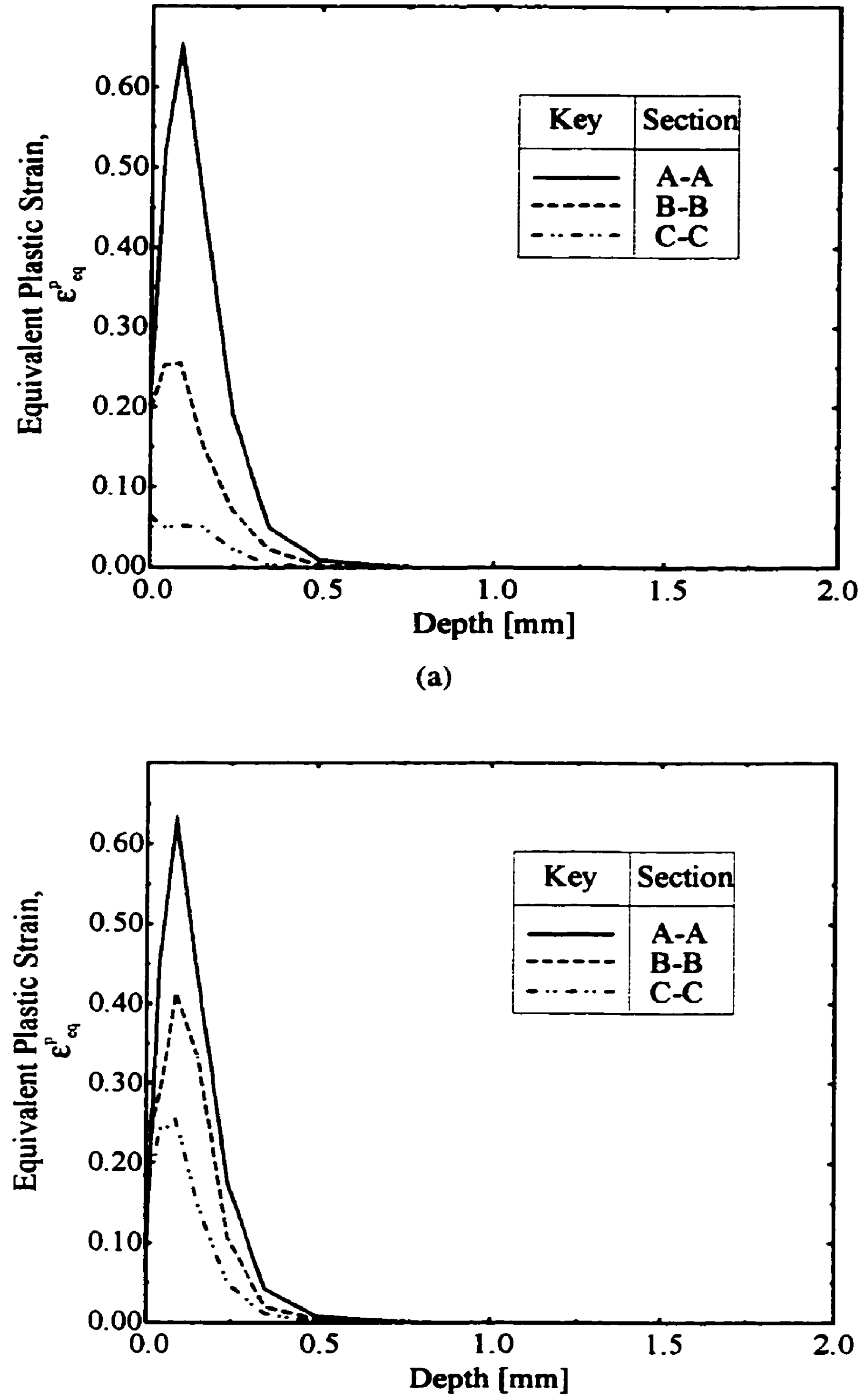

(a)

(b)

Fig. 5-32 Equivalent plastic strain distribution for a separation distance of C/R=1 after rebound of the (a) first and (b) fourth shot arrays.

5.3 Incremental Hole Drilling Method

Titanium Ti-6Al-4V coupons, supplied by Pratt & Whitney Canada, measuring 41 mm in diameter by 10 mm thick with an initial yield stress of σ_o=1024 MPa were subjected to a range of intensities of different peening treatments, from light (4N) to moderate (8A). These were then examined using the incremental hole drilling method. Measurements were made on each coupon, and the results show the average of three trials on each of two tested coupons per treatment, with a minimum deviation between trials amounting to a maximum error of 5%. Typical measured strains in the three gauges of the rosette are shown in Fig. 5-33. For the initial depths, the equal strains in all orientations were indicative of the equal biaxial residual stress field.

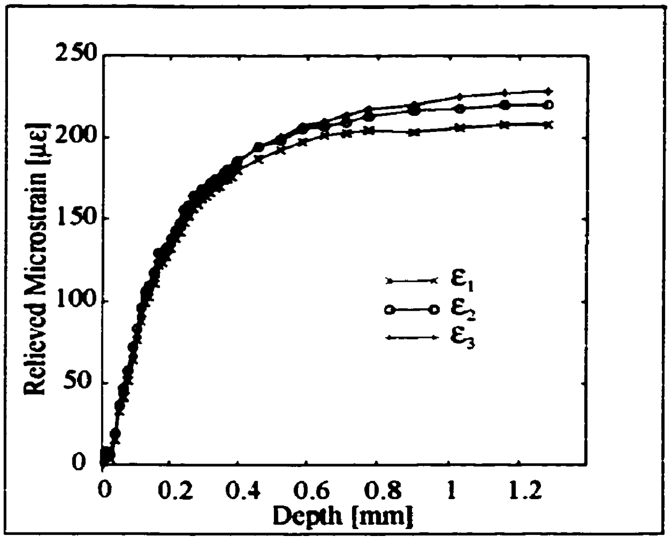

Fig. 5-33 Measured relaxed strains in peened Ti-6Al-4V to an Almen intensity of 8A.

Fig. 5-35 and Fig. 5-37 show the residual stress distributions obtained for the titanium coupons subjected to both steel and glass shot peening treatments, respectively. The coupons were also subjected to different levels of peening treatment. Each figure shows the results obtained using the incremental hole drilling technique. The equal biaxial stress field was calculated using equation (4.4). The strain ε_i was taken as the average of the three strains indicated by the three gauges. While the data was recorded in increments of 6.35 μm (0.25×10^{-3} inch) near the surface and 12.7 μm (0.5×10^{-3} inch) beyond 0.2 mm, the inversion technique was applied with 4 increments of 0.0127 mm (0.5×10^{-3} inch), 20 increments of 0.0254 mm (1.0×10^{-3} inch), 14 increments of 0.0635 mm (2.5×10^{-3} inch), and 10 increments of 0.127 mm (5.0×10^{-3} inch).

Fig. 5-34 provides a baseline using an unpeened sample for comparisons with other cases. Fig. 5-35 and Fig. 5-36 illustrate that with increasing peening intensity: (i) the level of the surface compressive stress increases, (ii) the level of the subsurface compressive stress increases, (iii) the depth of the maximum compressive stress does not change and (iv) the depth of the compressed layer increases.

There is no method for reliably determining the shot velocity or velocity distribution during the peening treatment. However, for a given class of shots, the peening treatment is primarily controlled by adjusting the pressure of the air stream carrying the shot, thereby increasing or decreasing the velocity. In comparison with Fig. 5-16, the increase in the depth of the compressed zone corresponded with the predictions of the finite element shot peening model, as did the consistent depth of the maximum compressive residual stress. The increased velocity would also result in an increased strain rate. The increased maximum compressive stresses shown in the strain rate sensitive model was also reflected in the experimental data (Fig. 5-25). In all cases, the measured residual tensile stress levels were insignificant.

The conclusions reached from the examination of the specimens subjected to glass bead peening (Fig. 5-37) agree with those obtained for the steel shot. Of particular note was the similarity of the residual stress profiles measured for the two 10N treatments. Both the steel (Fig. 5-35) and glass shot (Fig. 5-37(b)) result in a comparable subsurface compressive stress and depth of plastic zone. While the peening intensity does not provide any direct information about the compressive stress field resulting from the treatment, these results indicate that there is a reasonable measure of repeatability.

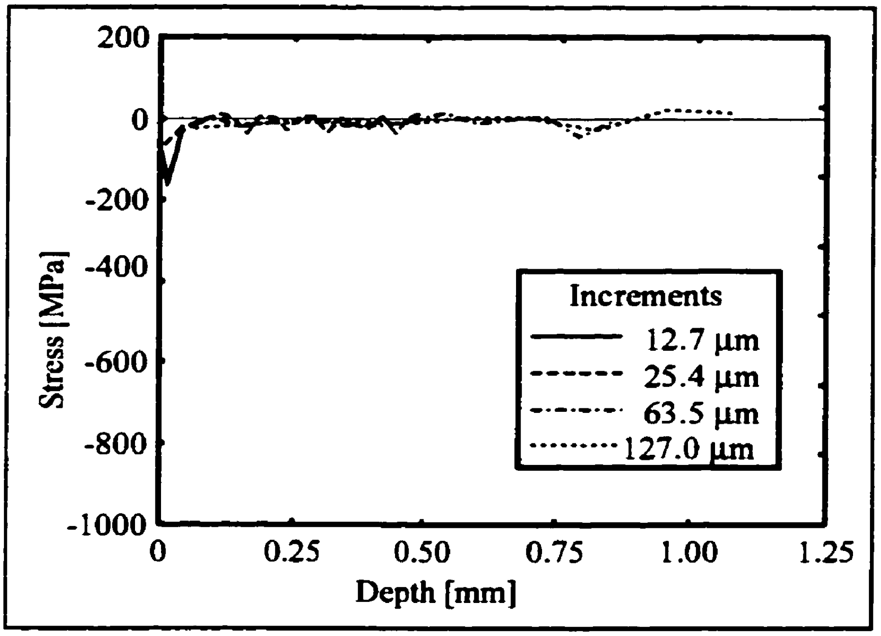

Fig. 5-34 Residual stress distribution for unpeened coupon.

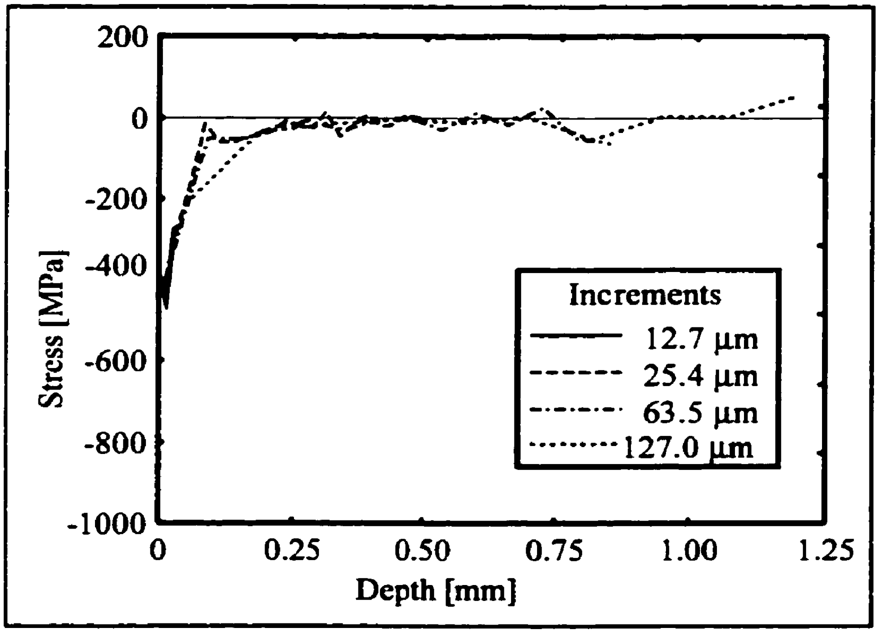

Fig. 5-35 Residual stress distribution of peened Ti-6Al-4V to an Almen intensity of 10N using steel shot.

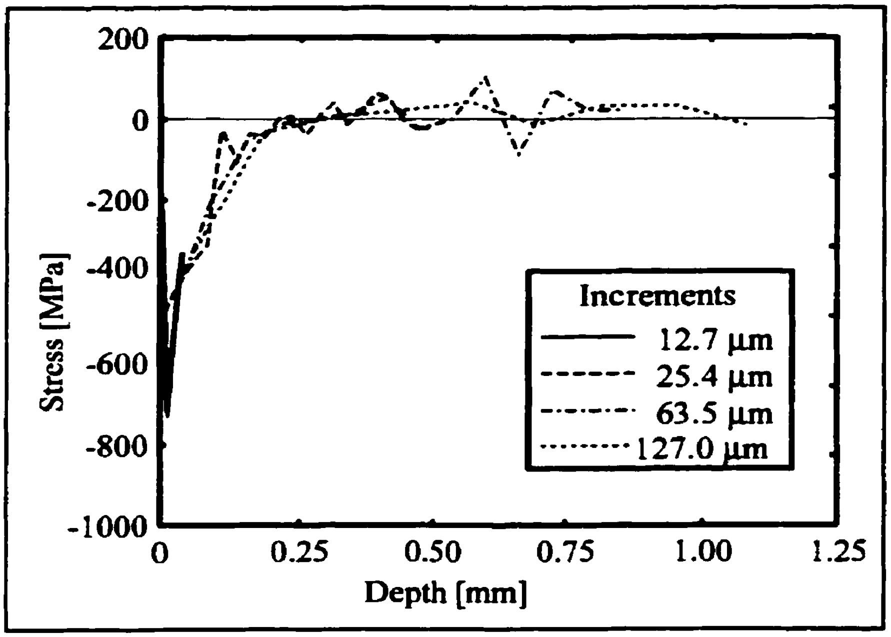

(a)

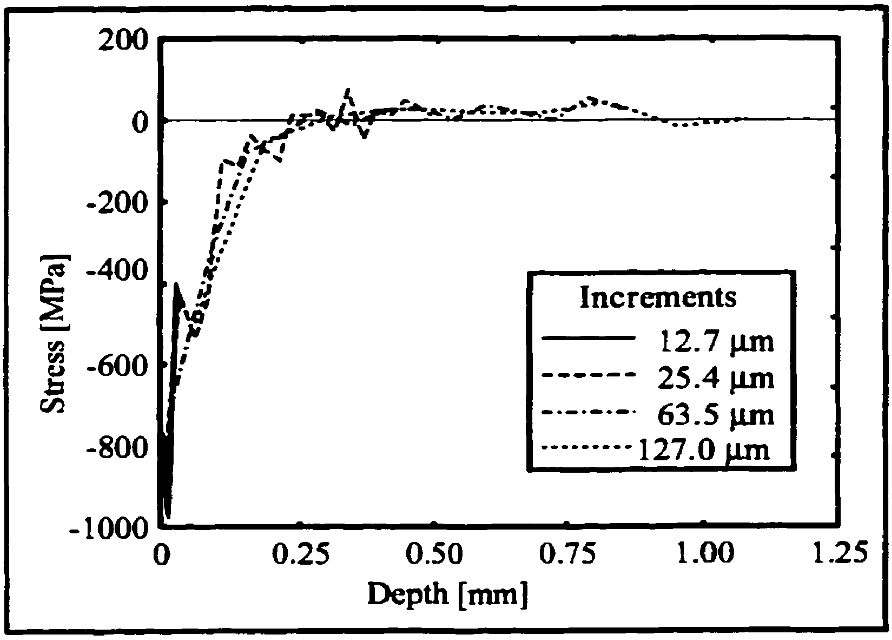

(b)

Fig. 5-36 Residual stress distribution for steel shot peening treatments: (a) 5A and (b) 8A Almen intensity.

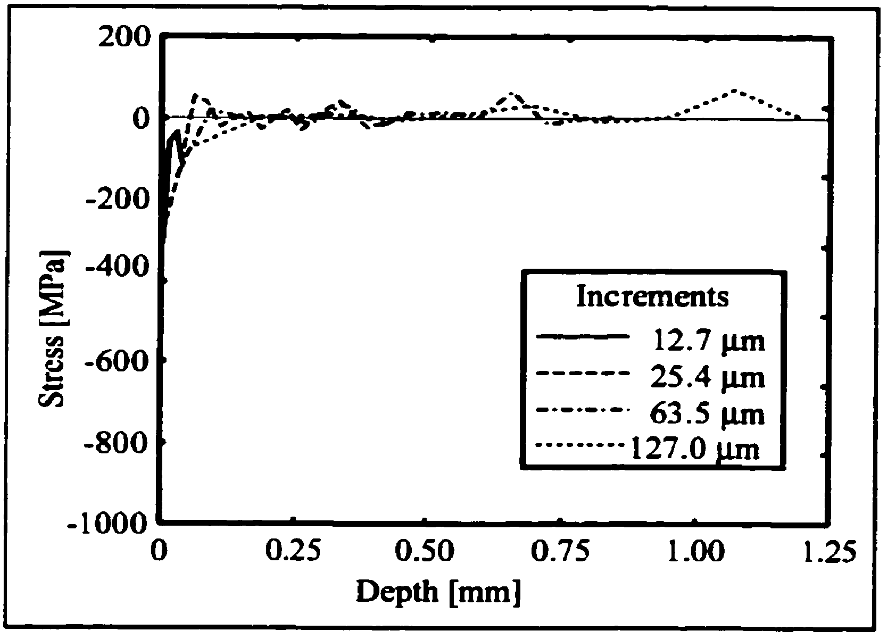

(a)

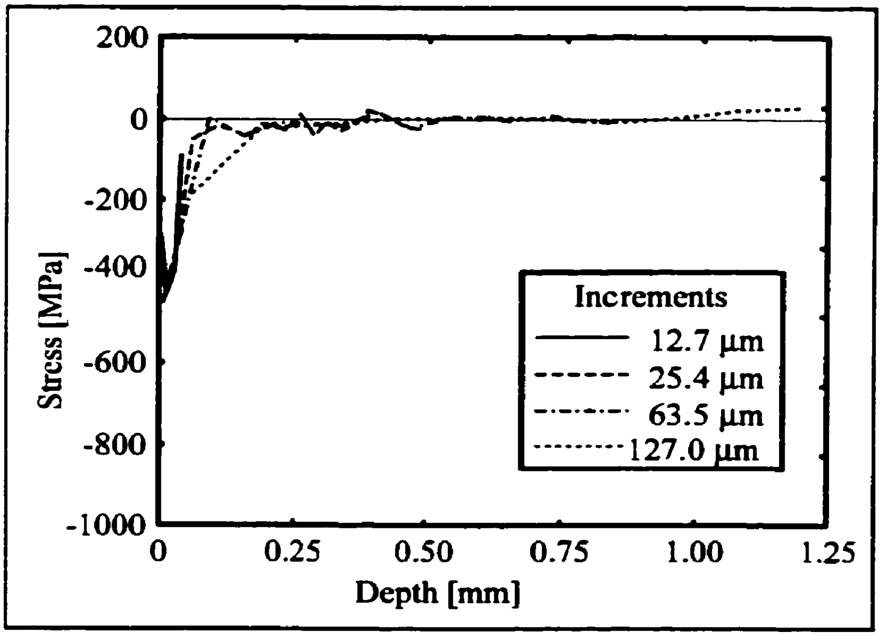

(b)

Fig. 5-37 Residual stress distribution for glass shot peening treatments: (a) 4N and (b) 10N Almen intensity.

The above results were obtained using the calibration coefficients resulting from the linear-elastic finite element analysis described earlier. However, if the magnitude of the residual stress field is close to the yield strength, the stress concentration caused by the presence of the hole may induce plastic strains in the neighborhood of the hole. As a result, considerable errors may result in the stresses calculated using equation (4.4). This problem has been studied both experimentally and analytically by other investigators [92-94]. It was found that the errors were negligible when the residual stress is less than 70% of the yield stress. In the present work, the maximum residual stress measured for all treatments, except for the case where the Almen intensity was 8A, was below this threshold. Therefore the results for the 8A intensity should be viewed with caution.

The attenuation of the strains is clearly visible in Fig. 5-33, where the total relieved strain is shown to be predominantly influenced by the stresses close to the surface. It is shown that beyond a depth of 200 μm, the incremental strain relaxation $\Delta\varepsilon$ decreases with increasing hole depth. As a result, the relative error in the measured strain increases as the hole depth increases. The absolute error present in the measurement affects the accuracy of the stress value. Fig. 5-38 illustrates this effect for the increments investigated. Clearly evident is the trade off required between spatial resolution and accuracy of the estimated stress levels.

A final issue which must be addressed is the sensitivity of the technique to the determination of the initial contact of the milling cutter with the specimen. Fig. 5-39 shows the effect of adjusting the assumed contact height upon the resulting residual stress profile. The figure shows the effect of adjusting the contact height by a total of 6.35 μm (0.25×10^{-3} inch) for the finest inversion increment. This figure clearly shows that a small offset in the initial point of contact has a negligible effect on the measured maximum compressive stress.

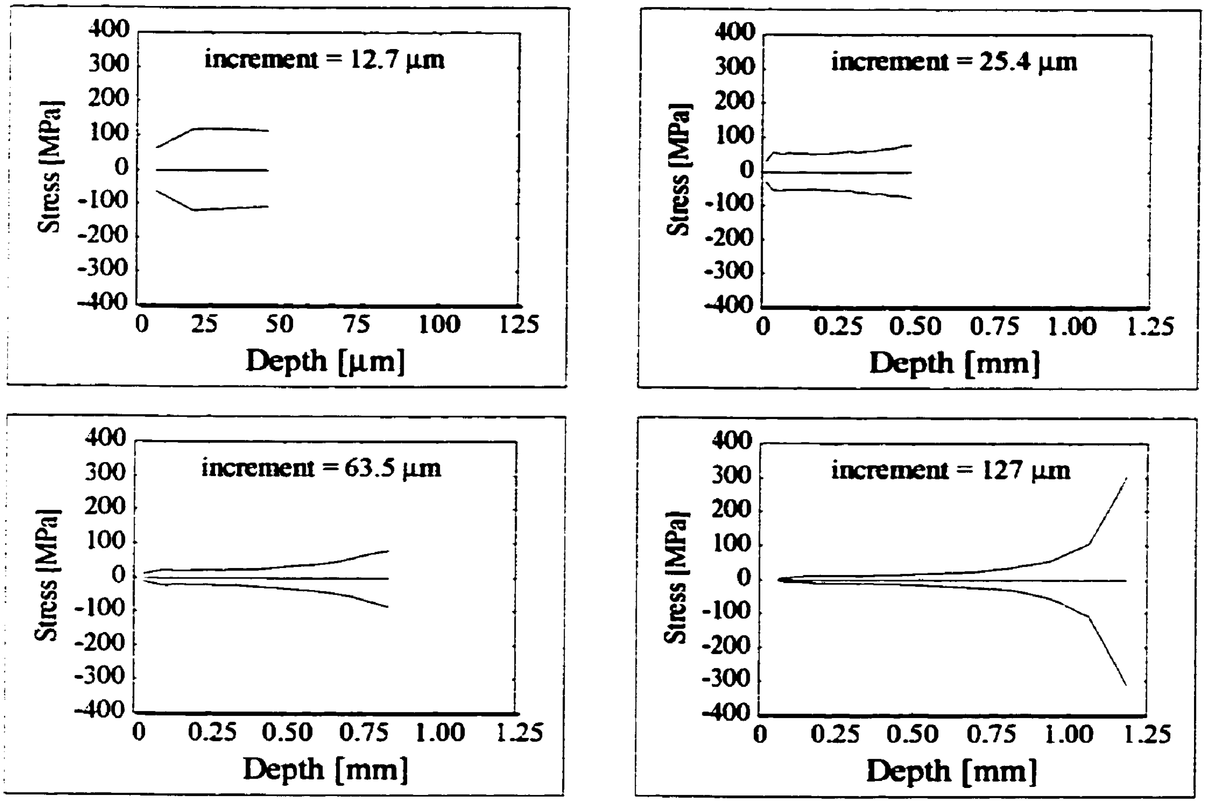

Fig. 5-38 Cumulative error bands for 1 microstrain error.

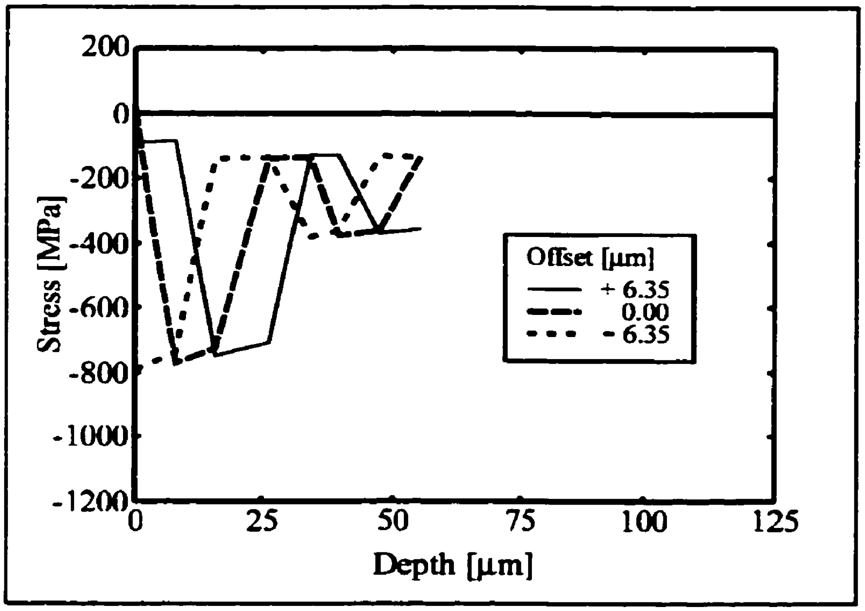

Fig. 5-39 Effect of zero level error on measured residual stress profiles.

Concluding remarks

The peening residual stress profiles are characterised by the following:

(i) the residual stress fields are typical of those encountered in peened components and obtained using different measurement techniques [95],

(ii) the experimental results agree with the predictions from the single shot non-linear dynamic finite element model, and

(iii) the peening intensity gives a reasonable measure of the consistency of the treatment.

Unlike the averaging ASTM E-837 approach, the current modified hole-drilling method is capable of calculating high stress gradients and thus allows the detection of the transition from compression to tension in a peening residual stress field and better estimates of the peak subsurface compressive stress magnitudes.

5.4 Ultrasonic Characterisation of Stress Field

5.4.1 Applied Stress Field

The first step in the application of the LLW technique to the measurement of residual stress was to evaluate the technique's capability to measure the stress state in a body. A uniform aluminium 7075-T651 specimen was incrementally loaded to 50% of its yield strength (σ_0=500 MPa) and the Lamb modes were acquired for incident angles of 16°, 18°, 20° and 22°. The Modal Frequency Spacing (MFS) [73] technique was used to calculate the resulting effective transverse wave velocities for the loaded specimen. Fig. 5-40 shows the effective transverse wave speed as a function of the incident angle. It indicates that the test sample has texture induced anisotropy. The results also illustrate the capability of the technique to measure applied stresses. The overall change in wave speed of approximately 1% at 0.5σ_0 agrees well with values available in the literature for aluminium [86].

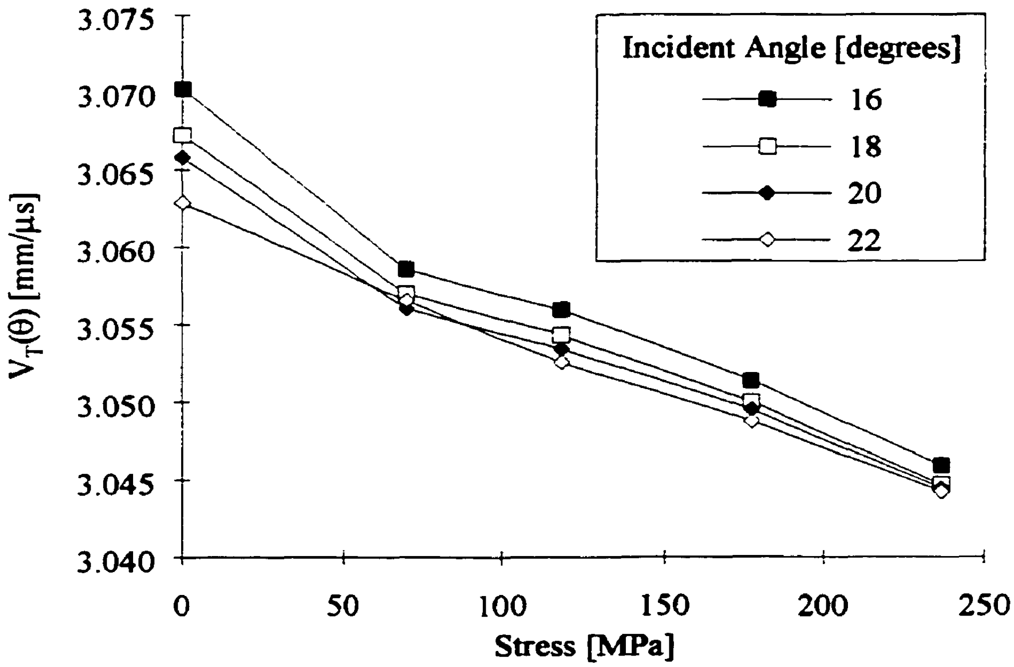

Fig. 5-40 Variation of effective transverse wave velocity with applied stress, as determined by the LLW and MFS techniques.

5.4.2 LLW Analysis of Cold Expanded Holes

As detailed in Chapter 4, the leaky Lamb wave technique was applied to a plate with sequentially expanded fastener holes. There was no observable effect from the resulting residual stress field and/or regions of cold work when scanned perpendicular to the axis of the holes. However, scanning using the leaky Lamb wave with the polarisation direction being parallel to the hole axes resulted in a measurable change in the plate's dispersion curve. Applying the Modal Frequency Spacing (MFS) analysis technique to the data, it was possible to identify regions subjected to the influence of the cold work process (Fig. 5-41). For comparison, the two dimensional finite element results are presented for the σ_{xx} residual stress field (Fig. 5-41(a)). In all cases, the lower hole was expanded first. The results lead to three conclusions. First, the regions showing the large change in the MFS corresponds to the highly stressed region in the FE model. Secondly, the observed change in the MFS is 6%, which is much higher than that observed for the uniform applied elastic field. The acoustoplastic effect must play a significant role to account for this large change in the signal. Thirdly, for the case under study, the 16° incident angle data provided information regarding the residual stress field, which was not evident in the 22° incident angle data. This is attributed to the volume of the material interrogated by the ultrasonic signal. Due to the oblique nature of the ultrasonic beam, the greater the incident angle, the larger the region under test, resulting in greater averaging of the changes, and a reduction in discriminating between those changes in the sample as a result of the treatment.

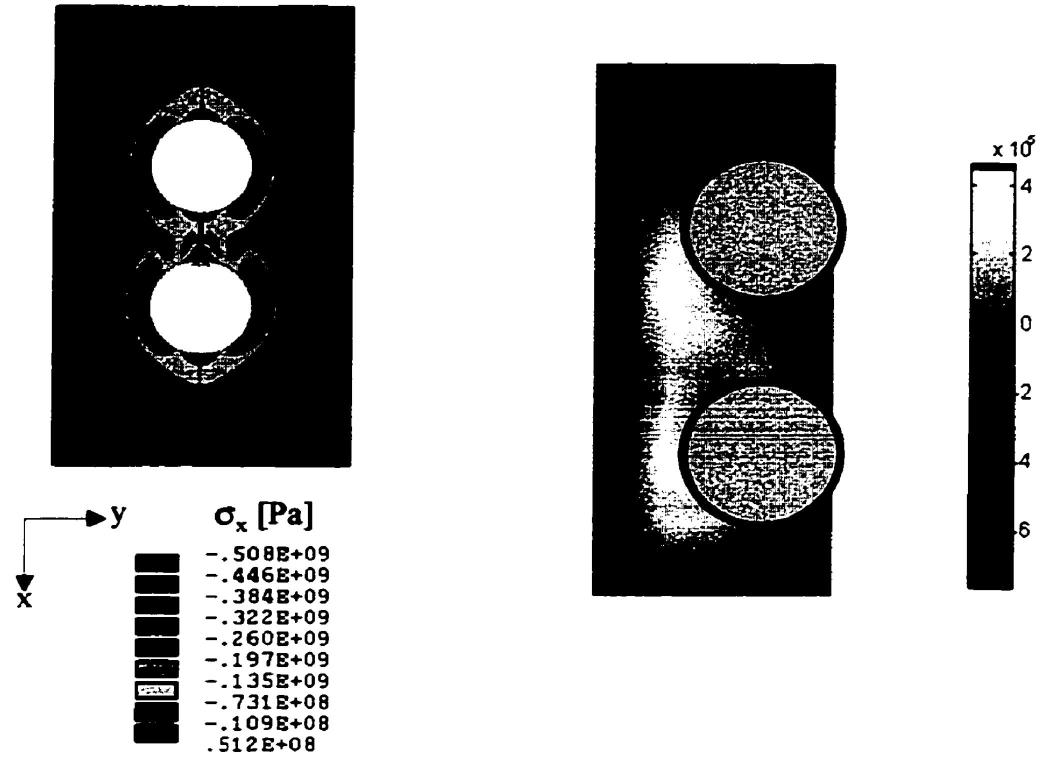

(a) (b)

Fig. 5-41 Change in sequentially cold hole expanded specimen: (a) σ_{xx} from 2D finite element analysis and (b) average LLW MFS at 16° incident angle with measurements taken parallel to axis of holes.

C-Scan Analysis of Cold Expanded Holes

As outlined in section 4.4, the above treated specimen was subjected to ultrasonic C-scan to investigate the area around the holes after the cold expansion treatment. The signals were analysed by examining the change in the time of flight. The average flight time between the first three to four echoes was used. Fig. 5-42 illustrates the averaged time for the two oscilloscopes employed. In these figures, the hole on the right was expanded first. The change in the wave speed shown is on the order of 1%. Contrasting Fig. 5-42(a) and Fig. 5-42(b), the random interleave sampling technique employed by the PM 3380 oscilloscope to obtain higher time resolution is successful. It provides a clearer overall map of the specimen. The entire returned signal from the PM 3380 was also autocorrelated in order to calculate the lag in the signal resulting from all subsequent echoes (Fig. 5-42(c)). The figure shows that autocorrelation can further enhance the interpretation of the data and provide a clear image of the area of interest. However, as expected, the observed changes do not correspond to the predicted residual stress field shown in Fig. 5-41(a). The normal incidence longitudinal wave responds to changes in the stress state in the direction of propagation. The through thickness components of stress, as determined by the three dimensional finite element models, were negligible. Consequently the lack of change in wave speed was expected. However, as shown in Fig. 5-43, the change in the wave speed agrees well with the developed equivalent plastic strain distribution.

Concluding, the traditional C-scan methodology is incapable of measuring the variation of the residual stresses parallel to the accessible surface. The leaky Lamb wave technique, however, shows marked response to the stress and plasticity states. While the current theory cannot invert the data to provide quantitative evaluation of the stress field for this geometry at the present time, the experimental results show that such an effort will succeed.

(a) 3365 Oscilloscope, Direct Time of Flight Data

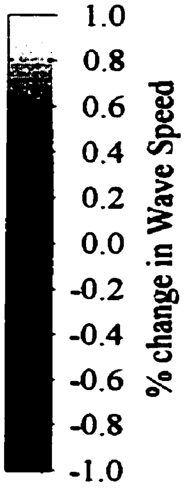

(b) 3380 Oscilloscope, Random Interleaved Time of Flight Data

(c) 3380 Oscilloscope, Autocorrelated Random Interleaved Time of Flight Data

Fig. 5-42 Comparison between (a) direct sampling, (b) random interleave sampling and (c) autocorrelation filtering of C-scan data.

Fig. 5-43 Two dimensional equivalent plastic strain for cold expanded hole.

5.4.3 Shot Peened Specimens

This section addresses the work carried out in modelling and measuring the LLW response to the shot peening induced residual stresses.

Modelling of Leaky Lamb Wave Response

The net stress through the section of all three models detailed in section 3.4.3 was zero, which is indicative of an equilibrated residual stress field. In this case, employing a time of flight approach will not yield a measurable change. On the contrary, the use of the LLW will show a measurable change in the dispersion curve. Fig. 5-44 shows the predicted changes in the dispersion curves with respect to the unstressed plate. Examination of this response shows that the shift is a function of both modal line (or frequency) and incident angle, increasing non-linearly with both. For the given system, each modal line represents approximately 0.32 MHz at 16° incidence, increasing to 0.65 MHz at 26° incidence. The shift represented ranges from 0.3% for a 1.6 MHz mode for an incident angle of 16° through 0.15% for a 15 MHz mode for an incident angle of 26°. This non-linear response enabled the differentiation of the two residual stress profiles examined. The variations ranged from -15 to +10 kHz over the 0-15 MHz frequencies and 16° through 26° incident angles studied. This confirms that the model, which neglected acoustoplastic effects, can be used to discriminate through thickness stress variations.

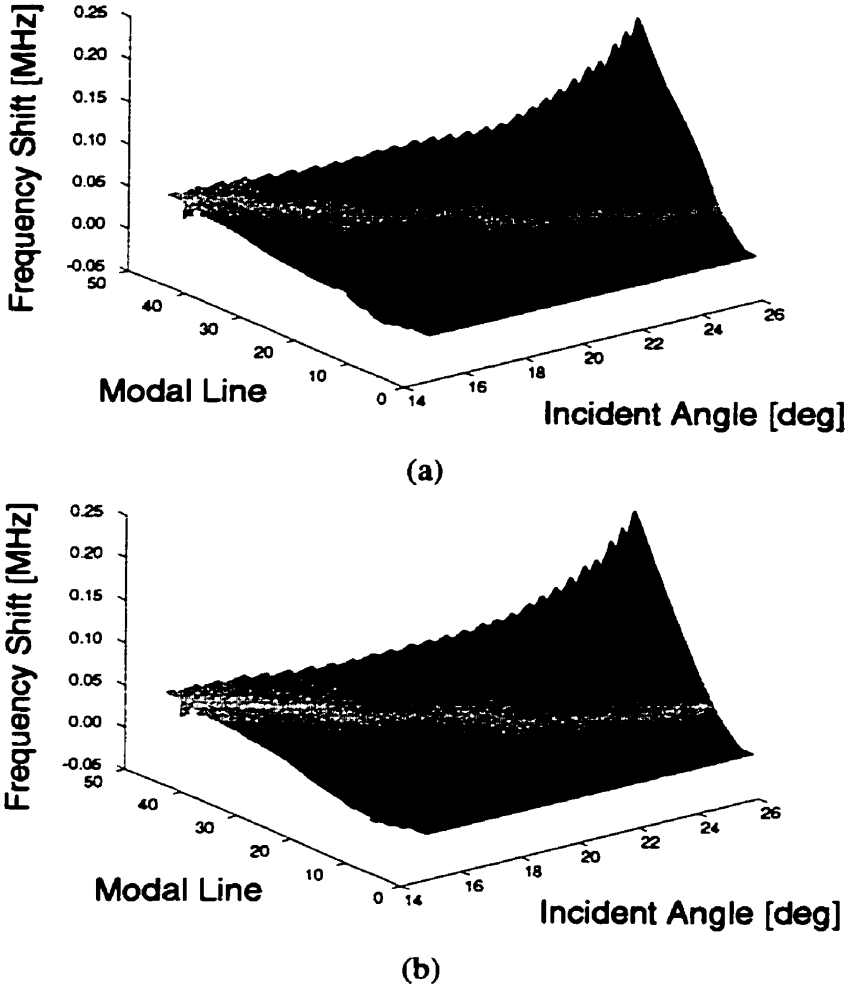

Fig. 5-44 Modelled shift of Lamb modes: (a) single compressive stress layer and (b) three-layered compressive stress.

Measurement of the Leaky Lamb Wave Response

As well as monitoring and correcting for variations in the bath temperature, it was necessary to account for geometrical distortions due to the peening process. With the guiding arc travelling in a fixed plane, the time of flight to receive the echo from the upper surface of the specimen was used to construct the surface profile of the specimen. Fig. 5-45 illustrates the surface profile for a peening intensity of 20A. The profile was then used to calculate the point to point angular variation from the nominal value and a surface was fitted to the data to reduce noise. This angular correction factor was then applied to the measurements at each location. Fig. 5-46 illustrates the data from an aluminium specimen peened to an Almen intensity of 20A before and after correction.

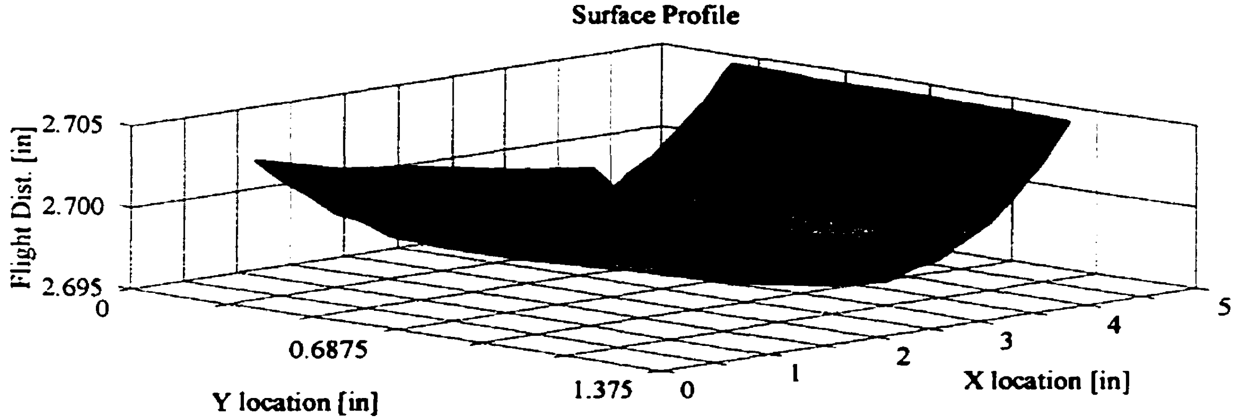

Fig. 5-45 Surface geometry of a shot peened specimen to an Almen intensity of 20A.

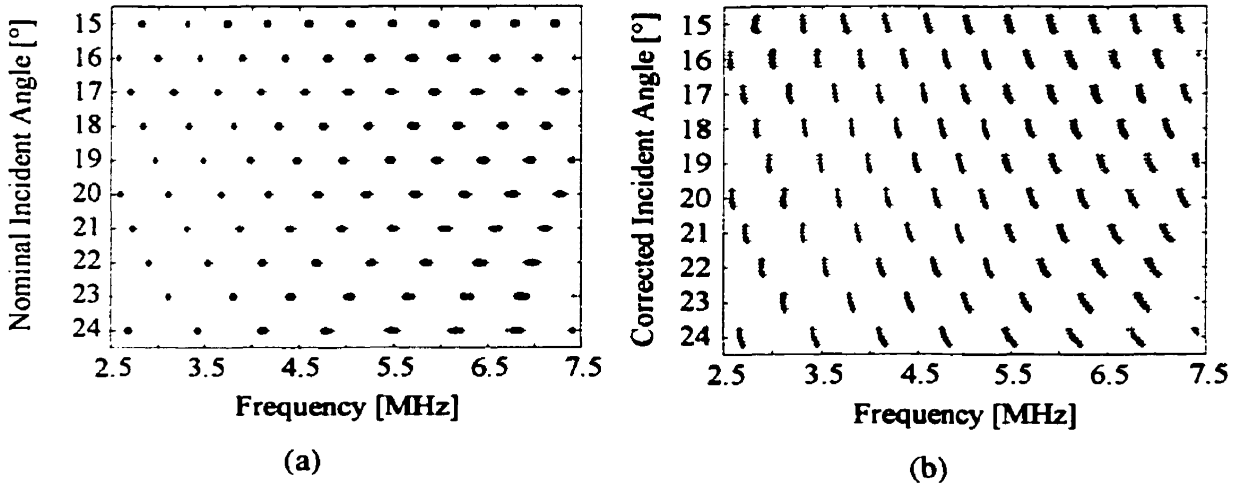

Fig. 5-46 Effect of angular correction on LLW data: (a) original data and (b) corrected data.

The LLW technique is sensitive both to stress state and material variations, as shown in Fig. 5-40. From the LLW modelling results, the response of the LLW signal was expected to be on the order of the variation for the material microstructure. To isolate the signal resulting from the shot peening treatment and to maximize the signal to noise ratio, aggregate measurements were taken over the peened and unpeened portions of the specimens. The modal frequencies obtained at each point and incident angle were corrected as detailed above. These were then combined into two groups, representing the peened and unpeened portions of the plate. The resulting differences at each angle and modal line are shown in Fig. 5-47. Four points should be observed at this point. First, the average Lamb mode decreased in frequency for the peened sections. If the shift were solely due to a reduction in the thickness of the component due to aggressive peening

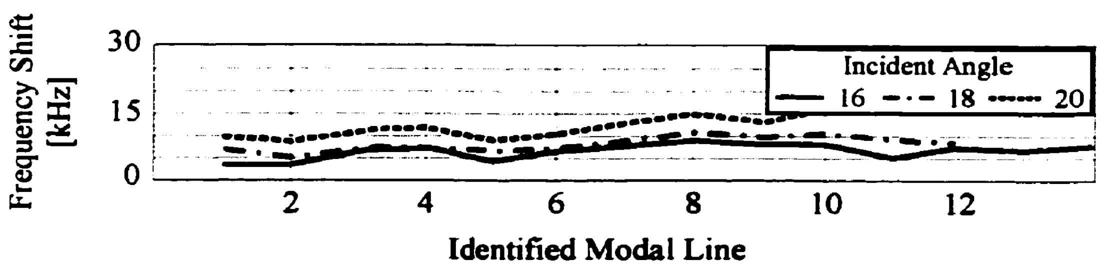

(a) 5A intensity

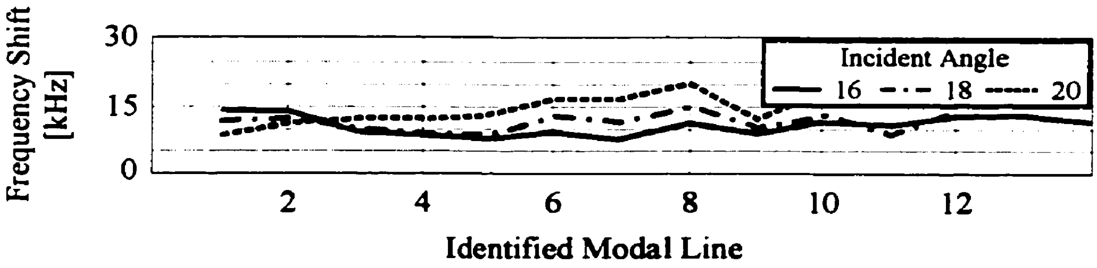

(b) 10 A intensity

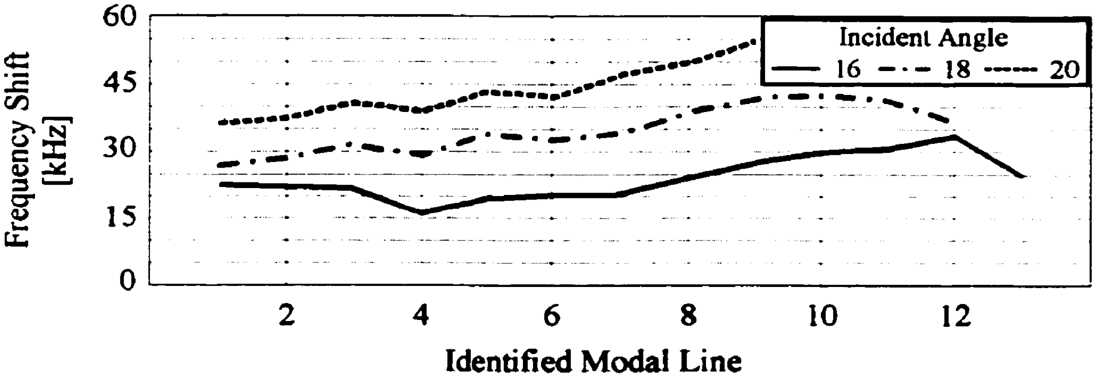

(c) 20 A intensity

Fig. 5-47 LLW modal frequency shift with peening intensity.

treatment, the modal shift would be to the right. Secondly, Fig. 5-47 illustrates that the variation of the Lamb modes is a function of both frequency and angle. This was as predicted in the modelling of the LLW modes for a plate with a shot peened residual stress profile. The shift of a modal line increased with increasing mode number (frequency). The magnitude of the measured shift was greater than that predicted by the model. This was attributed to the simplifications adopted in the model, including not accounting for plasticity and acousto-plastic effects. Third, the sensitivity of the LLW technique increased with increasing angle of incidence. This was a trade off with possible spatial resolution, as the area under examination increases with increasing angle of incidence due to oblique nature of the ultrasonic beam. Fourth, the magnitude of the shift increases with the intensity of the treatment. This agrees with the predictions from the FE modelling of the shot peening process. The increased intensity (velocity) results in a deeper compressed layer and larger plastic zone. This corresponds to a thicker layer of material subjected to decreased wave velocities, and hence larger effects upon the LLW dispersion curve.

While traditional ultrasonic scans could be employed to examine the surface geometry and curvature of the peened plates examined here, they are not capable of characterising the variation of the peening treatment. The leaky Lamb wave technique, with its low capital and operating costs, non destructive nature, deep penetration and capability to resolve in depth variations, offers the most promising avenue for quantitative nondestructive residual stress characterisation.

5.5 Characterisation of Mechanically Induced Residual Stresses

The outcome of the previously discussed simulations (cold hole expansion and shot peening) and experimental programmes can now be used to characterise mechanically induced residual stresses. In order to account for residual stress fields in the design stage of components, and to optimise the components for minimum weight and or maximum fatigue life, the designer needs information regarding five key parameters concerning mechanically induced residual stresses. These parameters are (i) the surface compressive stress, (ii) the maximum subsurface compressive stress and (iii) the depth at which it occurs, (iv) the depth of the compressed layer and (v) the maximum tensile subsurface stress (Fig. 5-48). In all the studies conducted, the magnitude of the residual tensile field was small with respect to the compressive field. The majority of the fatigue fracture behaviour of the component is therefore governed by the surface features and the five parameters outlined.

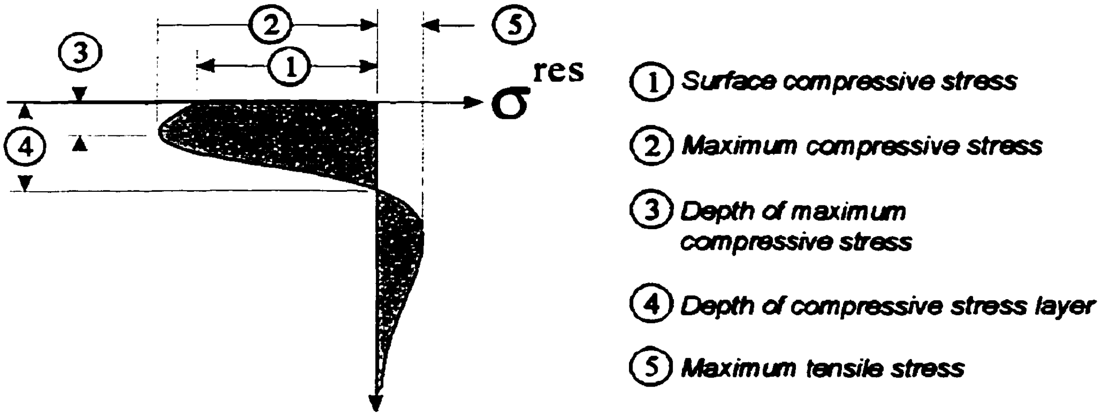

Fig. 5-48 Key parameters of mechanically induced residual stresses.

The three dimensional nature of the stress field resulting from cold hole expansion cannot be ignored. The resulting compressive stress field varies significantly through the depth of the treated component. The commonly adopted two dimensional models significantly over estimate the compressive stresses through the section. This is further exacerbated by the presence of nearby, expanded fastener holes. These findings were non-existent.

The experimental techniques developed to extend the incremental hole drilling technique allowed the improved resolution and measurement of the large residual stress gradients near the surface resulting from shot peening treatments. The leaky Lamb wave technique was shown to have greater sensitivity to stresses varying in the plane of the inspected surface. Furthermore, the technique can be used to characterise the peening treatment, which was not possible with traditional ultrasonic approaches. The LLW modal response was also shown to be sensitive to in depth variations in the residual stress profile. These developments represent a significant contribution to the characterisation of mechanically induced residual stresses where large stress gradients play a significant role in determining the life and integrity of many engineering components.

Chapter 6 Conclusions and Future Work

Summary: In this chapter we state the problem, identify the objectives of the study and outline the contribution of the thesis as well as the conclusions resulting from this work. Furthermore, a brief description of areas that would benefit from additional future work is provided.

6.1 Statement of the Problem

Residual stresses play an important role in determining the fatigue life of most engineering components. For example, many welded structures experience high tensile residual stresses at the heat affected zone as a result of high thermal gradients and possible phase change in the material. These high tensile residual stresses promote fatigue crack initiation and growth and may lead to catastrophic failure. In contrast, compressive residual stresses, such as those introduced by shot peening and cold hole expansion treatments, are highly effective in improving the fatigue strength of the treated components. This is the reason why these cold work treatments are used in the aerospace and automotive industries. A major impediment to the wider use and implementation at an early design stage stems from the inability to characterise the resulting residual stress field which governs the mechanical integrity of the component.

6.2 Objectives

It was therefore the objective of this study to determine the residual stress fields resulting from mechanically induced residual stresses both numerically using the finite element method and experimentally using destructive and nondestructive methods. In particular, it was desired to:

(i) carry out non-linear three dimensional quasi-static finite element analysis,

(ii) conduct dynamic non-linear three dimensional finite element analysis accounting for contact between the mandrel/shot and the target,

(iii) modify the incremental hole drilling technique to obtain the high in-depth stress gradients in the residual stress profile,

(iv) implement a newly developed leaky Lamb wave technique. This entailed the design and commissioning of an automated guided wave facility to acquire the frequency response of multi-layered systems and relating the output to peening treatment.

6.3 Thesis Contribution

6.3.1 Findings Relating to Finite Element Studies

Cold Hole Expansion

Extensive non-linear three dimensional elasto-plastic quasi-static finite element analyses were carried out to evaluate the residual stress fields due to the cold expansion of two adjacent fastener holes. The results of this investigation can be summarised as follows:

(i) the centre distance between the two holes can dramatically influence the residual stress field, leading to high tensile residual stresses,

(ii) sequential expansion of two adjacent holes leads to a much higher tensile residual stress than simultaneous expansion,

(iii) sequential expansion of closely spaced fastener holes may lead to partial relief of the compressive residual stresses on both the adjacent and far sides of the initially expanded hole, and

(iv) the two dimensional model is incapable of accurately predicting the residual stress variation at the entry and exit faces of the workpiece.

Shot Peening

Comprehensive non-linear dynamic finite element analysis was conducted to simulate the shot peening process. The effect of shot velocity, size and shape upon the time histories of the equivalent stress trajectories, equivalent plastic strains and unloading residual stresses of a target exhibiting bilinear material behaviour is examined and discussed. The work was further extended to account for the effect of the hardening rate of the target upon the residual stress field. The results reveal that the depth of the compressed layer, surface and sub-surface residual stresses are significantly influenced by the shot velocity, shot shape and to a much lesser extent, the strain-hardening rate of the target. Furthermore, the work accounts for strain rate effects using Cowper-Symonds visco-plastic model. The results also show the significant influence of the strain rate upon the plastic zone development and compressed layer.

Since the shot peening treatment involves more than a single shot, it was prudent to investigate the effect of multiple impacts on the induced residual stress field and plastic zone development. Two aspects of the work were accordingly examined: the first was concerned with examining the effect of simultaneous twin shot impact upon the outcome of the treatment. The results, which are outlined in Chapter 5, show that interaction effects are significant at the midplane between indentations. Underneath each of the impacting shots, the induced residual stress and plastic zone are predominantly influenced by the impacting shot and interaction effects are insignificant.

The second was motivated by our desire to study the influence of multiple indentations on the outcome of the treatment. To the author's knowledge, this is the first attempt to model the shot peening realistically, accounting for interactions resulting from multiple simultaneous and sequential impacts. The results are significant and should aid the designer to account for mechanically induced residual stresses in sizing components. Details of the findings can be viewed in Chapter 5.

6.3.2 Findings Relating to Experimental Studies

Incremental Hole Drilling Studies

The incremental hole drilling technique was enhanced and improved to the extent that it is now capable of determining large stress gradients near the surface of the specimen using newly developed calibration coefficients. It was also shown that the magnitude of the residual stresses near the surface were insensitive to a zeroing error of up to 12.7 μm.

The developed technique and calibration coefficients were used to obtain residual stress profiles for a variety of light to moderate peening intensities. The results showed good "overall" agreement with finite element predictions.

Ultrasonic Characterisation Studies

A fully automated leaky Lamb wave test facility was designed and constructed to carry out inspection of layered media. This included the design and implementation of controlling hardware as well as software routines implemented within MatLab for the efficient post-processing and analysis of the data. This test facility was then applied to three classes of inspection related to mechanically induced stresses. The first was the ability to distinguish uniaxial applied stress. The observed changes in the Modal Frequency Spacing and extracted transverse wave velocity agreed well with published data. The second application was to examine the spatially varying stress field around cold expanded holes. The sensitivity of the technique was significantly better than traditional ultrasonic C-scans. However, the path over which the LLW technique operates reduces its effective spatial resolution. Thirdly, the LLW technique was successfully applied to distinguish the peening intensity in aluminium specimens subjected to varying levels of peening treatment. The variation was found to be a function of the peening treatment, incident angle and the modal frequency. This was in agreement with the LLW model developed to describe the residual stress field resulting from shot peening in terms of a depth varying transversely isotropic layered media. The magnitude of the predicted changes was on the same order as those observed from the experimental work.

6.4 Future Work

During the course of these studies the following items were considered worthy of future work:

(i) Development of very high strain rate models to account for the rates experienced in the shot peening process. Furthermore, it would be useful to account for the effect of thermal relaxation in these models.

(ii) Correlating the FE results directly to the Almen intensity measurements currently adopted by the industry.

(iii) Optimising the mechanically induced residual stress field resulting from the treatment to maximise the fatigue life of a component made from a specific material.

(iv) Development of a modified leaky Lamb wave probe which incorporates independent angular adjustment and surface tracking to scan components with complex geometries.

(v) Development of a transversely isotropic Lamb wave model of a shot peened component incorporating acousto-plastic effects.

(vi) Investigate the effect of re-peening upon the mechanically induced residual stresses.

References

[1] Hammond, D.W., and Meguid, S.A., "Crack Propagation in the Presence of Shot-Peening Residual Stresses", Engineering Fracture Mechanics, **37**(2), pp. 373-387, 1990.

[2] Hammond, D.W., and Meguid, S.A., "Fatigue Fracture and Residual Stress Relaxation in Shot-Peened Components", Surface Engineering, S.A. Meguid, ed., Elsevier Applied Science, New York, pp.386-392, 1990.

[3] James, M.R., "The Relaxation of Residual Stresses During Fatigue", Residual Stress and Stress Relaxation, E. Kula and V. Weiss, eds., Plenum Publishing Corporation, New York, pp. 297-314, 1982.

[4] Quist, W.E., Narayanan, G.H. and Wingert, A.L. "Aluminum-Lithium for aircraft structures". In Proc. Second Conference on Aluminum-Lithium alloys, pp. 313-334, 1983.

[5] Sakata, I.F., "Systems study of transport aircraft incorporating advance Aluminum-Lithium". NASA Report, CR-165820, 1982.

[6] Kirsch, G., "Die Theorie der Elastizitat und die Bedurfnisse der Festigkeitslehre", Verlag des Vereins Deutscher Ingenieure, **42**, pp. 797-807, 1898.

[7] Jeffery, G.B., "Plane Stress and Plane Strain in Bipolar Co-ordinates", Philosophical Transactions of the Royal Society of London, **A221**, pp. 265-293, 1920.

[8] Mindlin, R.D., "Stress Distribution Around a Tunnel", Transactions of the American Society of Civil Engineers, **105**, pp. 1117-1153, 1940.

[9] Mindlin, R.D., "Stress Distribution Around a Hole Near the Edge of a Plate Under Tension", Proceedings of Society of Experimental Stress Analysis, **5**, pp. 56-68, 1948.

[10] Yu, I.W. and Sendeckyj, G.P., "Multiple Circular Inclusion Problems in Plane Elastostatics", ASME Journal of Applied Mechanics, **41**, pp. 215-221, 1974.

[11] Horii, H. and Nemat-Nasser, S., "Elastic Fields of Interacting Inhomogeneities", International Journal of Solids and Structures, **21**(7), pp. 731-745, 1985.

[12] Meguid, S.A. and Shen, C.L., "On the Elastic Fields of Interacting Defense and Main Hole Systems", International Journal of Mechanical Sciences, **34**(1), pp. 17-29, 1992.

[13] Hu, K.X., Chandra, A. and Huang, Y., "Multiple Void-Crack Interaction", International Journal of Solids and Structures, **30**(11), pp. 1473-1489, 1993.

[14] Dundurs, J. and Hetenyi, M., "The Elastic Plane With a Circular Insert, Loaded by a Radial Force", ASME Jounal of Applied Mechanics, **28**, pp. 103-111, 1961.

[15] Hetenyi, M. and Dundurs, J., "The Elastic Plane With a Circular Insert, Loaded by a Tangentially Directed Force", ASME Jounal of Applied Mechanics, **29**, pp. 62-368, 1962.

[16] Kienzler, R. and Zhuping, D., "On the Distribution of Hoop Stresses Around Circular Holes in Elastic Sheets", ASME Journal of Applied Mechanics, **54**, pp. 110-114, 1987.

[17] Greenwood, J.A. "Exact Formulae for Stresses Around Circular Holes and Inclusions", International Journal of Mechanical Sciences, **31**(3), pp. 219-227, 1989.

[18] Erickson, P.E. and Riley, W.F., "Minimizing Stress Concentrations Around Circular Holes in Uniaxially Loaded Plates", Experimental Mechanics, **18**, pp. 97-100, 1978.

[19] Heywood, R.B., Designing by Photoelasticity, Chapman & Hall, Ltd., London, 1952.

[20] Jindal, U.C., "Reduction of Stress Concentration Around a Hole in a Uniaxially Loaded Plate", Journal of Strain Analysis, **18**(2), pp. 135-141, 1983.

[21] Meguid, S.A., "Finite Element Analysis of Defense Hole Systems for the Reduction of Stress Concentration in a Uniaxially-loaded Plate with Two Coaxial Holes", Engineering Fracture Mechanics, **25**(4), pp. 403-413, 1986.

[22] Meguid, S.A. and Gong, S.X., "Stress Concentration Around Interacting Circular Holes: A Comparison Between Theory and Experiments", Engineering Fracture Mechanics, **44**(2), pp. 247-256, 1993.

[23] Champoux, R.L., "Overview of Hole Cold Expansion Methods", Proceedings of the International Conrefence on Fatigue Prevention and Design, pp. 35-61, Amsterdam, The Netherlands, 1986.

[24] Bernard, M., Bui-Quoc, T., Julien, D. and Forgues, S., "Feasibility Study of Cold Expansion Processes Modelling", Report 063SS.W8477-1-AC89, Department of National Defence, 1993.

[25] Nadai, A., Theory of Flow and Fracture of Solids, McGraw-Hill, New York, 1950.

[26] Hsu, Y.C. and Forman, R.G., "Elastic-plastic Analysis of an Infinite Sheet Having a Circular Hole Under Pressure", Journal of Applied Mechanics, **42**, pp. 347-352, 1975.

[27] Rich, D.L. and Impellizzeri, L.F., "Fatigue Analysis of Coldworked and Interference Fit Fasteners Holes", ASTM STP 637, pp. 153-175, 1977.

[28] Jongebreur, A.A. and de Koning, A.U., "Results of a Study of Residual Stresses and Fatigue Crack Growth in Lugs with Expanded Holes", National Research Laboratories, NRL, Amsterdam, The Netherlands, Report No. NRL-MP-83024-U, 1983.

[29] Wanlin, G., "Elastic-plastic Analysis of a Finite Sheet with a Cold-worked Hole", Engineering Fracture Mechanics, **45**, pp. 857-864, 1993.

[30] Link, R.E. and Sanford, R.J., "Residual Strains Surrounding Split-Sleeve Cold Expanded Holes in 7075-T651 Aluminum", Journal of Aircraft, **27**, pp. 599-604, 1990.

[31] Cook, R. and Holdway, P., "Residual Stress Induced by Hole Cold Expansion", In Computer Methods and Experimental Measurements for Surface Treatment Effects, pp. 91-100, Computational Mechanics Publications, Southampton, U.K., 1993.

[32] Poussard, C., Pavier, M.J. and Smith, D.J., "Analytical and Finite Element Predictions of Residual Stresses in Cold Worked Fastener Holes", Journal of Strain Analysis, **30**, pp. 291-304, 1995.

[33] Forgues, S.A., Bernard, M. and Bui-Quoc, T., "3-D Axisymmetric Numerical Analysis and Experimental Study of the Fastener Hole Coldworking Process", In Computer Methods and Experimental Measurements for Surface Treatment Effects, pp. 61-70, Computational Mechanics Publications, Southampton, U.K., 1993.

[34] Bernard, M., Bui-Quoc, T. and Burlat, M., "Effect of Re-coldworking on Fatigue Life Enhancement of a Fastener Hole", Engineering Fracture Mechanics, **18**, pp. 765-775, 1995.

[35] Chandawanich, N. and Sharpe, W.N., "An Experimental Study of Fatigue Crack Initiation and Growth from Coldworked Holes", Engineering Fracture Mechanics, **11**, pp. 609-620, 1979.

[36] Papanikos, P., Mechanics of Mixed Mode Fatigue Behaviour of Cold Worked Adjacent Holes, A Thesis for the Degree of Doctor of Philosophy, University of Toronto, 1997.

[37] Fuchs, H.O., "Shot-peening effects and specifications". ASTM STP-196, 1962.

[38] Fuchs, H.O., ed. "Second International Conference on Shot-peening". U.S.A., 1984.

[39] Kirk, D., ed. "Fifth International Conference on Shot-peening". U.K., 1993.

[40] Meguid, S.A., ed. "Impact surface treatment". Elsevier Applied Science Publishers, 1986.

[41] Meguid, S.A., ed. "Surface engineering". Elsevier Applied Science Publishers, 1990.

[42] Metal Improvement Company "Shot-peening applications". MIC Technical Note, Seventh Edition, 1989.

[43] Niku-Lari, A. ed. "First International Conference on Shot-peening". France, 1981.

[44] Wohlfahrt, H., ed. "Third International Conference on Shot-peening". Germany, 1987.

[45] Military specifications "Shot-peening of metal parts". MIL-S-13165C, 1989.

[46] Meguid, S.A. "Effect of partial-coverage upon the fatigue fracture behavior of peened components". Fatigue and Fracture of Engineering Materials and Structures, **14**, pp. 515-530, 1991.

[47] Meguid, S.A., Shagal, G., Stranart, J.C., and Daly, J., "Three Dimensional Dynamic Finite Element Analysis of Shot-Peening Induced Residual Stresses", Finite Elements in Analysis and Design, 31, pp. 179-191, 1999.

[48] Meguid, S.A., Shagal, G., and Stranart, J.C., "Finite Element Modelling of Shot-Peening Residual Stresses", Journal of Material Processing Technology, 92-93, pp. 401-404, 1999.

[49] Rund, C.O. "A review of selected non-destructive methods for residual stress technology". NDT International, pp. 15-23, 1982.

[50] Shackelford, J.F. and Brown, B. "A critical review of residual stress technology". In international Advances in Nondestructive testing, **15**, pp. 195-215, 1990.

[51] Meguid, S.A. "Feasibility of shot-peening modeling". DND Report, DND No. 321419090, 1992.

[52] ASTM Standards "Standard test method for determining residual stresses by the hole drilling strain gage method". ASTM-E 837, 1985.

[53] Measurement Group "Measurement of residual stresses by the hole-drilling strain gage method". Technical Note, TN-503-3, 1989.

[54] Rendler, N.J. and Vigness, I. "Hole-drilling strain gage method of measuring residual stresses". Experimental Mechanics, **6**, pp. 577-586, 1966.

[55] Schajer, G.S. "Application of finite element calculations to residual stress measurement". Journal Engineering Materials and Technology, **103**, pp. 157-163, 1981.

[56] Kelsey, R.A. "Measuring nonuniform residual stresses by the hole-drilling method". In Proc. of SESA, **14**, pp. 181-184, 1954.

[57] Soete, W. and Vancrombrugge, R. "An industrial method for the determination of residual stresses". In Proc. of SESA, **8**, pp. 17-28, 1950.

[58] Nickola, W.E. "Practical subsurface residual stress evaluation by the hole-drilling method". In Proc. Conference on Experimental Mechanics 86. pp. 126-136, 1986.

[59] Bijak-Zochowski, M. "A semidestructive method for measuring residual stresses". VDI-Berichte, **313**, 469-476, 1978.

[60] Flaman, M.T. and Manning, B.H. "Determination of residual stress variation with depth by the hole-drilling method". Experimental Mechanics, **25**, pp. 205-207, 1985.

[61] Schajer, G.S. "Measurement of non-uniform residual stresses using the hole drilling method: Part II. Practical application of the integral method". Journal Engineering Materials and Technology, **1**, pp. 343-349, 1988.

[62] Schajer, G.S. "Measurement of non-uniform residual stresses using the hole drilling method: Part I. Stress calculation procedures". Journal Engineering Materials and Technology, **1**, pp. 338-343, 1988.

[63] Burkhardt, G.L., Kwun, H., and Crouch, A.E., "Review of Stress Measurement Techniques in Pipelines", Proc. ASME Pressure Vessel and Piping Conference, pp. 95-103, 1990.

[64] Sundstrom, O., and Torronen, K., "The Use of Barkhausen Noise Analysis in Non-destructive Testing", Materials Evaluation, **37**, No. 3, pp. 51-56, 1979.

[65] Dike, J.J., and Johnson, G.C., "Residual Stress Determination Using Acoustoelasticity", J. Appl. Mech., **57**, pp. 12-17, March 1990.

[66] Kino, G.S., Hunter, J.B., Johnson, G.C., Selfridge, A.R., Barnett, D.M., Herman, G., and Steele, C.R., "Acoustoelastic Imaging of Stress Fields", J. Appl. Phys., **50**(4), pp. 2607-2613, 1979.

[67] Koshti, A.M., and Egle, D.M., "Stress Measurement via the Acoustoelastic Effect and Water-Coupled Ultrasonic Waves", Nondestructive Testing and Evaluation for Manufacturing and Construction, H.L.M. dos Reis, ed., Hemisphere Publishing Co., pp. 393-405, 1990.

[68] Hsu, N.N., "Acoustical Birefringence and the Use of Ultrasonic Waves for Experimental Stress Analysis", Experimental Mechanics, **14**, pp. 169-176, 1974.

[69] Hirao, M., Ultrasonic Surface Waves Related to Quantitative Nondestructive Evaluation, A Thesis for the Degree of Doctor of Engineering, Osaka University, 1982.

[70] Bray, D.E., Leon-Salamanca, T., and Janghans, P., "Application of Lcr Ultrasonic Technique for Evaluation of Post-Weld Heat Treatment in Steel Plates", Nondestructive Evaluation NDE Planning and Application, Proceedings 1989, ASME Pressure Vessles and Piping Conference, R.D. Streit, ed., pp. 191-197, 1989.

[71] Hirao, M., Tomizawa, A., and Fukuoka, H., "Nonlinear resonance interaction of ultrasonic waves under applied stress", J. Appl. Phys., **56**, pp. 235-7, July 1984.

[72] Mal, A.K., Xu, P.-C., and Bar-Cohen, Y., "Leaky Lamb Waves for the Ultrasonic Nondestructive Evaluation of Adhesive Bonds", J. Eng. Mat. Techn., **112**, pp. 255-259, 1990.

[73] Xu, P.-C., Lindenschmidt, K.-E., and Meguid, S.A., "A new high-frequency analysis of coatings using leaky Lamb waves", J. Acoust. Soc. Am., **94**(4), pp. 2954-2962, 1993.

[74] Xu, P.-C., Stranart, J.C. and Meguid, S.A., "Nondestructive Characterization of a Layered Medium using Novel Modal Analysis", Applied Mechanics and Materials Division Summer Meeting of the American Society of Mechanical Engineers, Los Angeles, California, June 28-30, pp. 101-112, 1995.

[75] Stranart, J.C. and Meguid, S.A., "Non-destructive Evaluation of Coating Properties Using Guided Waves", Mechanics in Design, Toronto, Ontario, May 6-9, 1996.

[76] Machinery's Handbook, (edited by R.E. Green), 24th edition, Industrial Press Inc., New York, 1992.

[77] Zhong, Z.H., "Finite Element Procedures for Contact-Impact Problems", Oxford University Press, 1993.

[78] Taylor, G., " The Use of Flat-Ended Projectiles for Determining Dynamic Yield Stress", Proceedings of Royal Society of London, **A194**, pp. 289-299, 1948.

[79] Parkes, E.W., "The Permanent Deformation of a Cantilever Struck Transversely at its Tip", Proceedings of the Royal Society of London, **A228**, pp. 462-472, 1955.

[80] Wilkins, M.L. and Guinan, M.W., "Impact of Cylinders on a Rigid Boundary", Journal of Applied Physics, **44**, pp.1200-1206, 1973.

[81] Davies, R.G., "The Effect of Strain-Rate Upon the Tensile Deformation of Materials", Journal of Engineering Materials and Technology, **97**, pp. 151-155, 1975.

[82] Symonds, P.S., "Viscoplastic Behaviour in Response of Structures to Dynamic Loading" In Behaviour of Materials Under Dynamic Loading, pp. 106, ASME, 1965.

[83] Symonds, P.S., "Survey of Methods of Analysis for Plastic Deformation of Structures Under Dynamic Loadings", Report BU/NSRDC/1-67, Brown University, 1967

[84] Jones, N. "Structural aspect of ship collisions", in Structural Crashworthiness, Chapter 11, (edited by N. Jones and T. Wierzbicki), Butterworth, London, pp. 308-337, 1983.

[85] Ewing, W.M., Jardetsky, W.S., and Press, F., "Elastic Waves in Layered Media", McGraw-Hill, New York, pp. 281-288, 1957.

[86] Krautkrämer, J. and Krautkrämer, H., Ultrasonic Testing of Materials, 4th Edition, Springer-Verlag, New York, pp. 533-539, 1990.

[87] Sachs, G., "Der nachweis immerer spannungen in stangen und rohren", Zeits. Metall., **19**, pp. 352-357, 1927.

[88] ANSYS (1998). "Engineering Analysis Systems". Swanson Analysis Systems Inc., Revision 5.4.

[89] ASTM Standards "Standard Test Methods for Tension Testing of Metallic Materials". ASTM E8 6.3, 1985.

[90] Papanikos, P. and Meguid, S.A., "Elasto-plastic finite element analysis of cold expansion of adjacent fastener holes", in Proc. of Advances in Materials and Processing Technologies (AMPT '97), M. Andritschky ed., pp. 799-804, 1997.

[91] Edberg, J., Lindgren, L. and Mori, K., "Shot peening simulated by two different finite element formulations", in: Shen & Dawson (editors), Simulation of Materials Processing: Theory, Methods and Applications, Balkema, Rotterdam, pp. 425-430, 1995.

[92] Nickola, W.E. "Post yield effects on center hole residual stress measurement." In Proc. Fifth International Congress on Experimental Mechanics, 126-136, 1984.

[93] Beaney, E.M. "Accurate measurement of residual stress on any steel using the center hole method". Strain, **12**, 99-106, 1976.

[94] Procter, E. and Beaney, E.M. "Recent developments in center hole technique for residual stress measurement". Experimental Mechanics, **6**, 10-15, 1982.

[95] Fuchs, H.O. "Shot-peening". In Mechanical Engineer's Handbook, 941-951. John Wiley & Sons. Cincinnati, OH. 1986.

[96] Mal, A.K., Xu, P.-C., and Bar-Cohen, Y., "Analysis of leaky Lamb waves in bonded plates", Int. J. Eng. Sci., Vol. 27, pp. 779-791, 1989.

[97] Refaat, M.H. and Meguid, S.A., "A novel finite element approach to frictional contact problems", Int. J. for Numerical Methods in Eng., **39**, pp. 3889-3992, 1996.

Appendix A: Hole Drilling Calibration Coefficients

Coefficients for A in $A\bar{\sigma} = \frac{E}{1+\nu}\bar{\varepsilon}$, where $\bar{\varepsilon}$ are the relaxed strains recorded for each increment and $\bar{\sigma}$ are the biaxial depth varying stresses.

127 µm (0.0050") Increments

A= 10^{-4} *

-187.96	0	0	0	0	0	0	0	0	0
-247.92	-192.94	0	0	0	0	0	0	0	0
-288.62	-242.95	-174.56	0	0	0	0	0	0	0
-316.85	-272.53	-216.92	-145.24	0	0	0	0	0	0
-336.23	-292.15	-239.45	-180.56	-113.22	0	0	0	0	0
-349.37	-305.25	-253.53	-197.77	-141.92	-83.23	0	0	0	0
-358.25	-313.99	-262.61	-208.04	-155.08	-106.06	-57.468	0	0	0
-364.26	-319.86	-268.56	-214.47	-162.64	-116.04	-75.252	-36.508	0	0
-368.37	-323.81	-272.49	-218.58	-167.22	-121.57	-82.696	-50.056	-20.046	0
-371.18	-326.50	-275.11	-221.24	-170.08	-124.83	-86.695	-55.513	-30.171	-7.6092

63.5 µm (0.0025") Increments

$A = 10^{-5}$ *

-816.95	0	0	0	0	0	0	0	0	0	0	0	0	0
-1007.60	-877.46	0	0	0	0	0	0	0	0	0	0	0	0
-1160.50	-1055.80	-890.24	0	0	0	0	0	0	0	0	0	0	0
-1289.50	-1189.00	-1062.40	-870.43	0	0	0	0	0	0	0	0	0	0
-1398.40	-1298.80	-1182.50	-1036.70	-827.57	0	0	0	0	0	0	0	0	0
-1489.90	-1390.30	-1278.20	-1146.10	-986.62	-768.77	0	0	0	0	0	0	0	0
-1566.30	-1466.50	-1356.40	-1230.70	-1086.50	-919.31	-700.06	0	0	0	0	0	0	0
-1629.90	-1529.70	-1420.50	-1298.20	-1161.60	-1010.40	-841.14	-626.39	0	0	0	0	0	0
-1682.60	-1582.10	-1473.30	-1352.90	-1220.50	-1077.30	-923.87	-757.20	-551.24	0	0	0	0	0
-1726.20	-1625.30	-1516.70	-1397.30	-1267.40	-1128.70	-983.27	-831.82	-671.36	-477.41	0	0	0	0
-1762.10	-1660.80	-1552.20	-1433.40	-1305.00	-1169.10	-1028.20	-884.45	-738.33	-586.84	-407.03	0	0	0
-1791.60	-1690.10	-1581.30	-1462.90	-1335.40	-1201.10	-1063.10	-923.72	-784.87	-646.66	-505.98	-341.36	0	0
-1816.00	-1714.10	-1605.20	-1486.90	-1359.90	-1226.70	-1090.40	-953.82	-819.17	-687.69	-559.14	-430.22	-281.07	0
-1836.00	-1733.80	-1624.80	-1506.50	-1379.80	-1247.30	-1112.10	-977.23	-845.17	-717.57	-595.13	-477.17	-360.36	-226.52

25.4 µm (0.0010") Increments

A= 10^{-5} *

-289.09	0	0	0	0	0	0	0	0	0	0	0	0	0
-326.54	-306.66	0	0	0	0	0	0	0	0	0	0	0	0
-358.89	-343.10	-318.12	0	0	0	0	0	0	0	0	0	0	0
-388.53	-373.46	-354.86	-325.50	0	0	0	0	0	0	0	0	0	0
-416.00	-401.11	-384.24	-362.79	-329.72	0	0	0	0	0	0	0	0	0
-441.59	-426.70	-410.58	-391.59	-367.57	-331.38	0	0	0	0	0	0	0	0
-465.48	-450.54	-434.77	-417.01	-395.99	-369.70	-330.83	0	0	0	0	0	0	0
-487.81	-472.80	-457.21	-440.13	-420.67	-397.78	-369.52	-328.40	0	0	0	0	0	0
-508.68	-493.59	-478.08	-461.41	-442.90	-421.84	-397.28	-367.32	-324.32	0	0	0	0	0
-528.19	-513.02	-497.54	-481.12	-463.21	-443.30	-420.77	-394.75	-363.35	-318.83	0	0	0	0
-546.41	-531.18	-515.69	-499.43	-481.92	-462.77	-441.53	-417.71	-390.42	-357.85	-312.11	0	0	0
-563.42	-548.12	-532.63	-516.46	-499.23	-480.59	-460.24	-437.82	-412.86	-384.52	-350.99	-304.33	0	0
-579.29	-563.94	-548.41	-532.30	-515.27	-497.01	-477.27	-455.82	-432.35	-406.41	-377.22	-342.95	-295.64	0
-594.08	-578.67	-563.12	-547.05	-530.14	-512.15	-492.87	-472.11	-449.68	-425.30	-398.56	-368.69	-333.89	-286.19
-607.86	-592.40	-576.81	-560.76	-543.94	-526.15	-507.21	-486.97	-465.28	-441.99	-416.85	-389.48	-359.10	-323.96
-620.68	-605.17	-589.55	-573.50	-556.75	-539.11	-520.42	-500.56	-479.43	-456.93	-432.91	-407.17	-379.31	-348.60
-632.59	-617.04	-601.38	-585.33	-568.62	-551.08	-532.59	-513.02	-492.32	-470.42	-447.22	-422.61	-396.39	-368.20
-643.63	-628.04	-612.35	-596.29	-579.61	-562.16	-543.80	-524.47	-504.10	-482.64	-460.06	-436.29	-411.22	-384.67
-653.85	-638.23	-622.51	-606.42	-589.76	-572.37	-554.13	-534.97	-514.86	-493.76	-471.65	-448.50	-424.28	-398.87
-663.28	-647.61	-631.86	-615.76	-599.11	-581.76	-563.60	-544.59	-524.67	-503.85	-482.11	-459.45	-435.85	-411.29

25.4 μm (0.0010") Increments (continued)

A= 10^{-5} *

0	0	0	0	0	0
0	0	0	0	0	0
0	0	0	0	0	0
0	0	0	0	0	0
0	0	0	0	0	0
0	0	0	0	0	0
0	0	0	0	0	0
0	0	0	0	0	0
0	0	0	0	0	0
0	0	0	0	0	0
0	0	0	0	0	0
0	0	0	0	0	0
0	0	0	0	0	0
0	0	0	0	0	0
-276.09	0	0	0	0	0
-313.29	-265.47	0	0	0	0
-337.31	-302.00	-254.43	0	0	0
-356.28	-325.36	-290.19	-243.07	0	0
-372.12	-343.67	-312.83	-277.96	-231.47	0
-385.66	-358.81	-330.40	-299.78	-265.33	-219.73

12.7 μm (0.0005") Increments

A= 10^{-4} *

-13.89	0	0	0
-14.94	-14.44	0	0
-15.83	15.45	-14.83	0
-16.64	-16.28	-15.83	-15.11